Mixing Effect of Transition Metals, Aliovalent Dopants and Component Elements on Proton-Conducting Properties of Perovskite-type Oxides

李, 榮晟

https://doi.org/10.15017/1866377

出版情報：Kyushu University, 2017, 博士（工学）, 課程博士
バージョン：
権利関係：

Mixing Effect of Transition Metals, Aliovalent Dopants and Component Elements on Proton-Conducting Properties of Perovskite-type Oxides

Young-Sung Lee

Department of Molecular and Material Science

Interdisciplinary Graduate school of Engineering Sciences

Kyushu University

A thesis submitted to the Interdisciplinary Graduate School of Engineering Sciences of Kyushu University in partial fulfillment of the requirements for the degree of Doctor of Philosophy.

Approved by:

Prof. Hisahiro Einaga

Prof. Hiroshige Matsumoto

Prof. Fujio Tsumori

Prof. Miki Inada

By

Young-Sung Lee

2017

Abstract

Among candidate proton conducting materials for solid fuel cell and solid oxide electrolysis cell, perovskite type electrolytes have garnered significant attention as the alternative materials. The proton conducting materials offers high electrical conductivity in intermediate temperature region targeted for effective operation of solid oxide fuel cell and solid oxide electrolysis cell. However, fundamental unsolved problems surrounding these proton conducting materials still remain. The effect of dopant species, transition metal diffusion, electrode compatibility and the description of proton conductivity are still not clearly to understand. For those reason, this study aimed to further understanding of the electrical properties of electrolytes base on the proton conducting materials in the most promising perovskite type proton conducting materials. This thesis mainly consists of six parts. The overviews of the proton conducting materials and properties are represented in introduction part.

In chapter 2, the electrical properties investigated to understand the effect of introducing transition metals to the proton conductor oxides such as conductivity, proton containing species and transport number. The introduction of transition metals caused a decrease in proton conductivity in most electrolytes and the electrical conductivity increased or decreased depend on the choice of *A*– and *B*–site as well as various atmospheres. At these transition metals, it is likely that the electrical property contributes significantly to the partial conductivity and proton transport number of electrolytes.

In chapter 3, the electrode activity the transition metal doped and parent

electrolytes were evaluated testing fuel cell performance. $BaCe_{0.85}Y_{0.1}Mn_{0.05}O_{3-\delta}$ was found to have a poor cathode and cell performance, which lower than that of $BaCe_{0.85}Y_{0.1}Co_{0.05}O_{3-\delta}$ and $BaCe_{0.85}Y_{0.1}Fe_{0.05}O_{3-\delta}$ electrolyte examined in fuel cell mode. The order of the decreased in overpotential of $BaCe_{0.85}Y_{0.1}M_{0.05}O_{3-\delta}$ correspond to accordance with results of proton conductivity. Therefore, the decrease in conductivity due to the introduction of the transition metal affects the increase in the electrode overpotential for fuel cell.

In chapter 4 investigated the reasons for the highest conductivity of $SrZr_{0.5}Ce_{0.4}Y_{0.1}O_{3-\delta}$ in $SrZr_{0.9-x}Ce_xY_{0.1}O_{3-\delta}$ system, and effects of Ba substitution and the doping level of Y on the crystal structure. The electrical properties, proton concentration as well as chemical stability of $A(Zr_{0.5}Ce_{0.4})_{1-x}Y_xO_{3-\delta}$ (A= Ba, Sr and x=0.1, 0.2). $Ba(Zr_{0.5}Ce_{0.4})_{0.8}Y_{0.2}O_{3-\delta}$ shows a maximum proton concentration limit of 17.1 mol % compared to only 6.03 mol % for $Sr(Zr_{0.5}Ce_{0.4})_{0.8}Y_{0.2}O_{3-\delta}$ and retained the highest proton conductivity of 1.4×10^{-2} Scm^{-1} in wet 1 % H_2 at 600 °C. $Ba(Zr_{0.5}Ce_{0.4})_{0.8}Y_{0.2}O_{3-\delta}$ shows the most performance in proton conductivity, concentration and mobility for $A(Zr_{0.5}Ce_{0.4})_{1-x}Y_xO_{3-\delta}$ system.

In chapter 5, the influences of In- and Y-doping on the electrical conduction properties of barium zirconate were investigated. The electrical conductivity measured on of $BaZr_{1-x-y}In_xY_yO_{3-\delta}$ (x=0, 0.1, 0.2 and y=0, 0.1, 0.2) could be understood that yttrium doping causes high bulk conductivity and indium doping leads to lowering activation energy of the grain boundary. Co-doping of yttrium and indium promotes the enhancement effect of improving the bulk conductivity and lowering of activation energy, and it is thus expected that the co-doping with yttrium and indium can work for

controlling the bulk and grain boundary conduction specifically in the materials.

Finally, the general summary and further investigation are represented in Chapter 6.

Contents

Abstract **3**

Contents **6**

Chapter 1. General introduction **11**

1.1 Background 11

1.2 Hydrogen energy system 13

1.3 Principle of water electrolysis 17

1.4 Proton conducting materials 20

1.4.1 Perovskite type structure and defect chemistry 20

1.4.2 The electrical conductivity 21

1.4.3 Chemical stability 23

1.4.4 Proton transport number 25

1.5 Electrochemical cell applications 27

1.5.1 Protonic ceramic fuel cell 28

1.5.2 Solid oxide electrolysis cell 29

1.5.3 Hydrogen pump 31

1.6 Purpose of this study 33

1.7 Reference.....34

Chapter 2. Electrical properties of transition metal doped proton conducting perovskites type electrolytes..... 38

2.1 Introduction 38

2.2 Experimental 41

2.2.1 Preparation of transition metals doped electrolytes by solid state reaction and chemical solution method 41

2.2.2 Characterization 42

2.3 Result and discussion 43

2.3.1 Phase identification of 5 mol % doped transition metal on $(Ba/Sr)(Ce/Zr)_{0.85}Y_{0.1}M_{0.05}O_{3-\delta}$ 43

2.3.2 The electrical conductivity of 5 mol % doped transition metal on $(Ba/Sr)(Ce/Zr)_{0.85}Y_{0.1}M_{0.05}O_{3-\delta}$ 47

2.3.3 FT-IR Spectroscopy of 5 mol % doped transition metal on $(Ba/Sr)(Ce/Zr)_{0.85}Y_{0.1}M_{0.05}O_{3-\delta}$ 52

2.3.4 The electromotive force of 5 mol % doped transition metal on $(Ba/Sr)(Ce/Zr)_{0.85}Y_{0.1}M_{0.05}O_{3-\delta}$ 55

2.4 Conclusion.....65

2.5 Reference.....67

Chapter 3. Effects of transition metal oxides doped electrolytes on the performance of PCFC.....70

3.1 Introduction.....70

3.2 Experimental.....77

3.2.1 Preparation of BCYM electrolytes and PCFC cells.....77

3.2.2 Fuel cell performance.....78

3.3 Result and discussion.....80

3.3.1 Resistance of anode and cathode electrodes by impedance spectroscopy.....80

3.3.2 Electrode overportential of transition metals doped BCY electrolytes and PCFC performance.....82

3.4 Conclusion.....86

3.5 Reference.....87

Chapter 4. Effect of dopant levels on the electrical properties of $Ba(Zr_{0.5}Ce_{0.4})_{1-x}Y_xO_{3-\delta}$ and $Sr(Zr_{0.5}Ce_{0.4})_{1-x}Y_xO_{3-\delta}$ proton conducting materials for hydrogen production.....90

4.1 Introduction.....90

4.2 Experimental 92

4.2.1 Preparation of BZCY and SZCY electrolytes 92

4.2.2 Characterization 94

4.3 Results and discussion.....96

4.3.1 Proton-conducting properties of $SrZr_{0.9-x}Ce_xY_{0.1}O_{3-\delta}$ based materials.....96

4.3.2 Phase identification and microstructures of BZCY and SZCY electrolytes 103

4.3.3 The electrical conductivity of BZCY and SZCY electrolytes....107

4.3.4 Proton concentration of BZCY and SZCY electrolytes 111

4.4 Conclusion.....119

4.5. Reference.....121

Chapter 5. Investigation of the electrical conductivity in indium and yttrium-doped barium zirconates proton conducting material..... 125

5.1 Introduction 125

5.2 Experimental 130

5.2.1 Preparation of $BaZr1-x-yIn_xY_yO_{3-\delta}$ electrolytes by chemical solution method 130

5.2.2. Characterization.....132

5.3 Result and discussion.....133

5.3.1 Characteristic of Y- and In-doped barium zirconate proton conducting materials.....133

5.3.2 Characteristic of Y and In co-doped barium zirconate proton conducting materials.....138

5.4 Conclusion.....142

5.5 Reference.....144

Chapter 6. Conclusion..... 146

6.1 General summary..... 146

Outlook for future plan..... 148

Acknowledgments..... 149

Chapter 1

General introduction

1.1 Background

Advances in science and technology have brought us many benefits. The rapid industrial growth in many countries has led to a growing need for energy in all parts of industry, commerce, transportation, education, medical and residential facilities. According to the "The British Petroleum Co. (BP)" latest report, energy consumption grew even faster, while the largest percentage of energy source is from fossil fuel, including coal, oil, and natural gas (Fig. 1.1) [1].

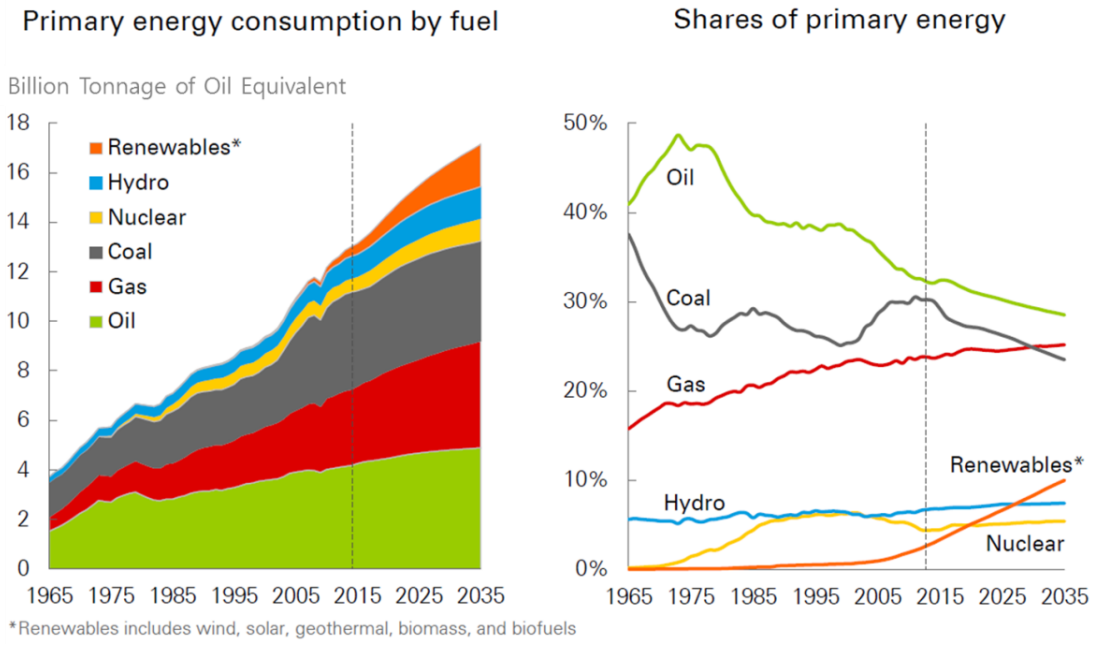

Fig. 1.1 Information of primary energy consumption by fuel in world [1]

World consumption of primary energy remarkably increased from 3.8 billion tons of oil equivalent in 1965 to 13 billion tons of oil equivalent in 2015. Energy consumption in developing countries are expected to continue increasing rapidly owing to high economic growth, rising populations and ongoing industrialization. Burning fossil fuels has been considered as the most economic ways to generate electricity. Fossil fuel, however, is a finite resource. Also, most countries rely primarily on foreign imports of coal, oil and gas market forces of supply and demand. The hazardous chemicals from fossil fuel combustion cause people, especially vulnerable groups such as children and the elderly, to be diagnosed with ailments such as heart disease, cancer and respiratory disease and developmental impairments [2]. In addition, fossil fuel produces vast quantities of 'green house gases' such as carbon dioxide. Human activities like the burning of fossil fuels are major reasons for greenhouse gas emissions, which lead to climate change. Given the effects of climate change, governments and scientists around the world have been seeking ways to reduce the utilization of fossil fuel. Both developing and developed countries are aiming to use cleaner, less polluting, energy [3,4]. Since those ideas, there is an increasing worldwide interest in the renewable energy including wind, such as solar energy and hydrogen energy. Renewable energy resources could be utilized for energy efficiency improvements over wide geographical areas, in contrast to fossil fuels, which are concentrated in a limited number of countries. Rapid deployment of renewable energy and energy efficiency, and technological diversification of energy sources, would result in significant energy security and economic benefits.

1.2 Hydrogen energy system

Hydrogen, the lightest element, is the first element on the periodic table. Therefore, it rises in the atmosphere and is also rarely found in its pure H_2. Although, hydrogen is most abundant element in the universe, it can be mostly available in combined compounds with other elements in hydrogen production [5].

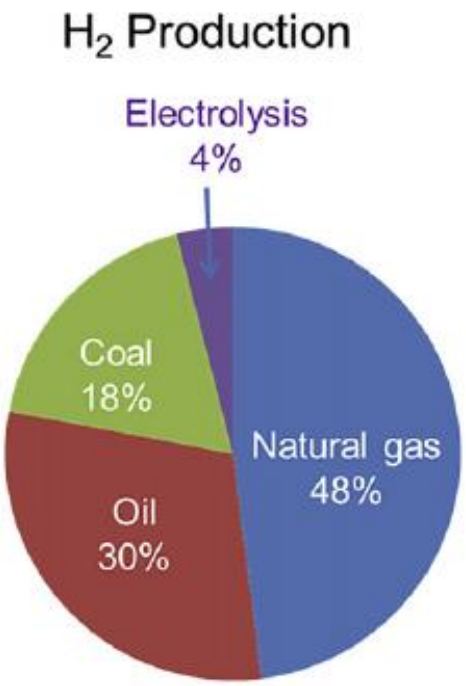

Fig. 1.2 World hydrogen productions [6]

Hydrogen can be produced from a number of sources, such as water, hydrocarbon fuel, biomass, hydrogen sulfide, boron hydrides, and chemical elements with hydrogen. Among them, around 95 % of hydrogen produced is generated from fossil fuel (Fig. 1.2)

[6]. The major source is natural gas, such as methane (CH_4). Steam-methane reformation and partial oxidation can be applied to produce hydrogen with thermal processes. Steam reforming involves the endothermic conversion of methane and water vapor into hydrogen and carbon monoxide (1.1). This heat is often supplied from the combustion of the methane feed-gas. The process typically occurs at temperatures from 700 to 850 °C and in pressures from 3 to 25 bar. The product gas contains around 12 % CO, which can be further converted to CO_2 and H_2 through the water-gas shift reaction (1.2) [7,8].

$$CH_4 + H_2O \rightarrow CO + 3H_2 \qquad (1.1)$$

$$CO + H_2O \rightarrow CO_2 + H_2 \qquad (1.2)$$

In case of coal, it is often noted as the best resource for economically producing large quantities of hydrogen, because of its relatively low cost [9]. A typical reaction for the process is given in equation (1.3), in which carbon is converted to carbon monoxide and hydrogen.

$$C + H_2O \rightarrow CO + H_2 \qquad (1.3)$$

Therefore, carbon dioxide can be considered as a major exhaust in all production of hydrogen from fossil fuel. As previously mentioned, fossil fuel is not the best way for energy generation. Alternatively, water electrolysis is a promising option for hydrogen production from renewable resources. Water electrolysis is a process for separation of water into hydrogen and oxygen. The reaction takes place in a unit called an electrolyzer. In a flame of pure hydrogen gas, burning in air, the hydrogen reacts with oxygen to

form water and release energy.

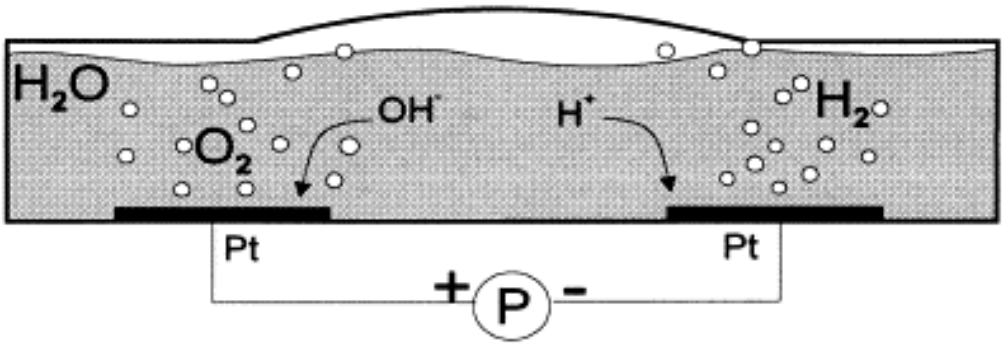

Fig.1.3 Sketch of an electrochemical cell [10]

The electrolysis of water is the reverse reaction to produce oxygen and hydrogen gas from water. In Fig. 1.3, a schematic of a sealed electrochemical cell is shown. The cell is filled with pure water and has two electrodes which are connected with an external power supply. At a certain critical voltage between both electrodes, the electrodes start to produce hydrogen gas at the negatively biased electrode and oxygen gas at the other one. The amount of gas evolved per unit time is directly related to the current passing the cell. In water solution, there is always a certain percentage ionic species; H^+ and OH^- represented by the equilibrium equation [10]:

$$H_2O \leftrightarrow H^+ + OH^- \qquad (1.4)$$

Oxygen and hydrogen gas can be generated at noble metal electrodes by the electrolysis of water:

$$\text{Anode: } 4OH^- \leftrightarrow 2H_2O + O_2 + 4e^- \qquad (1.5)$$

$$\text{Cathode: } 2H^+ + 2e^- \leftrightarrow H_2 \qquad (1.6)$$

In case of acidic or basic water, the reactions which occur at the electrode interface are slightly different. In water electrolysis, there are no side reactions that could yield undesired byproducts. The overall reaction is shown below:

$$\text{Overall reaction: } 2H_2O \leftrightarrow 2H_2 + O_2 \qquad (1.7)$$

The required electricity to produce hydrogen may be obtained by conventional power plants, such as petroleum or nuclear energy. The renewable energy resources such as wind and solar power also can be considered for accomplishing zero greenhouse emissions [11-14]. Hydrogen can be produced via water/steam electrolysis that uses electricity generated from renewable energies, and fuel cells can convert from the hydrogen energy into electricity (Fig. 1.4) [15].

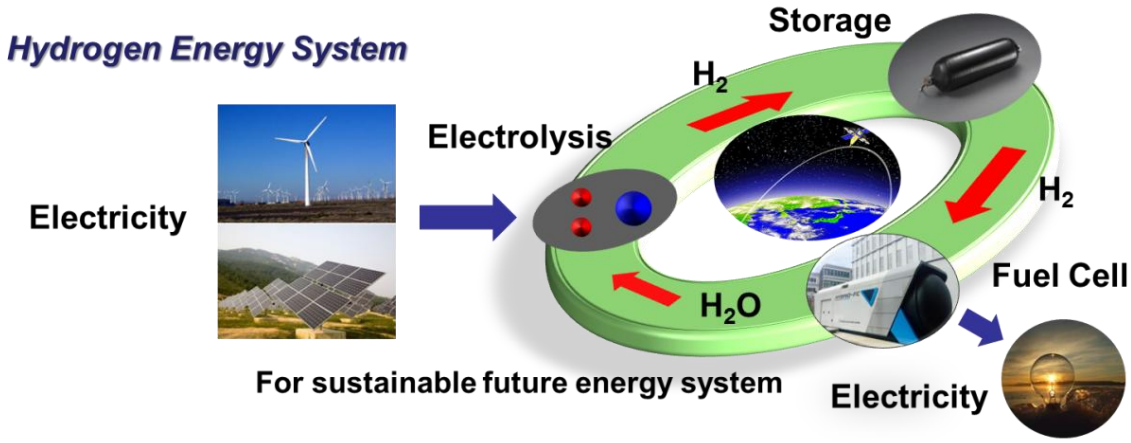

Fig. 1.4 Schematic illustration of a hydrogen energy system

This hydrogen system has many potential advantages. Unlike fossil fuel, hydrogen emits only water as it react with oxygen. So hydrogen promises can greatly cut emissions of carbon dioxide. Furthermore, hydrogen can be produced with renewable energy, and hydrogen utilization will also promote stability in the supply of energy. Finally, a fuel cell vehicle leads to a significant reduction in airborne pollutants and runs much more quietly. Based on these reason, hydrogen can be considered a realistic next-generation energy that can be readily accepted.

1.3 Principle of water electrolysis

Electrolysis of water is the decomposition of H_2O into O_2 and H_2 due to an electric current being passed through the water. Using the relevant values of thermodynamic properties at temperature 25 ^oC and 1 atmosphere pressure, the process must provide the energy for the dissociation plus the energy to expand the gases produced, affording a change in enthalpy as shown in table 1.1.

Table 1.1 Thermodynamic properties of reaction in water

Quantity	H_2O	H_2	0.5 O_2	Change
Enthalpy	-285.83 kJ	0	0	ΔH = 285.83 kJ
Entropy	69.91 J/K	130.68 J/K	0.5 x 205.14 J/K	$T\Delta S$ = 48.7 kJ

At temperature 25 ^{o}C and 1 atmosphere pressure, the thermodynamic analysis on the total Gibbs free energy change is shown as;

$$\Delta G = \Delta H - T\Delta S \qquad (1.8)$$

where ΔG, ΔH, T and ΔS are Gibbs free energy, enthalpy change, absolute temperature and entropy change. The change in the Gibbs free energy is equal to the change in the enthalpy of the system minus the change in the product of the temperature times the entropy of the system. The amount $T\Delta S$ can be provided from the environment temperature T. Therefore, Gibbs free energy can be calculating as;

$$\Delta G = \Delta H - T\Delta S = 285.83 \text{ kJ} - 48.7 \text{ kJ} = 237.13 \text{ kJ} \qquad (1.9)$$

This Gibbs free energy can be related to the Nernst Equation,

$$\Delta G = -nFE \qquad (1.10)$$

where n is the number of electrons involved in the electrolysis reaction, F is Faradays constant (96485 C/mol) and E is the ideal potential of the cell. For this reaction, the cell potential value of the water electrolysis cell (E) at 25 °C for 1 atm is 1.23 V. The Gibbs free energy change of reaction can be also expressed by the following equation,

$$\Delta G = \Delta G^{o} + RT \ln Q \qquad (1.11)$$

where ΔG^{o} is the change of Gibbs free energy at reaction with hydrogen and oxygen in standard state pressure and temperature. Also, R and Q are the ideal gas constant and reaction quotient, respectively. According to the equilibrium constant Eq (1.10 and 11), the equation can be rearranged to following equation,

$$E = E^o + \frac{RT}{nF} \ln Q \qquad (1.12)$$

where the equilibrium constant base on the reaction (1.7) can be written as next equation,

$$E = E^o + \frac{RT}{2F} \ln \frac{P_{H_2} \cdot (P_{O_2})^{1/2}}{a_{H_2O}} \qquad (1.13)$$

where P_{H_2}, P_{O_2}, a_{H_2O} are partial pressure of hydrogen, oxygen and activity of water respectively. The theoretical potential value of water electrolysis cell (E_{theo}) is shown in following equation;

$$E_{theo} = E_A - E_C = E^O + \frac{RT}{2F} \ln \frac{P_{H_2} \cdot (P_{O_2})^{1/2}}{a_{H_2O}} \qquad (1.14)$$

where E_A and E_C are equilibrium potential of anode and cathode. The electrodes equilibrium potential as following equations;

$$E_A = E_{O_2} + \frac{RT}{2F} \ln \frac{a_{H_2O} \cdot (P_{O_2})^{1/2}}{(a_{OH^-})^2} \qquad (1.15)$$

$$E_C = E_{H_2} + \frac{RT}{2F} \ln \frac{P_{H_2} \cdot (a_{OH^-})^2}{(P_{H_2O})^2} \qquad (1.16)$$

where E_{O_2} and E_{O_2} are standard electrode potential of O_2 and H_2. Also, a_{OH^-} is activity of OH^-. These equations can be rearranged to can be rearranged to

$$E^O = E_{O_2} - E_{H_2} = \frac{\Delta G}{2F} \qquad (1.17)$$

These Nernst equations are available in transport number and cell performance on the proton conducting materials.

1.4 Proton conducting materials

1.4.1 Perovskite type structure and defect chemistry

Proton conductor based on barium, strontium, cerates and zirconates have been regarded as traditional perovskite type electrolytes materials in solid oxide fuel cell (SOFC) and protonic ceramic electrolysis cell (PCEC) for decades at intermediate temperature [16-25]. The perovskite structure has the general formula ABO_3, where the A-site is a metal with a divalent cation and the B-site with a tetravalent cation, respectively. For example, $SrCe_{0.9}Y_{0.1}O_{3-\delta}$ proton, conducting perovskite material, is partially substituted with a trivalent yttrium to create oxygen vacancies. In Kröger-Vink notation, the equation can be written as;

$$Y_2O_3 + 2Ce_{Ce}^{x} + O_O^{x} \rightarrow 2Y_{Ce}' + V_o^{\cdot\cdot} + 2CeO_2 \qquad (1.18)$$

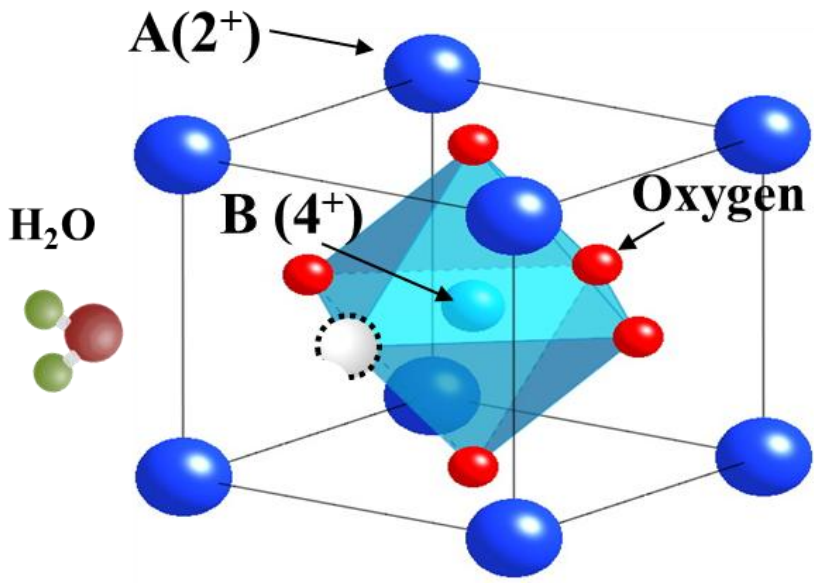

Fig. 1.5 Perovskite unit cell of $AB_{1-x}M_xO_{3-\delta}$

The A-site cations are located at the corners of the unit cell with B-site cations in the center as shown in Fig. 1.5. The oxygen ions are at the centers of each face of the unit cell. In moist atmospheres, ambient water molecules incorporate into the oxide ion vacancies to form protons that make hydrogen bonds to the lattice oxygen. The proton can move from the oxygen atom to another by breaking and forming the hydrogen bonds with the oxygen atoms repetitively.

$$H_2O + V_{\ddot{o}} + O_O^x \leftrightarrow 2OH_O^{\cdot} \qquad (1.19)$$

In Kröger-Vink notation this reaction is given that two hydroxide ions substitute for oxide ions, i.e., two positive charged protonic defects ($OH_O^{\cdot}$) are formed. This phenomenon implies that such oxides show some oxide ion conductivity in the dry state and have an affinity for chemical diffusion for water, which has advantages for application of such oxides in fuel cells [26].

1.4.2 The electrical conductivity

Iwahara et al., were among the first time to reported that ABO_3 perovskites oxides has the proton conductivity of in 1981 [16]. After his research, many researchers have evaluated that cerates and zirconates based perovskites can have remarkable proton conductivity [27-30]. The electrical conductivity of typical proton conductor in moist hydrogen atmosphere can be observed in Fig. 1.6. According to the study of Matsumoto et al., cerates have high protonic conductivity. On the other hand, zirconates based electrolytes shows low protonic conductivity [15]. It is suggested that the

electrical conductivity can change depending on the A- or B-site materials and compositions. In addition, proton conductor has lower activation energy than that of oxide ion conductor.

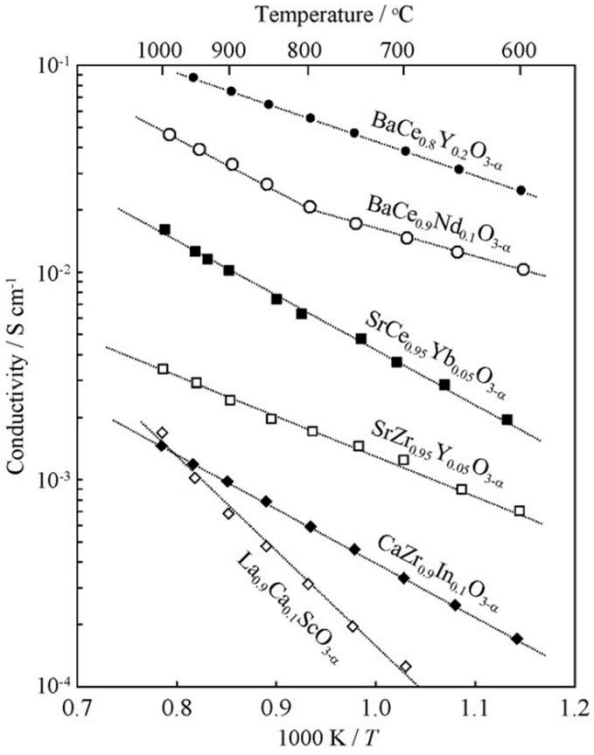

Fig. 1.6 The electrical conductivity of typical proton conductor in moist hydrogen [15]

Fig. 1.7 shows that comparison of the electrical conductivity between the 8 mol% Y_2O_3 stabilized ZrO_2 (8YSZ) and $BaCe_{0.9}Y_{0.1}O_{3-\delta}$ (BCY91) samples [31]. These electrolytes have comparable conductivities at 900 ^oC. While temperature declined to 600 ^oC, however, the electrical conductivities of BCY91 have significantly higher than 8YSZ due to small temperature dependence. Thus, activation energy of proton conduction is

smaller than that of oxide ion conduction, and this material can be applied for intermediate temperature fuel cell devices. It is indicated that such low operation temperature can regarded as an advantage in the material cost and heat management of electrochemical cells.

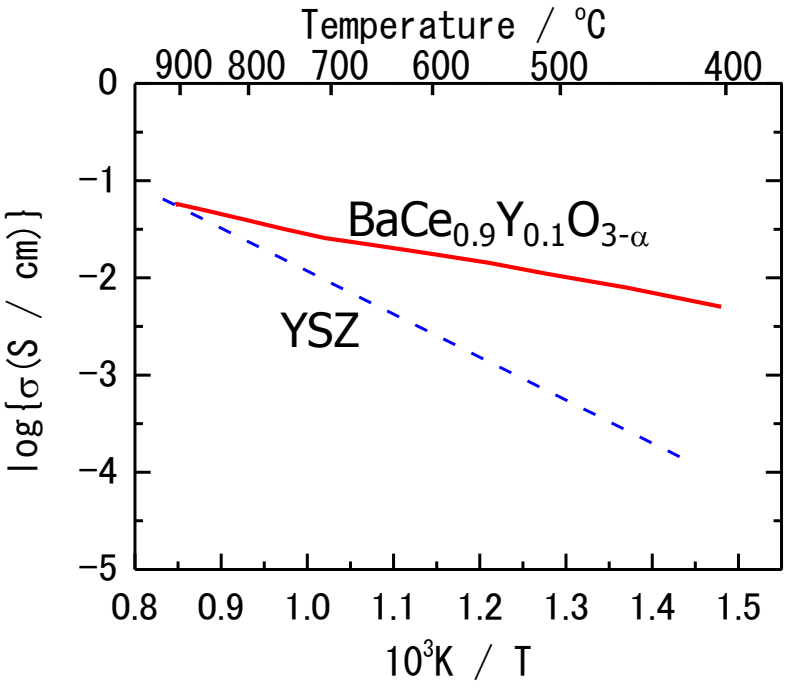

Fig. 1.7 Comparison of the electrical conductivities of 8YSZ and BCY91 [31]

1.4.3 Chemical stability

Although the cerate based electrolytes are shown to have high proton conduction at intermediate temperature (Fig. 1.6), thermodynamically less stable and reactions with CO_2 and H_2O to decompose into cerium oxide and alkaline earth

carbonates have been considered as problems. Those reactions are in reaction (1.20) or alkaline earth hydroxides reaction (1.21).

$$BaCeO_3 + CO_2 \rightarrow BaCO_3 + CeO_2 \qquad (1.20)$$

$$BaCeO_3 + H_2O \rightarrow Ba(OH)_2 + CeO_2 \qquad (1.21)$$

Zirconate oxides are characterized by high chemical stability, but the conductive are not as high as cerate oxides. Cerate oxides show lower chemical stability than zirconate oxides in same conditions.

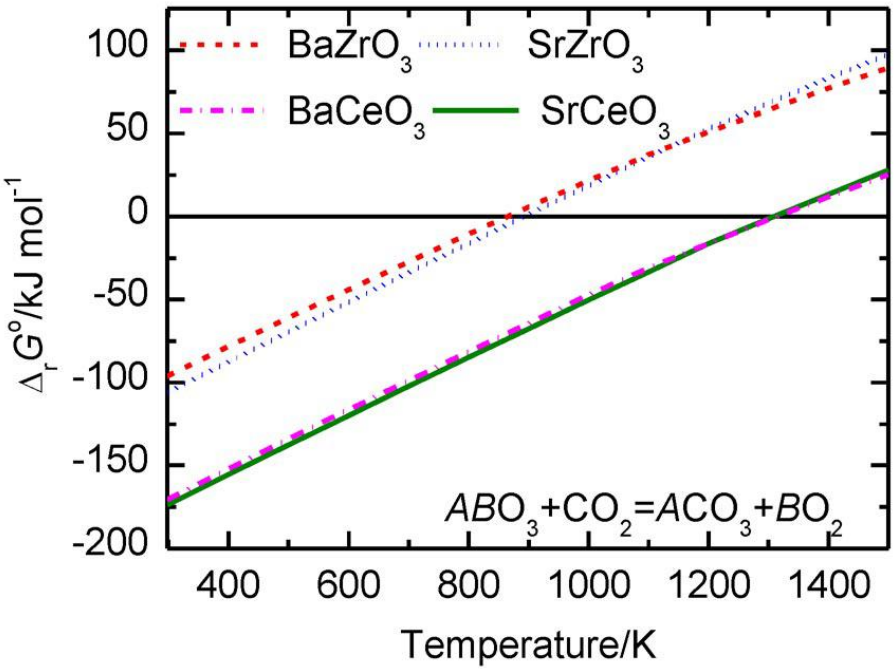

Fig. 1.8 Standard Gibbs free energy of carbonation of ABO_3 as a function of temperature calculated from a thermodynamic database [33]

The chemical stability is explained by thermodynamics [31-33]. Fig. 1.8 shows the Gibbs free energy, revealing that cerates and zirconates samples can react with carbon dioxide at 1 bar at 1300 °C and 900 °C, respectively. Therefore, the cerates can be used under condition that carbon dioxide can be minimized. These reactions cause serious decomposition of the material and limit applications in electrochemical devices in severe conditions, such as conditions under hydrocarbon or high humidity. Furthermore, zirconate based electrolytes exhibits excellent stability under CO_2, rendering it highly attractive for applications in extreme conditions.

1.4.4 Proton transport number

Perovskite type oxide solid solutions exhibit the electrical conductivity in atmospheres containing hydrogen, oxygen and steam at high temperatures. Also, the conductivity of each ionic species is directly proportional to the density of mobile ions *n*, which are carrying a charge q with mobility μ. The ionic conduction of proton conducting material is as following equation;

$$\sigma_{ion} = nq\mu \qquad (1.22)$$

As ion conduction consists of conduction of oxide and proton, should be evaluated proton transport number from electromotive force measurement (EMF). In other words, the electrical conductivity of a proton conductor can be measured under various oxygen, hydrogen and steam partial pressures and at a temperature range. Through those measurements the total conductivity of the material can be obtained. The total

conductivity combines with the EMF measurement in a concentration cell and steam concentration cell to determine transport numbers for oxide ions and protons under a similar set of conditions. A good understanding of total and partial conductivities is provided. The EMF method is based on cell voltage measurement on a sample composed with two reversible electrodes to a gradient in chemical potential. The voltage measured over the sample will then be equal to follows,

$$E_{EMF} = -\frac{RT}{nF}(t_i)\, ln\frac{P''}{P'} \qquad (1.23)$$

where t_i, R, T, n and F, are ionic transport number, gas constant, temperature, number of moles of electrons transferred, Faraday's constant, p' and p'' are the partial pressures of activities at both electrodes. This theoretical voltage calculated from Nernst equation. It has a very important definition of ionic transport number of the electrolytes from measured value and calculated value;

$$t_i = \frac{E_{EMF}}{E_{Nernst.}} \qquad (1.24)$$

For electrolytes where both oxide ionic and protonic conductivity is expected, the equilibrium between hydrogen, oxygen and water vapor should be taken into account, and the total EMF developed over the sample can be calculated as;

$$E_{EMF} = -(t_{H^+} + t_{O^{2-}})\frac{RT}{2F}\ln\frac{P_{H_2}(\mathrm{II})}{P_{H_2}(\mathrm{I})} + t_{O^{2-}}\frac{RT}{2F}\ln\frac{P_{H_2O}(\mathrm{II})}{P_{H_2O}(\mathrm{I})} \qquad (1.25)$$

where $t_{O^{2-}}$, and t_{H^+}, are oxide and proton transport number, $P_{H_2}(\mathrm{I})$, $P_{H_2}(\mathrm{II})$, $P_{H_2O}(\mathrm{I})$ and $P_{H_2O}(\mathrm{II})$ are the partial pressures of hydrogen and water at both electrodes. For the EMF measurements, Pt electrodes painted on both surface, and moist hydrogen flowed

into the sample. For the EMF of hydrogen concentration cell, water partial pressures were fixed with both sides. Flowing mixtures of Ar-H_2 gasses were provided to each side with different H_2 concentrations of 1-100 %, respectively. In the EMF of steam concentration, hydrogen partial pressures were same with both side, therefore, first term of equation (1.25) can be ignore. The dry gas was bubbled through water, and mixing the dry and wet gas can be control of the water content of the gas (Fig. 1.9).

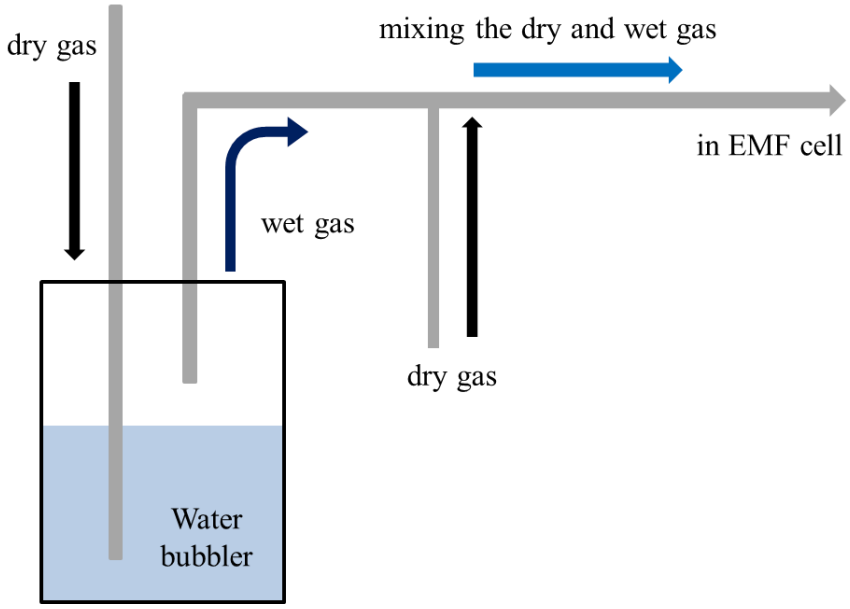

Fig. 1.9 Schematic illustration of water partial pressures setup

1.5 Electrochemical cell applications

1.5.1 Protonic ceramic fuel cell

Fuel cell is environmentally friendly devices for energy conversion and power

generation, and is one of the most promising candidates as a zero-emission power sources. A fuel cell is an electrochemical device that converts chemical energy of reactants directly into electrical energy, and does not need to be charged as with conventional batteries. Also, fuel cells do not generate carbon dioxide to create noiseless useful energy as compared to internal combustion engines. Based on these advantages, fuel cells have attracted the world's attention, and the development of fuel cell is being aggressively pursued by nearly every automobile manufacturer, as well as manufacturers of power systems for portable electronic devices. The PCFC reaction can be separation into two electrochemical half-cell reactions with oxidation reaction taking place at anode and reduction reaction at cathode as shown:

$$\text{Anode: } 2H_2 \rightarrow 4H^+ + 4e^-$$

$$\text{Cathode: } O_2 + 4H^+ + 4e^- \rightarrow H_2O$$

$$\text{Overall: } 2H_2 + O_2 \rightarrow 2H_2O \qquad (1.26)$$

PCFC is consisting of an anode, a cathode, and a proton conducting electrolyte that allows proton to move between the two sides of the fuel cell. The proton migrates through the electrolyte after the reaction. At the same time, electrons are migration from the anode to the cathode through an external circuit, producing direct current electricity. At the cathode side, oxygen reacts with protons, electrons to produce water. A schematic illustration of PCFC is shown in figure 1.10. This electrochemical device generates electrical power from hydrogen fuel. Also, the critical advantage is relatively low operating temperatures (500–700 °C) because the proton conducting material has higher conductivity and lower activation energy in intermediate temperature than that of oxide

ion conductor.

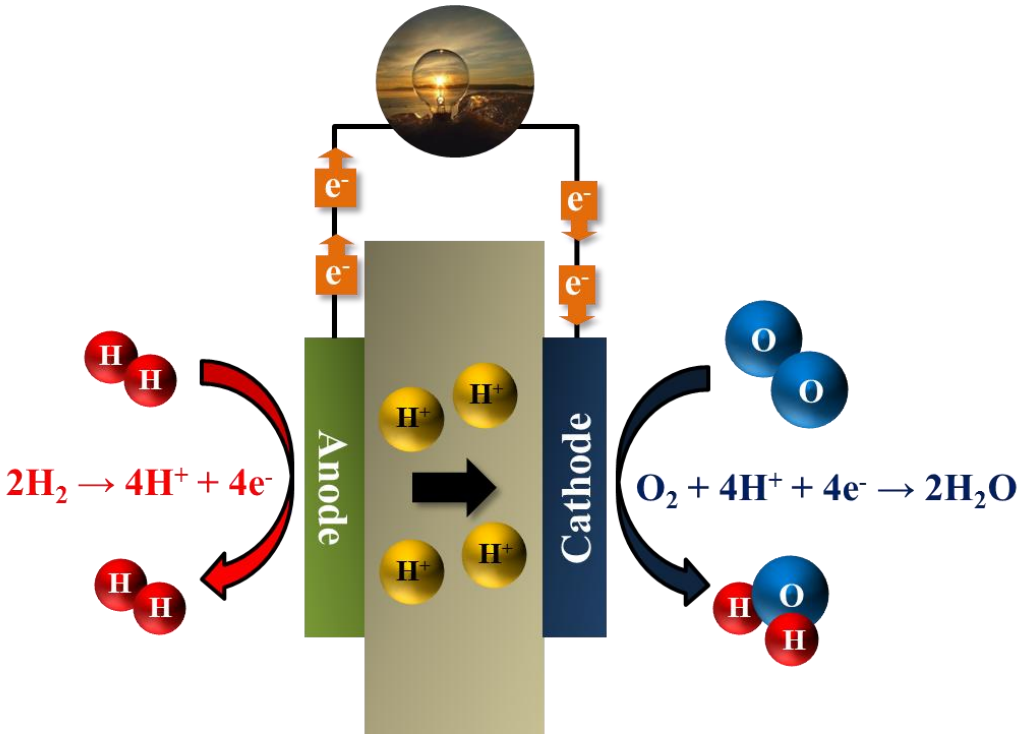

Fig. 1.10 Schematic of the processes taking places in a PCFC

1.5.2 Solid oxide electrolysis cell

When a protonic ceramic fuel cell is operated in a reverse mode to steam electrolysis to generate hydrogen, then it is called a solid oxide electrolysis cell (SOEC). Steam electrolysis produces high purity hydrogen directly with no additional devices. Water electrolysis proceeds during 600 to 800 °C in SOECs. The anode and cathode reactions for the SOEC represented in figure 1.11 are as shown in below;

Anode: $2H_2O \rightarrow O_2 + 4H^+ + 4e^-$

Cathode: $4H^+ + 4e^- \rightarrow 2H_2$

Overall: $2H_2O \rightarrow 2H_2 + O_2$ (1.27)

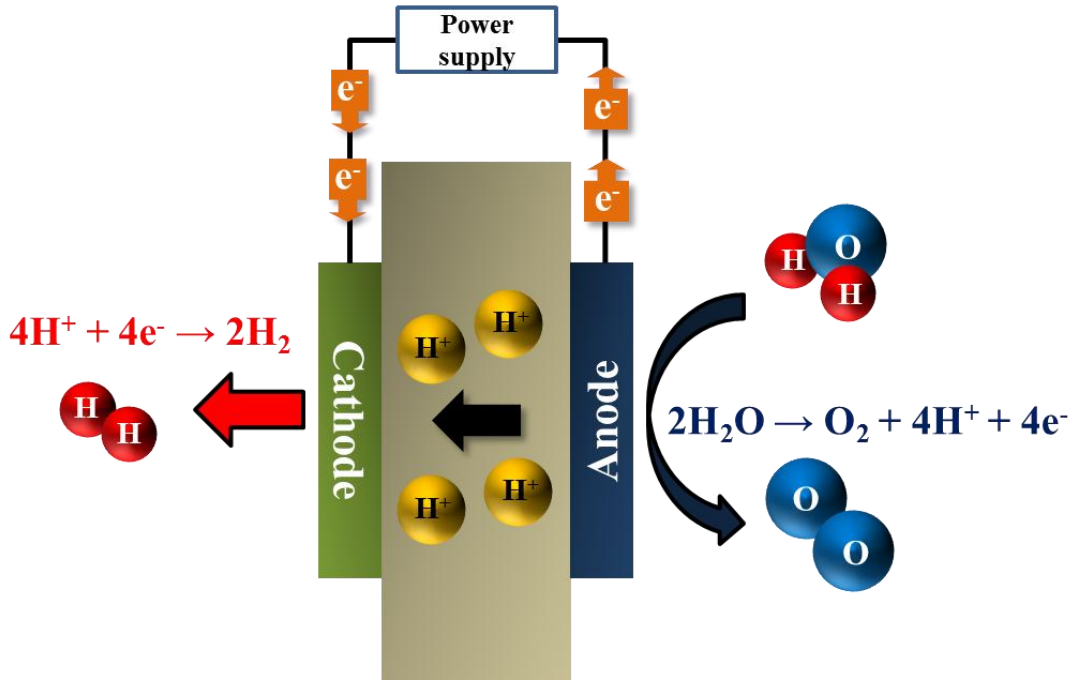

Fig. 1.11 Schematic of the processes taking places in a SOEC

The SOEC is to separate steam into pure H_2 and O_2. This cell is consisting of an anode, a cathode, and a proton conducting electrolyte that allows proton to move between the two sides of the electrolysis cell. The protons migrate from the anode to the cathode through the electrolyte during the reaction. The electrons transport from the anode to the cathode through an external circuit at the same time. At the cathode, protons and

electrons react to form hydrogen gases. Based on these reactions, SOEC produces pure hydrogen and oxygen gases in each electrode. SOEC is very effective when unutilized for hydrogen generation when a source of high temperature wastes steam, such as the outlet of steam turbines at a nuclear power plant.

1.5.3 Hydrogen pump

The proton conductors allow selective transport of hydrogen, and thus are most attractive in application of hydrogen separation. As previous mention, around 95 % of hydrogen is produced from fossil fuels. Of that, the most used sources are natural gas for about 50 % of the global production: natural gas is a naturally occurring hydrocarbon gas mixture consisting primarily of methane. Methane steam reforming reaction is the most efficient technology for convert methane to useful hydrogen. Methane steam reforming reaction is a highly endothermic process in which Ni-based catalysts are employed to produce synthesis gas, usually around a 1:3 of CO/H_2 ratio, at elevated temperatures (800–1000 ^{o}C) [34-38]. Schematic of illustration in Fig. 1.12 is a device of a membrane reactor with proton conducting material for pure hydrogen production. The cell reaction of hydrogen production and separation are listed as following reactions;

$$\text{Anode: } CH_4 + 2H_2O \rightarrow CO_2 + 8H^+ + 8e^-$$

$$\text{Cathode: } 8H^+ + 8e^- \rightarrow 4H_2$$

$$\text{Overall: } CH_4 + 2H_2O \rightarrow CO_2 + 4H_2 \qquad (1.28)$$

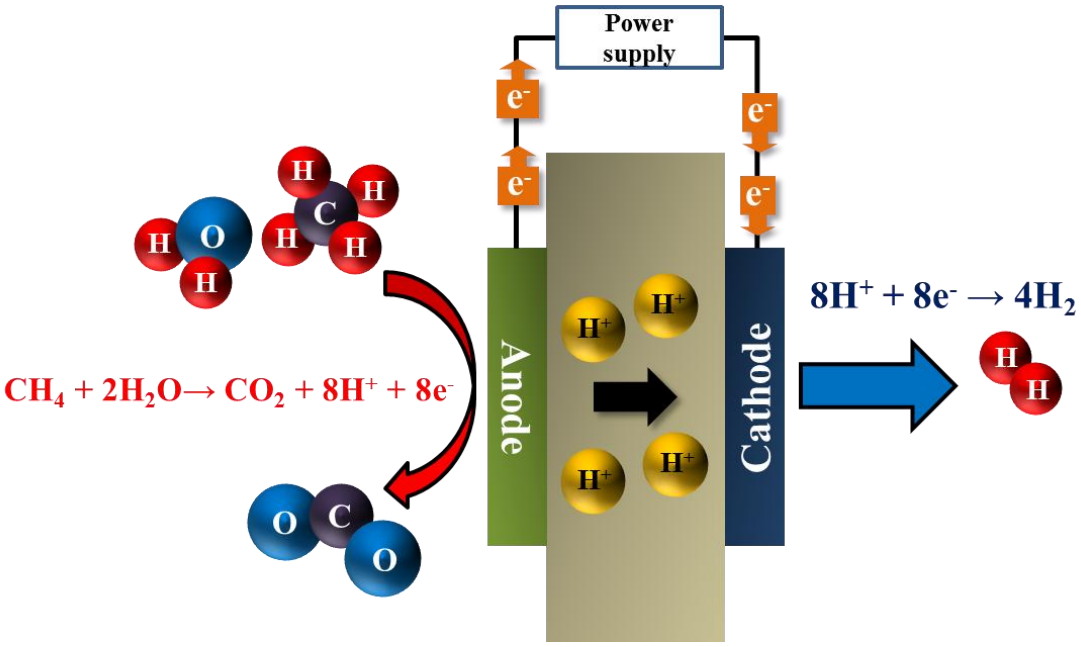

Fig. 1.12 Schematic of the processes taking places in a methane steam reforming cell

At high temperature and in the metal-based catalyst (typically nickel-based catalyst), steam reacts with methane to produce carbon dioxide in anode side. The protons migrate through the electrolyte after the reaction. At the same time, electrons are migration from the anode to the cathode through an external circuit, at cathode, protons react with electrons to produce hydrogen. Using a methane steam reforming cell, it is relatively easy to separate hydrogen from the carbon in the hydrocarbon and then use hydrogen. Thus, steam reforming of hydrocarbon gases is regarded as a potential way to provide fuel for fuel cells.

1.6 Purpose of this study

This study has focused on the electrical properties of electrolytes based on the proton conducting materials. Fuel cell performance and electrolytes compatibility to electrodes were evaluated. The main focuses of this study are shown as follows:

1. The electrical properties of proton conducting perovskite type oxide electrolytes
2. Influence of transition metals doping on the electrical properties and cell performance of proton conducting electrolytes.

Proton conducting materials has been investigated in the past few years in terms of materials design and cell performance. Especially, trivalent cation doped barium zirconate cerates ($BaZr_{1-x-y}Ce_xM_yO_{3-\delta}$) based electrolytes have been extensively studied. This composition based electrolytes shows high conductivity and cell performance. However, many researchers lack of interest about effect of transition metals for electrolytes. Through the this study, the effect of transition metals doping on the proton conducting perovskite electrolytes was investigated, also it will be utilized to further assist in selecting suitable oxide electrode or dopant materials. Furthermore, the final objective of this study is related to the reduction of carbon dioxide emission to save human and nature beings from environmental pollution.

1.7 Reference

[1] “Primary Energy” The British Petroleum Co., BP Energy outlook 2017, http://www.bp.com/

[2] F. P. Perera, *Environmental Health Perspectives*, 116 (2008) 987–999

[3] M. Ni, Dennis Y. C. Leung, Michael K. H. Leung, K. Sumathy, *Fuel Process. Tech.*, 87, 461 (2006)

[4] M. Bafat, *Int. J. of Hydrogen Energy*, 33 (2008) 4013–4029

[5] “Hydrogen.” *The Columbia Encyclopedia*, 6th Ed. Columbia University Press, 2001

[6] R. Lan, J. T. S. Irvine, S. Tao, *Int. J. of Hydrogen Energy*, 37 (2008) 1482–1494

[7] G. E. Marnellos, C. Athanasiou, S. S. Makridis, E. S. Kikkinisdes, *Hydrogen-based Autonomous Power Systems*, Springer, ISSN 1612-1287 (2008), P. 25

[8] K. Aasberg-Petersen, J.-H. Bak Hansen, T. S. Christensen, I. Dybkjaer, P. S. Christensen, C. S. Nielsen, S. E. L. W. Madsen, J. R. Rostrup-Nielsen, *Appl. Catal. A.*, 221 (2001) 379–387

[9] J. A. Turner, *Science*, 305 (2004) 972–974

[10] C. Neagu, H. Jansen, H. Gardeniers, M. Elwenspoek, *Mechatronics*, 10 (2000) 571–581

[11] A. Marshall, B. Børresen, G. Hagen, M. Tsypkin, R. Tunold, *Energy*, 32, (2007) 431–436

[12] A. Marshall, *A review of technology and current research*, August (2003)

[13] K. Sim, S. Moon, S.-T. Choo, *Hydrogen Information*, No. 4,1 (2004)

[14] B. Sorensen, *Hydrogen and Fuel Cells, Elsevier Academic Press*, Heidelberg (2005)

[15] H. Matsumoto, T. Sakai, Y. Okuyama, *Pure Appl. Chem.*, 85 (2013) 427–435

[16] H. Iwahara, T. Esaka, H. Uchida, N. Maeda, *Solid State Ionics*, 3/4 (1981) 359–363

[17] H. Iwahara, H. Uchida, S. Tanaka, *Solid State Ionics*, 9–10 (1983) 1021–1026

[18] N. Sata, M. Ishigame, S. Shin, *Solid State Ionics*, 86–88 (1996) 629–632

[19] S. Shin, H. H. Huang, M. Ishigame, *Solid State Ionics*, 40/41 (1990) 910–913

[20] H. H. Huang, M. Ishigame, S. Shin, *Solid State Ionics*, 47 (1991) 251–255

[21] H. Iwahara, H. Uchida, N. Maeda, *J. Power. Sources*, 7 (1982) 293–301

[22] T. Schober, J. Friedrich, D. Triefenbach, F. Tietz, *Solid State Ionics*, 100 (1997) 173–181

[23] N. Bananos, *Solid State Ionics*, 53–56 (1992) 967–974

[24] H. Iwahara, T. Yajima, H. Ushida, *Solid State Ionics*, 70/71 (1994) 267–271

[25] H. Iwahara, T. Yajima, T. Hibino, K. Ozaki, H. Suzuki, *Solid State Ionics*, 61 (1993) 65–69

[26] K. D. Kreuer, *Annu. Rev. Mater. Res.*, 33 (2003) 333–359

[27] C. Zuo, S. Zha, M. Liu, M. Hatano, M. Uchiyama, *Adv. Mater.*, 18 (2006) 3318–3320

[28] Y. Yang, S. Wang, K. Blinn, M. Liu, Z. Liu, Z. Cheng, M. Liu, *Science*, 326 (2009) 126–129

[29] D. Pergolesi, E. Fabbri, A. D'Epifanio, E. D. Bartolomeo, A. Tebano, S. Sanna, S. Licoccia, G. Balestrino, E. Traversa, Natuer Materials, 9 (2010) 846–852

[30] K. Leonard, Y. S. Lee, Y. Okuyama, K. Miyazaki, H. Matsumoto, *Int. J. of Hydrogen Energy*, 37 (2017) 3926–3937

[31] Matsumoto, *Proton-Conducting Ceramics: From Fundamentals to Applied Research*, Pan Stanford Publishing (2016) 352–361

[32] H. Matsumoto, T. Shimura, H. Iwahara, T. Higuchi, K. Yashiro, A. Kaimai, T. Kawada, J. Mizusaki, J. Alloys Compd., 408–412 (2006) 456–462

[33] H. Matsumoto, S. Okada, S. Hashimoto, K. Sasaki, R. Yamamoto, M. Enoki, T. Ishihara, *Ionics*, 13 (2007) 93–99

[34] V. Kyriakou, I. Garagounis, A. Vourros, E. Vasileiou, A. Manerbino, W. G. Coors, M. Stoukides, *Appl. Catal. B Environ.*, 186 (2016) 1–9

[35] A. T. Ashcroft, A. K. Cheetham, J. S. Foord, M. L. H. Green, C. P. Grey, A. J. Murrell, P. D. F. Vernon, *nature*, 344 (1990) 319–321

[36] Z. Liu, K. W. Jun, H. S. Roh, S. E. Park, *J. Pow. Sources*, 111 (2002) 283–287

[37] R. Chaubey, S. Sahu, O. O. James, S. Maity, *Renewable and Sustainable Energy*

Reviews, 23 (2013) 443–462

[38] S. D. Angeli, G. Monteleone, A. Giaconia, A. A. Lemonidou, *Int. J. of Hydrogen Energy.*, 39 (2014) 1979–1997

Chaper2

Electrical properties of transition metal doped proton conducting perovskites type electrolytes

2.1 Introduction

Proton-conducting oxides have been studied as intermediate-temperature electrolyte materials for fuel cells and steam electrolysis [1-6]. These materials can operate at intermediate temperatures because the activation energy for proton conductivity is lower than that of oxide ion conductivity. Solid electrolytes are crucial and indispensable component of fuel cells and electrolyzers, governing the performance and to a large extent the design of the system. Oxides containing transition metals, such as (La,Sr)(Co,Fe)O_3 (LSCF), (Ba,Sr)(Co,Fe)$O_{3-\delta}$ (BSCF), (La,Sr)MnO_3 (LSM), (Sm,Sr)CoO_3 (SSC) are commonly untilized as electrodes for either SOFCs or electrolyzers [7-24]. During preparation and operation of the fuel cells, transition metals have been considered to diffuse from the electrodes to the electrolyte. There is a concern that the diffused transition metals would degrade the electrolyte conductivity. For this reason, researches on the reaction between electrode and electrolyte have been the interested in the subject recently. Shimura et al. reported that a significant decrease in the electrical conductivity of $BaCe_{0.9}Y_{0.1}O_{3-\delta}$-based (BCY) proton conductors on partially substituting Fe, Mn and Co for Ce [25]. The electrical conductivity of transition metal doped $BaCe_{0.9-x}Y_{0.1}M_xO_{3-\delta}$ (M = Co, Fe, Mn and x = 0.05, 0.075, 0.1) in

air atmosphere are shown in Fig.2.1. From these data show apparent that transition metal doping decreases the conductivity in air. The magnitude of the decrease is the largest in Mn-doped solutions and the smallest in Co-doped solutions (Mn > Fe > Co). In addition, conductivity of $BaCe_{0.9-x}Y_{0.1}M_xO_{3-\delta}$ in air can be considered as independent of x, as shown in the Fig.2.1. The research proved those transition metals are related to the electrical conductivity decreasing for BCY system.

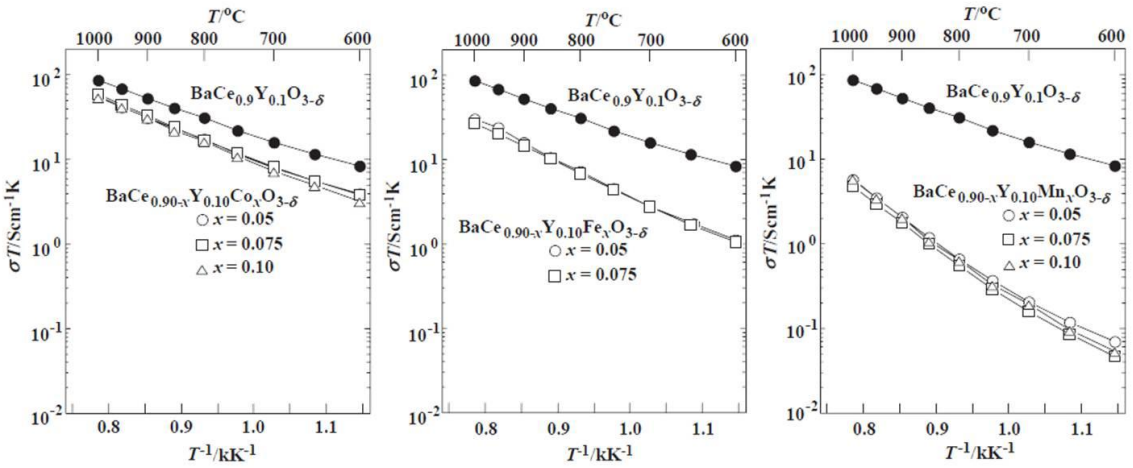

Fig.2.1 The electrical conductivity of $BaCe_{0.9-x}Y_{0.1}M_xO_{3-\delta}$ in air atmosphere [25]

A similar tendency has been observed in the present study and is discussed in the subsequent section. In a nutshell, decreasing electrical conductivity related to transition metal diffusion might not only contribute to increasing ohmic loss of the electrolytes but also might significantly affect the electrode performance. If assumed that the electrode-reaction takes place at the triple phase boundary as illustrated in Fig. 2.2, then the electrode reaction might be influence by the proton conductivity of the electrolyte remarkably. And the influence becomes significantly larger at the interface between the

electrode and the electrolyte since the diffused transition metals also take place simultaneously at this point. Meanwhile, many researchers have investigated to $BaZr_{1-x-y}Ce_xY_yO_{3-\delta}$ [26-28] and $SrZr_{1-x-y}Ce_xY_yO_{3-\delta}$ [29] electrolytes system in recently. This is because these materials show high conductivity and cell performance. Thus, this study is also employed for understanding the effect of transition metal The foundation of based electrolytes such as a $BaCe_{0.9-x}Y_{0.1}M_xO_{3-\delta}$, $BaZr_{0.9-x}Y_{0.1}M_xO_{3-\delta}$, $SrCe_{0.9-x}Y_{0.1}M_xO_{3-\delta}$ and $SrZr_{0.9-x}Y_{0.1}M_xO_{3-\delta}$ system were utilized in this research. Also, this research can assist in selecting suitable oxide electrode materials.

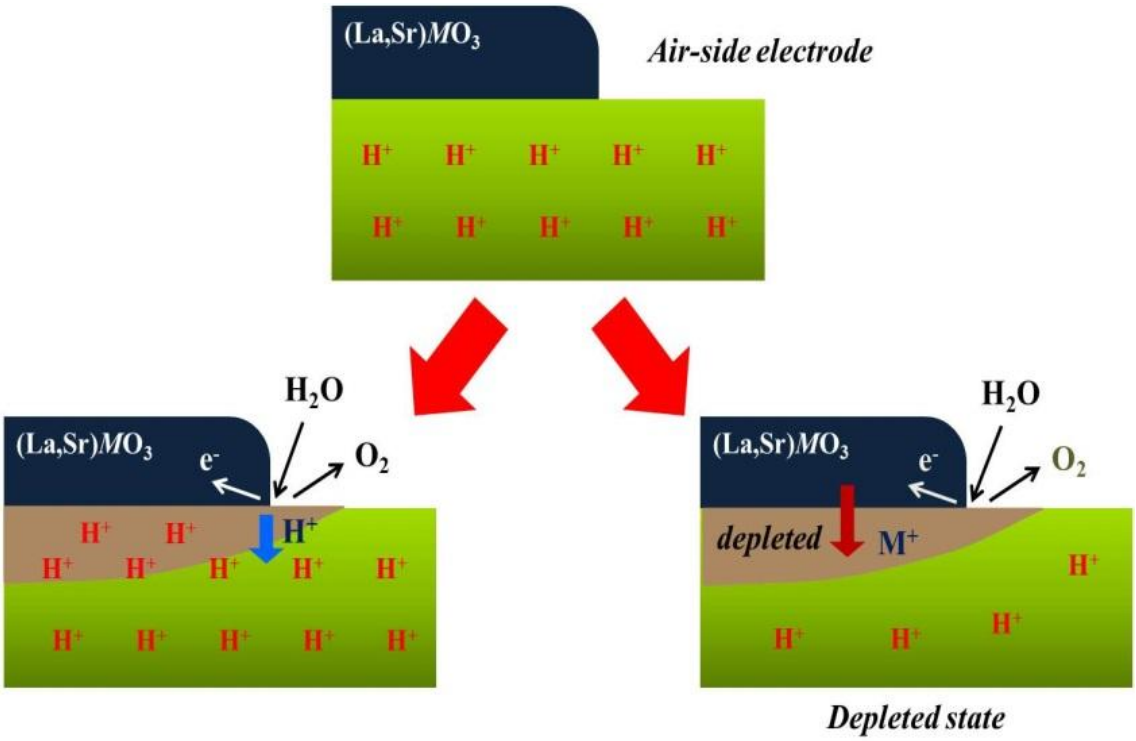

Fig. 2.2 A schematic illustration of possible decrease in electrode activity due to proton depletion

In this chapter, transition metal doping of perovskite type oxide have been performed, i.e., $BaCe_{0.85}Y_{0.1}M_{0.05}O_{3-\delta}$, $BaZr_{0.85}Y_{0.1}M_{0.05}O_{3-\delta}$, $SrCe_{0.85}Y_{0.1}M_{0.05}O_{3-\delta}$ and $SrZr_{0.85}Y_{0.1}M_{0.05}O_{3-\delta}$ which are referred to hereafter as BCYM, BZYM, SCYM and BZYM, or transition-metal-specifically as BCYCo, BCYFe, BCYMn, BZYNi, BZYCo, BZYFe, BZYMn, BZYNi, SCYCo, SCYFe, SCYMn, SCYNi, SZYCo, SZYFe, SZYMn and SZYNi, respectively (*M*= Co, Fe, Mn and Ni), and their electrical conduction properties investigated to understand the effect of introducing transition metals to the proton conductor oxides.

2.2 Experimental

2.2.1 Preparation of transition metals doped electrolytes by solid state reaction and chemical solution method

(Ba/Sr)$(Ce/Zr)_{0.85}Y_{0.1}M_{0.05}O_{3-\delta}$ (BCYM, SCYM and SZYM) and (Ba/Sr)$Ce_{0.9}Y_{0.1}O_{3-\delta}$ (BCY, SCY and SZY) were prepared by a solid-state-reaction method, using $BaCO_3$ (Rare metallic, 99.99 %), $SrCO_3$ (Rare metallic, 99.99 %), ZrO_2 (Tosoh, 99.9 %), CeO_2 (Rare metallic, 99.99 %), Y_2O_3 (Mitsuwa's pure chemicals, 99.99 %) and transition metal oxides as starting materials. The transition metal oxides Co_3O_4 (Kanto chemical, 99.95 %), Fe_2O_3 (Mitsuwa's pure chemicals, 99.99 %), MnO_2 (High purity chemicals, 99 %) and NiO (Soekawa chemicals, 99.97 %) were utilized. Stoichiometric amounts of the appropriately weighed powders were mixed in a mortar with ethanol and then pressed in to a pellet. The pellets were subsequently calcined at 1000–1200 °C for 10 h in air with regrind. The obtain powders were ball-milled at 300

rpm for 1h , then pressed into pellets at 250 MPa for 10 min, and finally sintered at1400–1600 °C for 10 h in air. $BaZr_{0.85}Y_{0.1}M_{0.05}O_{3-\delta}$ (BZYM) was prepared by a chemical solution method using aqueous solution [30]. Reagent grade metal nitrate of $Ba(NO_3)_2$ (Wako, 99.9 %), $ZrO(NO_3)_2{\cdot}xH_2O$ (Zirconyl nitrate solution, Aldrich, 35 wt %, 99 %), $Y(NO_3)_3{\cdot}nH_2O$ (Wako, 99.9 %), $Co(NO_3)_2{\cdot}6H_2O$ (Kanto chemical, 99.95 %), $Fe(NO_3)_3{\cdot}9H_2O$ (Kanto chemical, 99.9 %) $Mn(NO_3)_2{\cdot}6H_2O$ (Wako, 98 %), $Ni(NO_3)_2{\cdot}6H_2O$ (Wako, 99.9 %) were used. Citric acid (Wako, 99.5 %) and ethylene diamine tetraacetic acid (EDTA, Dojindo, 99 %) were employed as chelating and complexing agents. The molar ratio between total metal cations, EDTA, and citric acid was set at 1:1.5:1.5. After NH_3 solution (Chameleon reagent, 28 %) was add to the solution to adjust the pH to approximately 9 to 10. The aqueous solution was dehydrated on a hot plate at 260 °C, generating a viscous liquid. The dried mixture powders were calcined at 900 ^oC for 10h. The synthesized powders were then ball-milled in ethanol at 300 rpm for 4 days, dried and sieved (150 μm), pressed into pellets at 250 MPa for 10 min and finally sintered at1400–1600 °C for 10 h in air.

2.2.2 Characterization

Phase composition and crystal structure of the transition metals doped electrolytes were characterized using X-ray diffraction (XRD, Cu Kα, 40 kV–40 mA, Rigaku) range from 10^o to 80^o of 2 theta. Infrared absorbance measurements were conducted with a Fourier transform infrared spectrometer (FT/IR-6100 JASCO) at room temperature. The electrical conductivity of transition metals doped electrolytes were measured by a four-terminal AC impedance method (Princeton Applied Research, Versa

STAT 3) at 600 to 900 ^{o}C in moist air and 1%H_2 atmospheres (pH_2O = 1.9 kPa). The electromotive force (EMF) of the gas concentration cells were measured at 600 and 800 ^{o}C in moist H_2 atmosphere. Platinum electrode (Tanaka Kikinzoku Kogyo, TR-7907) was painted on the sample surface, then heat-treat at 950 ^{o}C for 1 h in air. The experimental atmosphere supplied to both electrodes was composed of a gas mixture of the required ratio of H_2/H_2O/Ar or O_2/H_2O/Ar ($P_{H2O(I)}$ = 0.006 – 0.019, $P_{H2O(II)}$ = 0.019, $P_{H2(I)}$ or $P_{O2(I)}$ = 0.01 – 0.98 and $P_{H2(II)}$ or $P_{O2(II)}$ = 0.01).

$$P_{H2(I)} \text{ or } P_{O2(I)} + P_{H2O(I)} + \text{Pt} \mid \text{Electrolytes} \mid \text{Pt} + P_{H2O(II)} + P_{H2(II)} \text{ or } P_{O2(II)}$$

2.3 Result and discussion

2.3.1 Phase identification of 5 mol % doped transition metal on $(Ba/Sr)(Ce/Zr)_{0.85}Y_{0.1}M_{0.05}O_{3-\delta}$

The XRD pattern of transition metals doped and un-doped electrolytes are shown in Fig.2.3. From The XRD patterns of, it is indicated that BCYM, SCYM and SZYM are orthorhombic perovskite structure. Also, BZYM system shows the cubic structure without secondary phase. The relative density obtaining from all the synthesized compositions were above 95 %. However, SCYFe shows the secondary phase with $Sr_2FeO_{4-\delta}$. The ionic radius of the six coordinated Ce^{4+}, Zr^{4+} and Y^{3+} is larger than Co, Fe, Mn and Ni in the same coordination configuration (Ce^{4+} = 87 pm Zr^{4+} = 72 pm, Y^{3+} = 90 pm, Co^{3+} = 61 pm, Fe^{3+} = 64.5 pm, Mn^{3+} = 64.55 pm and Ni^{3+} = 56 pm)[31]. Therefore, it is suggested to get a smaller lattice parameter for transition metal

doped electrolytes. According to the XRD patterns, in these all cases that unit cell volume decreased with the introduction of transition metals.

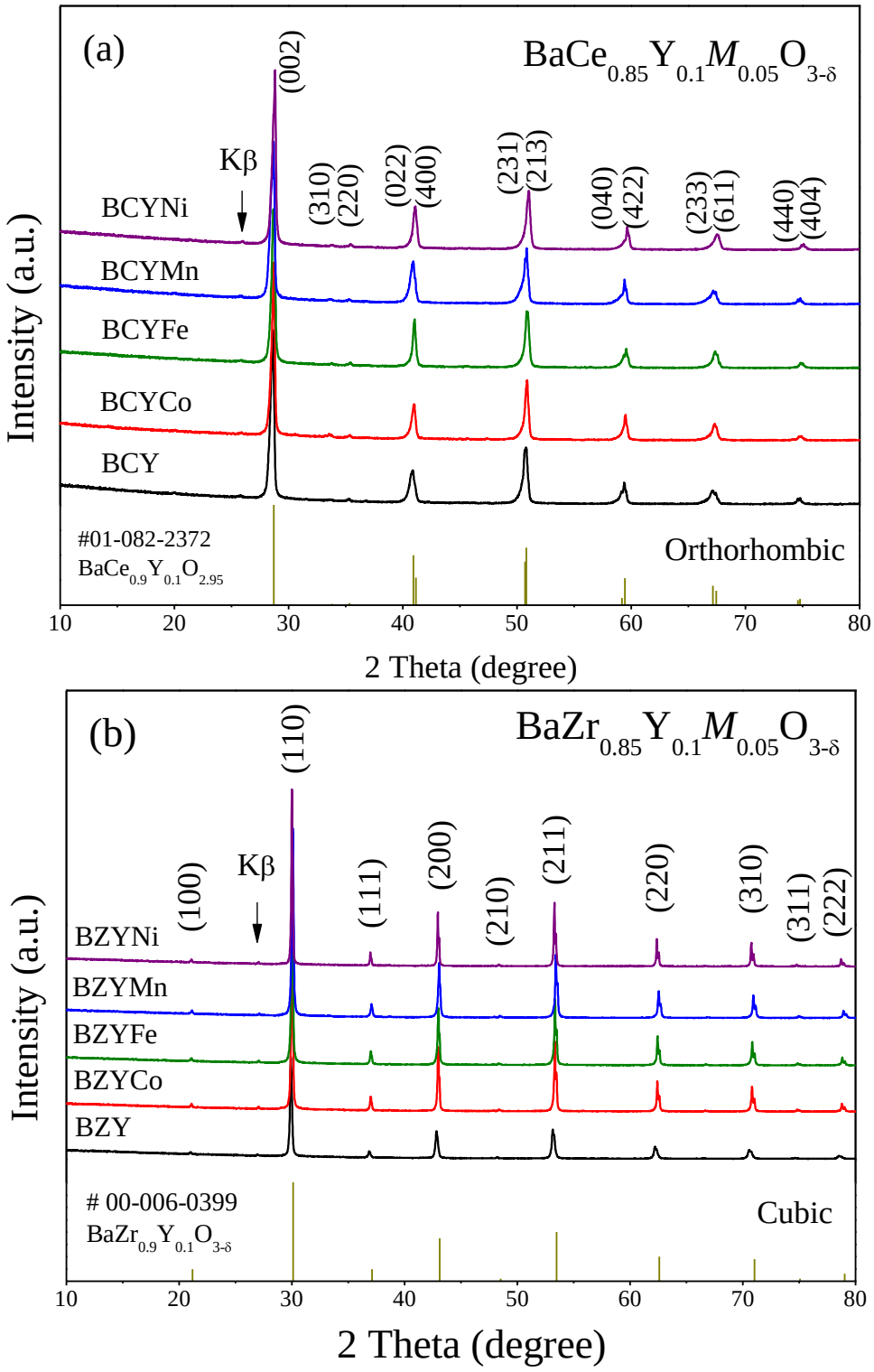

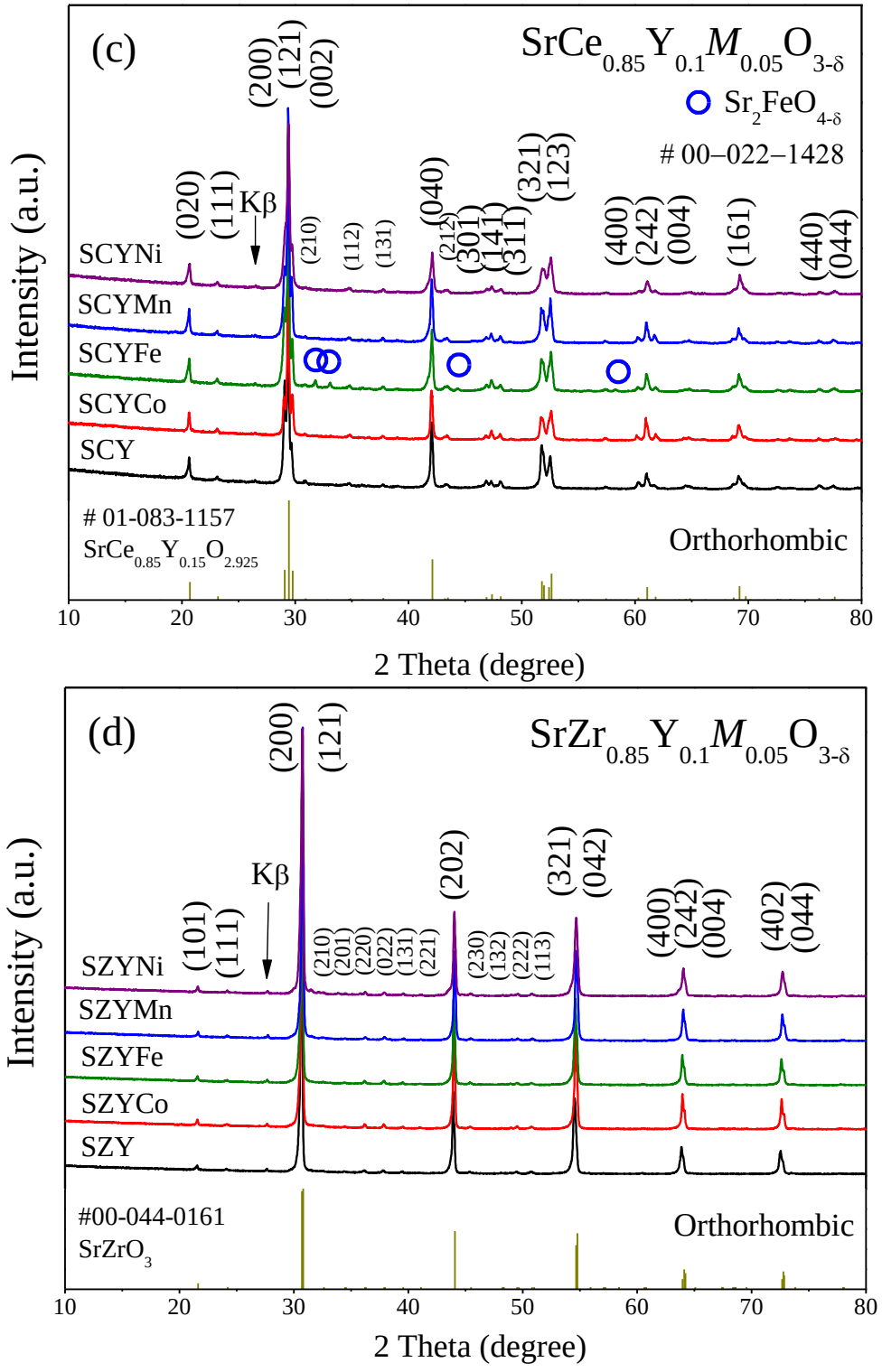

Fig.2.3 The XRD patterns of 5 mol % transition metal doped electrolytes after sintering at 1400–1600 ^{o}C in 10h in air: (a) BCYM, (b) BZYM, (c) SCYM and (d) SZYM

With respect to the BCYM and SCYM system, the calculated unit cell volume also was given as descending sequence BCYNi > BCYFe > BCYCo > BCYMn and SCYNi > SCYMn > SCYFe > SCYCo. The changed volume status shows a different trend for 4 type transition metal doped electrolytes. Thus, the unit cell volume varies, upon the introduction of the transition metals depending on *A* and *B*-site materials.

Table 2.1 The lattice parameter and unit cell volume of (Ba/Sr)(Ce/Zr)$_{0.85}$Y$_{0.1}$*M*$_{0.05}$O$_{3-\delta}$ (*M* = Co, Fe, Mn and Ni)

Sample	**BCY**	**BCYCo**	**BCYFe**	**BCYMn**	**BCYNi**
Structure	Orthorhombic	Orthorhombic	Orthorhombic	Orthorhombic	Orthorhombic
Volume (nm^3)	0.3407	0.3388	0.3387	0.3402	0.3366
Lattice Parameter (nm)	a = 0.8774 b = 0.6230 c = 0.6233	a = 0.8762 b = 0.6219 c = 0.6218	a = 0.8781 b = 0.6206 c = 0.6216	a = 0.8774 b = 0.6230 c = 0.6224	a = 0.8754 b = 0.6203 c = 0.6198

Sample	**BZY**	**BZYCo**	**BZYFe**	**BZYMn**	**BZYNi**
Structure	Cubic	Cubic	Cubic	Cubic	Cubic
Volume (nm^3)	0.0748	0.0743	0.0743	0.0740	0.0745
Lattice Parameter (nm)	a = 0.4214	a = 0.4205	a = 0.4203	a = 0.4198	a = 0.4208

Sample	SCY	SCYCo	SCYFe	SCYMn	SCYNi
Structure	Orthorhombic	Orthorhombic	Orthorhombic	Orthorhombic	Orthorhombic
Volume (nm^3)	0.3166	0.3164	0.3163	0.3161	0.3151
Lattice Parameter (nm)	a = 0.6136 b = 0.8586 c = 0.6010	a = 0.6135 b = 0.8584 c = 0.6008	a = 0.6141 b = 0.8581 c = 0.6002	a = 0.6121 b = 0.8588 c = 0.6014	a = 0.6113 b = 0.8576 c = 0.6010

Sample	SZY	SZYCo	SZYFe	SZYMn	SZYNi
Structure	Orthorhombic	Orthorhombic	Orthorhombic	Orthorhombic	Orthorhombic
Volume (nm^3)	0.5587	0.5570	0.5571	0.5553	0.5549
Lattice Parameter (nm)	a = 0.8235 b = 0.8239 c = 0.8234	a = 0.8227 b = 0.8231 c = 0.8225	a = 0.8229 b = 0.8232 c = 0.8224	a = 0.8221 b = 0.8218 c = 0.8220	a = 0.8217 b = 0.8222 c = 0.8214

2.3.2 The electrical conductivity of 5 mol % doped transition metal on $(Ba/Sr)(Ce/Zr)_{0.85}Y_{0.1}M_{0.05}O_{3-\delta}$

The Arrhenius plots of the total electrical conductivity of BCYM, BZYM, SCYM and SZYM in moist air atmosphere as a function of reciprocal temperature are shown in Fig. 2.4. The electrical conductivity of the materials were calculated with the following equation; $\sigma = l/RA$ where l, R and A are the length of electrolyte, total resistance and cross sectional area, respectively.

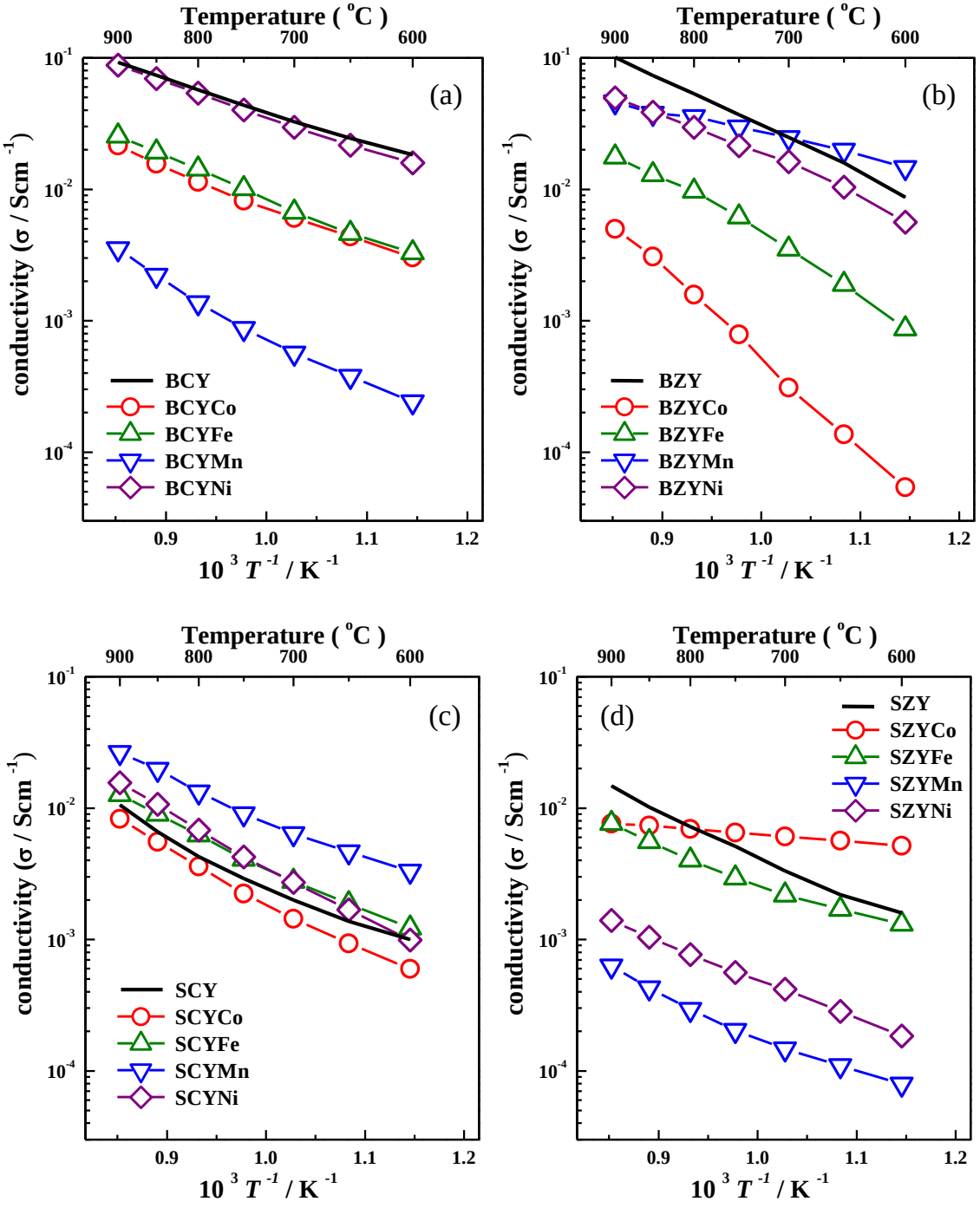

Fig. 2.4 The temperature dependence of the electrical conductivity of 5 mol % doped transition metal on (a) BCYM, (b) BZYM, (c) SCYM and (d) SZYM in moist air atmosphere

According to the result of BCYM system, a decrease in electrical conductivity was observed after introducing the transition metals. The largest magnitude of decrease is BCYMn The electrical conductivity of BCYNi was much closer to that of BCY. Meanwhile, BCYCo and BCYFe electrolytes show the same trend in air atmosphere. In BZYM system, the electrical conductivity was given as descending sequence BZYCo>BZYFe>BZYNi>BZYCo. BZYCo seems to decrease more than one order of magnitude in the electrical conductivity (Fig. 2.4(b)). Meanwhile in SCYM system, the electrical conductivity was minor slightly increased or almost same than the other electrolytes. SCYCo shows a slightly decrease the electrical conductivity than SCY. The other electrolytes were slightly increased with SCYMn. SCYMn in SCYM system shows the most increase in conductivity. According to the plots of SZYM, the electrical conductivity decreases as sequence SZYMn, SZYNi, SZYFe and SZYCo.

Figure 2.5 shows the electrical conductivity of 5% transition metal doping on the electrolytes in 1% H_2 atmosphere. The electrical conductivity was slightly increased or nearly same for SCYM than that of SCY. Meanwhile, BCYM, BZYM and SZYM samples shows decreased tendency. Also, in 1% H_2 atmosphere, it is shows the different tendency to air atmosphere. The electrical conductivity of Co and Mn-doped BCY decreased than that of BCY (Fig. 2.5(a)). Also, in the case of BZYM, it was observed that the electric conductivity decreased after doping with above respective transition metal (Fig. 2.5(b)). The order of decreased in conductivity, is as a sequence Fe > Co = Mn > Ni. These results suggest that Ni based electrode material be best suitable for $BaZr_{1-x}Ce_xY_yO_{3-\delta}$ base electrolyte. In the case of SCYM, a similar tendency as shown in Fig. 2.4(c).

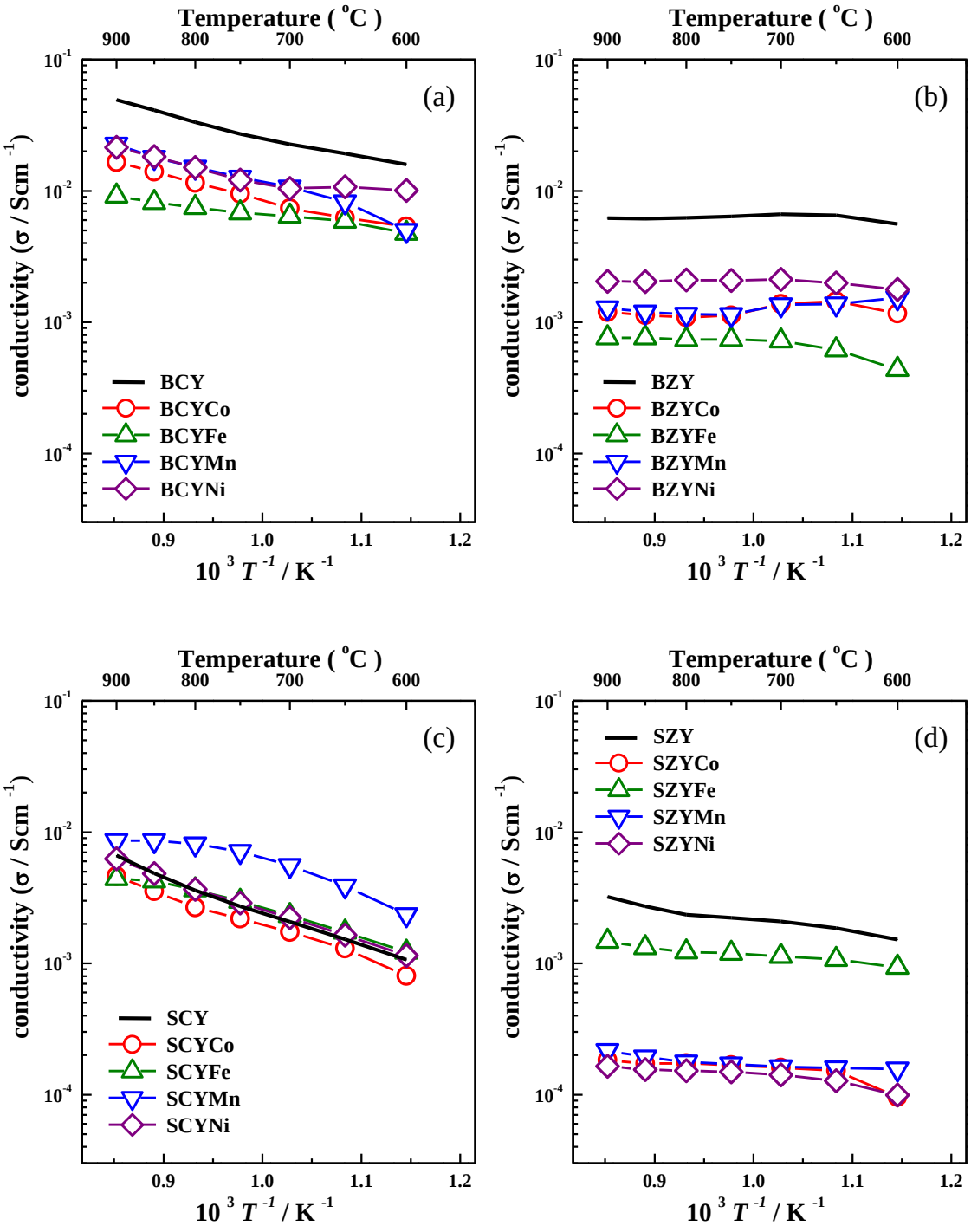

Fig. 2.5 The temperature dependence of the electrical conductivity of 5 mol % doped transition metal on (a) BCYM, (b) BZYM, (c) SCYM and (d) SZYM in moist 1% H_2 atmosphere

Co, Fe and Ni-doped SCY conductivity were also close to that of SCY electrolyte (Fig. 2.5(c)). The magnitude of decrease in this case is the largest in Co, Mn and Ni-doped SZY and the smallest in Fe doped SZY (Fig. 2.5(d)). The results of Ni-doped electrolytes are critical in 1% H_2 atmosphere, because Ni containing materials are commonly applied as cathode electrode for solid oxide electrolysis cells. The electrical conductivity of SZYNi shows magnitude of decrease was larger than BCYNi, BZYNi and SCYNi. Whereas the electrical conductivity of SCYNi was very similar to electrical conductivity of the SCY. A plausible explanation of the decreased conductivity has been proposed in the works of Kreuer. According to reported, reduction of the coordination number tends to reduce proton conductivity [32-34]. The perovskite structure is characterized by high coordination numbers for both types of cation (12 for the *A*-site and 6 for the *B*-site) between adjacent oxide ions which all have the same site symmetry. For a given ion, the ionic radius decreases with decreasing coordination number [31]. Thus, decrease of coordination number reduces oxygen vacancies (BO_6 to BO_5), which means a decrease in the proton conductivity. $BaZrO_3$ [34] and $BaCeO_3$ [35] shows much lower proton conductivity when doped with Sc or In compared with Y as an acceptor dopant, which has a significantly higher ionic radius. These results supported that the reduction of coordination leads to a decrease in conductivity. The transition metal has small ion radius than that of *B*-site cation such as Ce, Zr and Y. Therefore, it can be analogized that the introduced transition metal has a small coordination number compared with *B*-site cation and leads to a decrease in conductivity than that of the parent electrolyte.

2.3.3 FT-IR Spectroscopy of 5 mol % doped transition metal on $(Ba/Sr)(Ce/Zr)_{0.85}Y_{0.1}M_{0.05}O_{3-\delta}$

The presence of proton-containing species within the doped and parent electrolytes was evaluated with FT-IR. Infrared diffuse reflection spectra of O–H stretching vibration regions are used to characterize proton dissolution sites in high temperature proton conductors. Protons bonded to oxygen in the crystals resulting in the formation of hydroxyl groups. These hydroxyl groups can subsequently bond to lattice oxygen. These respective environments can be elucidated to gives the information of protons in the materials. The thermogravimetric analysis (TG) is more suitable for such determination. However, it is not considered since the oxidation states of the doped transition metals have a high tendency to change at higher temperature especially with a change in the gas atmosphere. Figure 2.6 and 2.7 shows the FT-IR spectra of the electrolytes together with the transition metals doped electrolytes in air and 1% H_2 atmosphere. Four broad absorbance bands around 1700-1800 cm^{-1} (band A), and 2400-2500 cm^{-1} (band B), 2800-3100cm^{-1} (band C) and 3500-3800cm^{-1} (band D) which are characteristic O-H stretching vibrational modes are observed [36-39]. Omata et al. reported that the absorption intensities of the O-H bands at band A and B due to M^{3+}–OH–Zr and the bands at band C and D due to M^{3+}–OH–M^{3+} were analyzed as a function of the ion radius of dopant ($SrZr_{0.95}M_{0.05}O_{3-\delta}$, *M*= Ga, Sc, In, Lu, Y and Gd) [39]. The intensity ratios between bands A and B depend on the ion radius of dopant species such as the bigger ionic radius dopant shows higher intensity in the band B side. These absorbance bands can be attributable to bound protons in the materials.

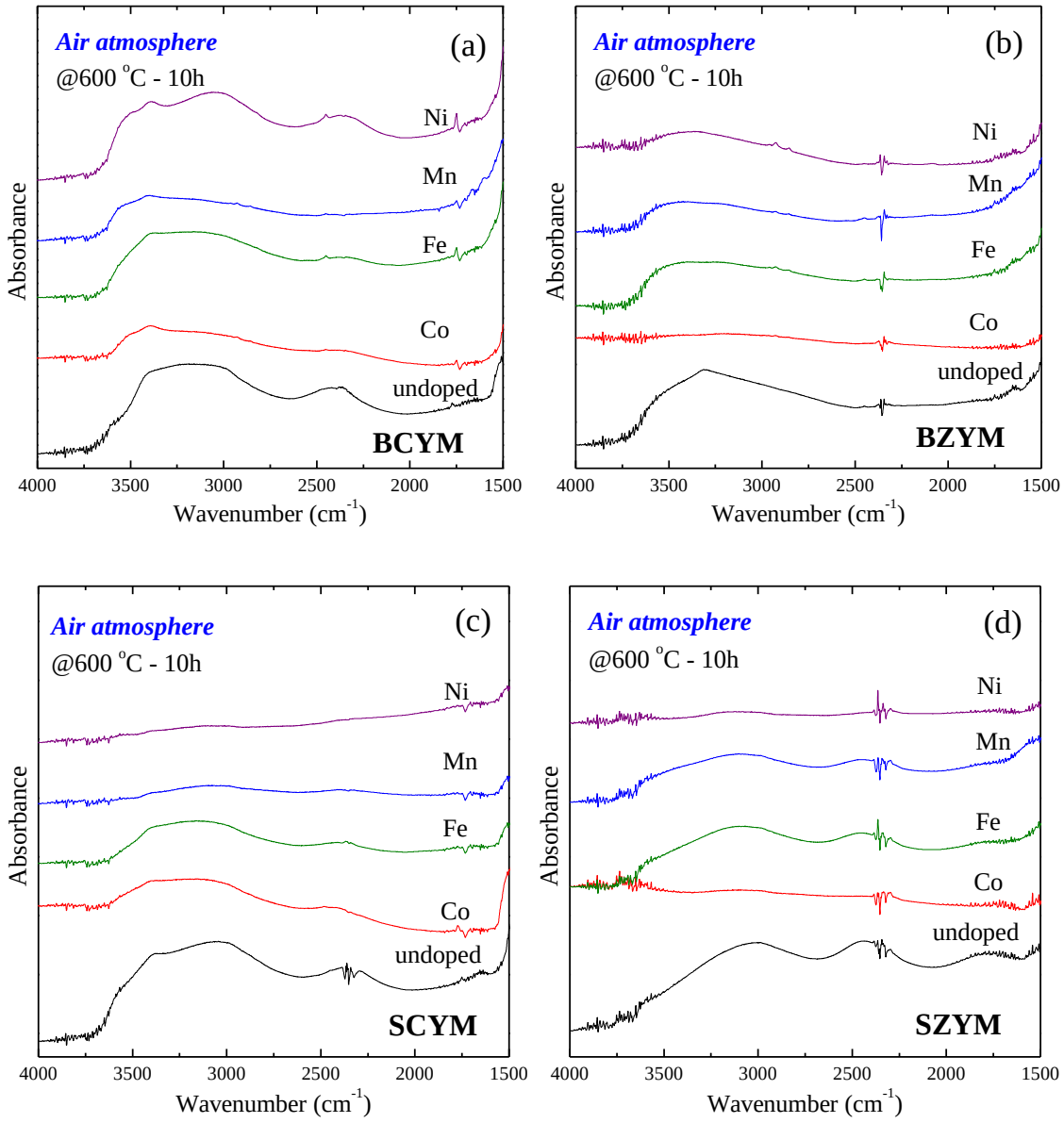

Fig. 2.6 Room temperature FT-IR spectra of 5 mol % doped transition metal on (a) BCYM, (b) BZYM, (c) SCYM and (d) SZYM in air atmosphere. Data for the parent electrolytes are also shown for comparison. The samples were annealed at 600 °C for 10 hours in moist air atmosphere.

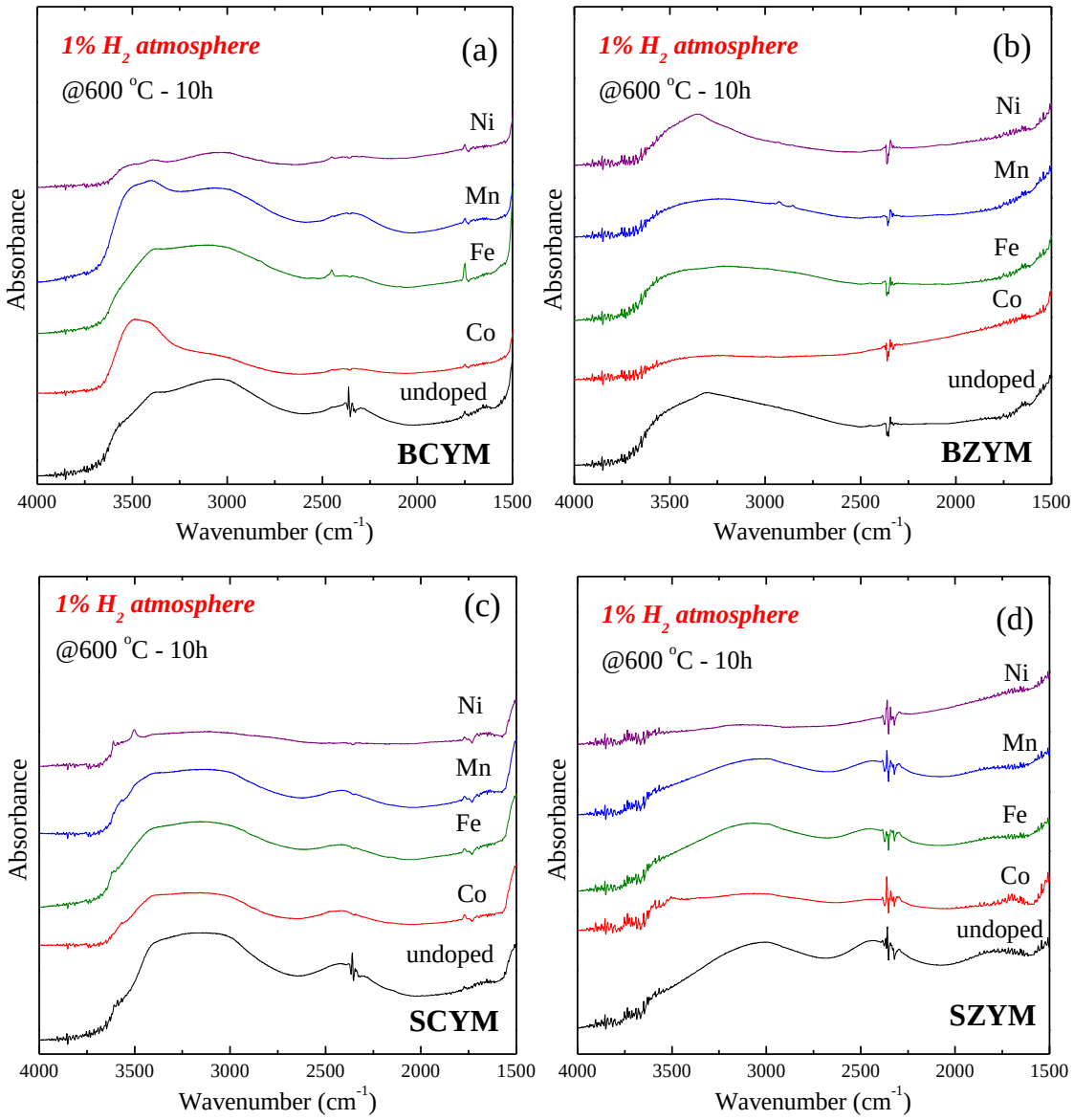

Fig. 2.7 Room temperature FT-IR spectra of 5 mol % doped transition metal on (a) BCYM, (b) BZYM, (c) SCYM and (d) SZYM in air atmosphere. Data for the parent electrolytes are also shown for comparison. The samples were annealed at 600 ^{o}C for 10 hours in moist 1% H_2 atmosphere.

In the case of an electrolyte doped with a transition metal, absorbance bands appear at a higher wavenumber than that of parent electrolyte. Also, the transition metals doped electrolytes in most cases show a decrease in the absorbance intensity, which can be attributed to a decrease in the O-H content and probably the ionic conductivity of the materials. No absorption band was observed in a few samples (BZYCo, SCYNi SZYNi and SZYCo) and the spectrum was almost the same as the tendency the electrical conductivity data in same atmosphere. Consequently, it is shown that proton dissolution have occurred for transition metal doped electrolytes, even though transition metal concentration in the composition were extremely small. The decreases in the absorption intensity of the band of A-D were related to the coordination number of the transition metal. As explained earlier, the coordination number can be changed to BO_5 due to the small ionic radius of the transition metal, leading to a reduction in oxygen vacancy. Therefore, the O-H absorption band can be reduced in all range of bands.

2.3.4 The electromotive force of 5 mol % doped transition metal on $(Ba/Sr)(Ce/Zr)_{0.85}Y_{0.1}M_{0.05}O_{3-\delta}$

More studies are still necessary to complete quantify the exact reasons for the change in conductivity of the electrolytes after doping with transition metals. EMF measurements are utilized to determine the ionic transport number in electrolytes. Also it is possible to identify the transport number. The EMF of hydrogen concentration cell with BCYM and SCYM electrolytes as well as the original SCY and BCY in moist

atmospheres is shown in Fig. 2.8 ($P_{H2O(I)} = P_{H2O(II)} = 0.019$, $P_{H2(I)} = 0.01–0.98$ and $P_{H2(II)} = 0.01$). The theoretical EMF is calculated using the following Nernst's equation;

$$E_{\text{theo}} = -(t_{H^+} + t_{O^{2-}})\frac{RT}{2F}\ln\frac{P_{H_2}(II)}{P_{H_2}(I)} + t_{O^{2-}}\frac{RT}{2F}\ln\frac{P_{H_2O}(II)}{P_{H_2O}(I)} \qquad (2.1)$$

where F, R and T are Faraday's constant, gas constant and absolute temperature, respectively. In case of Hydrogen gas concentration cell, water vapor activities were fixed at 1.9 kPa with both electrodes. The theoretical EMF calculated follows the next equation;

$$E_{t_{ion}} = -(t_{H^+} + t_{O^{2-}})\frac{RT}{2F}\ln\frac{P_{H_2}(II)}{P_{H_2}(I)} \qquad (2.2)$$

The solid lines in the figures are values calculated by Eq. 2.2. The ionic transport number is given by E/E_{theo}. The measured EMFs were nearly equal to the values calculated from the Nernst's equation in BCYM and SCYM. This result reveals that the introduction of transition metals dose not introduce electronic conductivity to the oxides in reducing atmosphere. Moreover, the measurement of water vapor concentration cell result is shown in Fig. 2.9. The hydrogen activities of the both electrode were equal ($P_{H2O(I)} = 0.006 – 0.019$, $P_{H2O(II)} = 0.019$ and $P_{H2(I)} = P_{H2(II)} = 0.01$). Therefore, the first term of equation (2.1) can be ignored. The theoretical EMF calculated follows the next equation;

$$E_{t_H} = t_{O^{2-}}\frac{RT}{2F}\ln\frac{P_{H_2O}(II)}{P_{H_2O}(I)} \qquad (2.3)$$

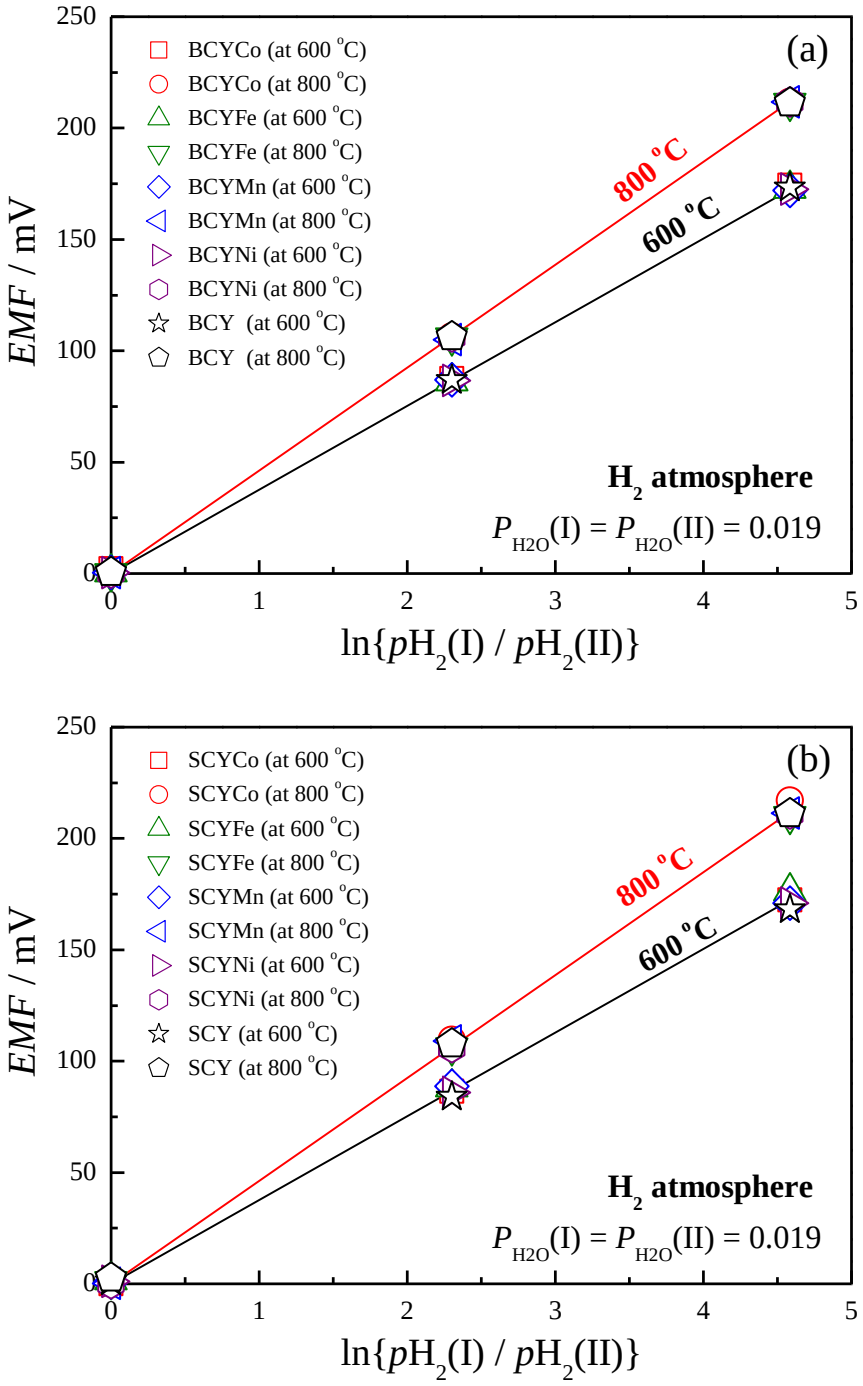

Fig. 2.8 The EMF of hydrogen concentration cell using transition metal-doped (a) BCYM and (b) SCYM electrolytes (solid line is the theoretical value of EMF)

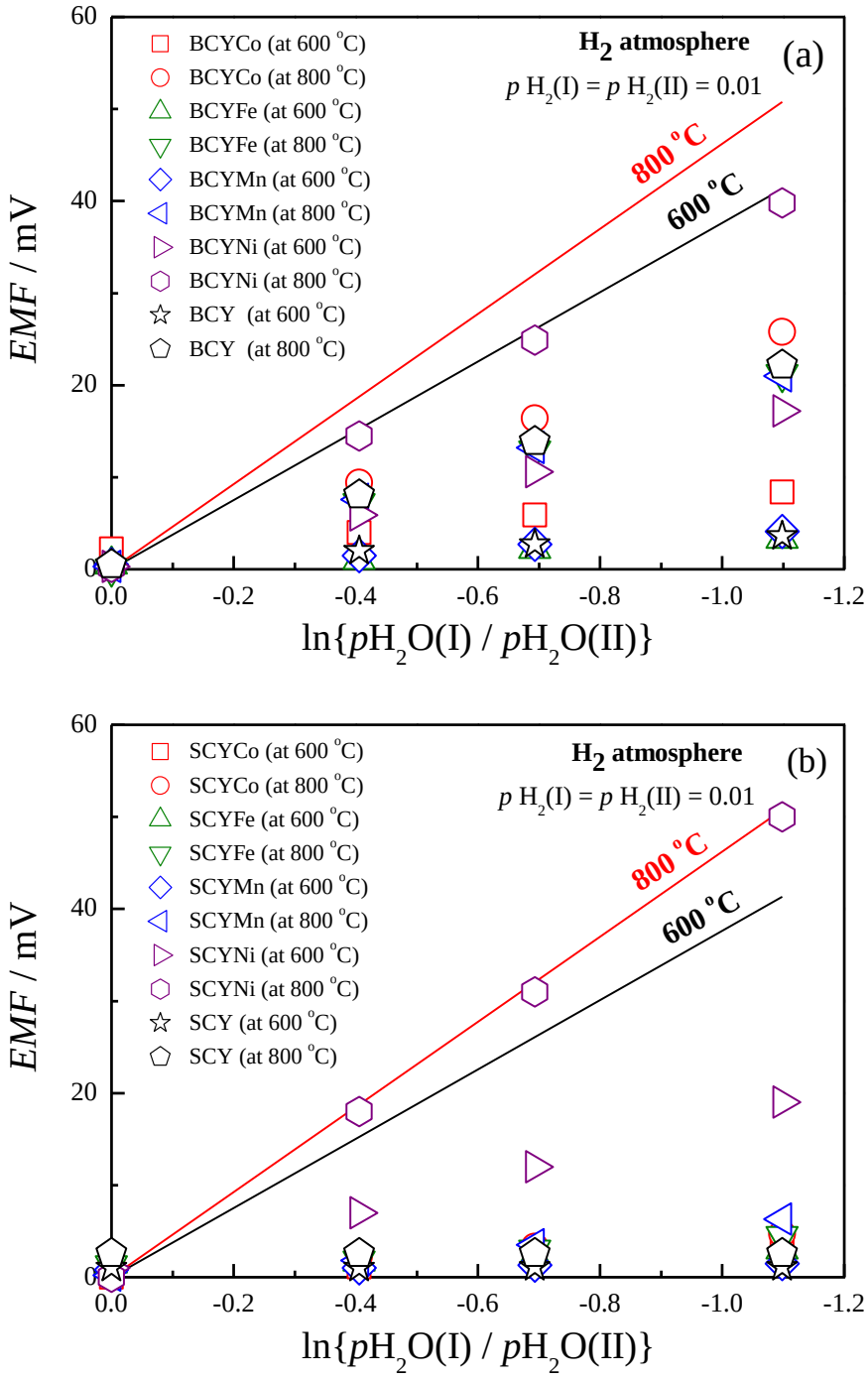

Fig. 2.9 The EMF of water vapor concentration cell using transition metal-doped (a) BCYM and (b) SCYM electrolytes in H_2 atmosphere.

(solid line is the theoretical value of EMF)

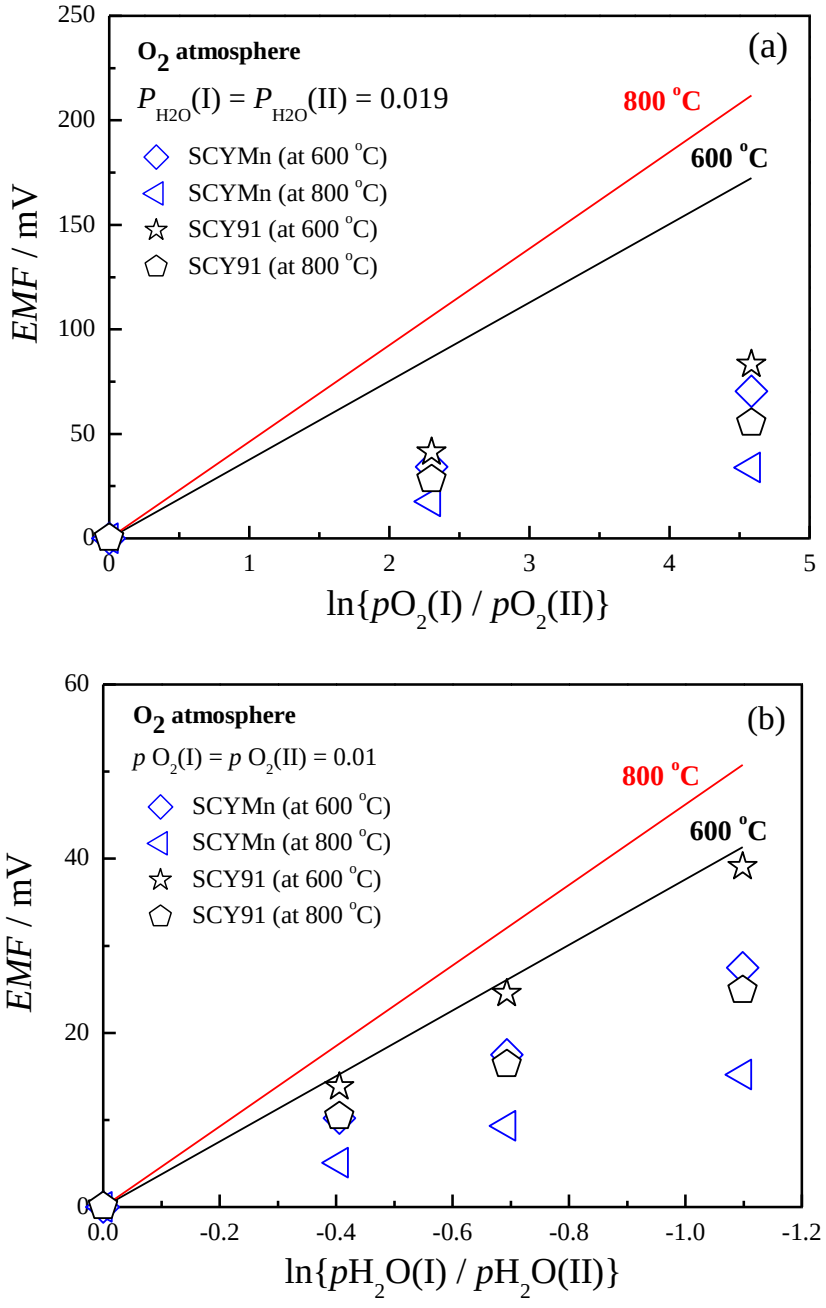

Fig. 2.10 The (a) EMF of oxygen gas concentration cell ($P_{H2O(I)} = P_{H2O(II)} = 0.019$ and $P_{O2(I)} = 0.01 – 0.98$, $P_{O2(II)} = 0.01$) and (b) water vapor concentration cell ($P_{H2O(I)} = 0.006 – 0.019$, $P_{H2O(II)} = 0.019$ and $P_{O2(I)} = P_{O2(II)} = 0.01$) using SCY and SCYMn electrolytes in O_2 atmosphere at 600 and 800 °C

(solid line is the theoretical value of EMF)

Also, If the transport number is in oxide unity, the EMF can be represented with the theoretical case. The EMFs of BCY, BCYCo, BCYFe and BCYMn were slightly increased at 600 ^{o}C signifying an increase in the oxide transport number. The proton transport number were 0.93, 0.85, 0.93 and 0.91, respectively. In addition, proton transport number has half value at 800 ^{o}C (BCY = 0.57, BCYCo = 0.49, BCYFe = 0.58, BCYMn = 0.59). On the other hand, proton transport number of BCYNi were significantly decreases than other electrolytes at 600 ^{o}C and 800 ^{o}C (t_H = 0.58 and 0.22). This is also consistent with SCYM system. SCY, SCYCo, SCYFe and SCYMn electrolytes have very limited oxide ion conduction thus the proton transport number in hydrogen atmosphere is almost unity at 600 ^{o}C and 800 ^{o}C. However, the EMF of SCYNi was nearly equal to the theoretical value calculated at 800 ^{o}C. This implies that the major charge carriers are oxide ion ($\underline{t}_H$ = 0.02). In addition, proton transport number has half value at 600 ^{o}C (t_H = 0.56).

SCYMn shows most high the electrical conductivity in air atmosphere with SCYM system. Therefore, SCY and SCYMn electrolytes were selected to confirm the transport number. The EMF of oxygen concentration cell is represented by the following equation:

$$E_{\text{theo}} = (t_{H^+} + t_{O^{2-}})\frac{RT}{4F}\ln\frac{P_{O_2}(II)}{P_{O_2}(I)} - t_{H^+}\frac{RT}{2F}\ln\frac{P_{H_2O}(II)}{P_{H_2O}(I)}$$

Figure 2.10 shows the EMF of gas concentration cell ($P_{\text{H2O(I)}}$ = $P_{\text{H2O(II)}}$ = 0.019, $P_{\text{O2(I)}}$ = 0.01 – 0.98 and $P_{\text{O2(II)}}$ = 0.01) and water vapor concentration cell ($P_{\text{H2O(I)}}$ = 0.006 – 0.019, $P_{\text{H2O(II)}}$ = 0.019 and $P_{\text{O2(I)}}$ = $P_{\text{O2(II)}}$ = 0.01) using SCY and SCYMn in O_2

atmosphere. The measured EMFs were overall decrease to the values calculated from the Nernst's equation. It is notable that the ionic transport number of SCYMn, which are 0.42 and 0.16, are markedly smaller than that of SCY, 0.48 and 0.26 at 600 and 800 ^{o}C, respectively. This phenomenon also confirmed for water vapor concentration results. The proton transport number of SCY and SCYMn were 0.46 and 0.28 at 600 ^{o}C, respectively. Figure 2.11 shows the partial conductivity and proton transport number of BCYM and SCYM at 600 ^{o}C in H_2 atmosphere. As aforementioned results, proton transport number slightly decrease tendency from BCYM except BCYNi at 600 ^{o}C (Fig. 2.11(a)). Also, this results accords with the electrical conductivity and FT-IR at 600 ^{o}C in hydrogen atmosphere. SCYM case shows a more certainly change of partial conductivity (Fig. 2.11(b)). Superficially, the total conductivity in both SCY and SCYM cases are almost similar however, the EMFs data reveals significant changes in the conduction species within the materials. Figure 2.12 shows the partial conductivity and proton transport number of BCYM and SCYM at 800 ^{o}C in H_2 atmosphere. According to the results of partial conductivity, BCYM electrolytes possess tendency of proton conductivity similar with total conductivity. BCYNi has the most poor proton conductivity among others. Thus, the overpotentials of fuel cell mode can hydrolyses that the increase tendency follow as Ni > Fe > Co > Mn in hydrogen-side electrodes at 800 ^{o}C. Meanwhile, SCYM system shows very similar proton conductivity except for SCYNi at 800 ^{o}C. The total conductivity doesn't change, but proton transport number into it decreases. Thus, an increase in oxide transport number helped to offset the change in total conductivity. The proton transport number in BCYNi and SCYNi made the biggest drop in all system.

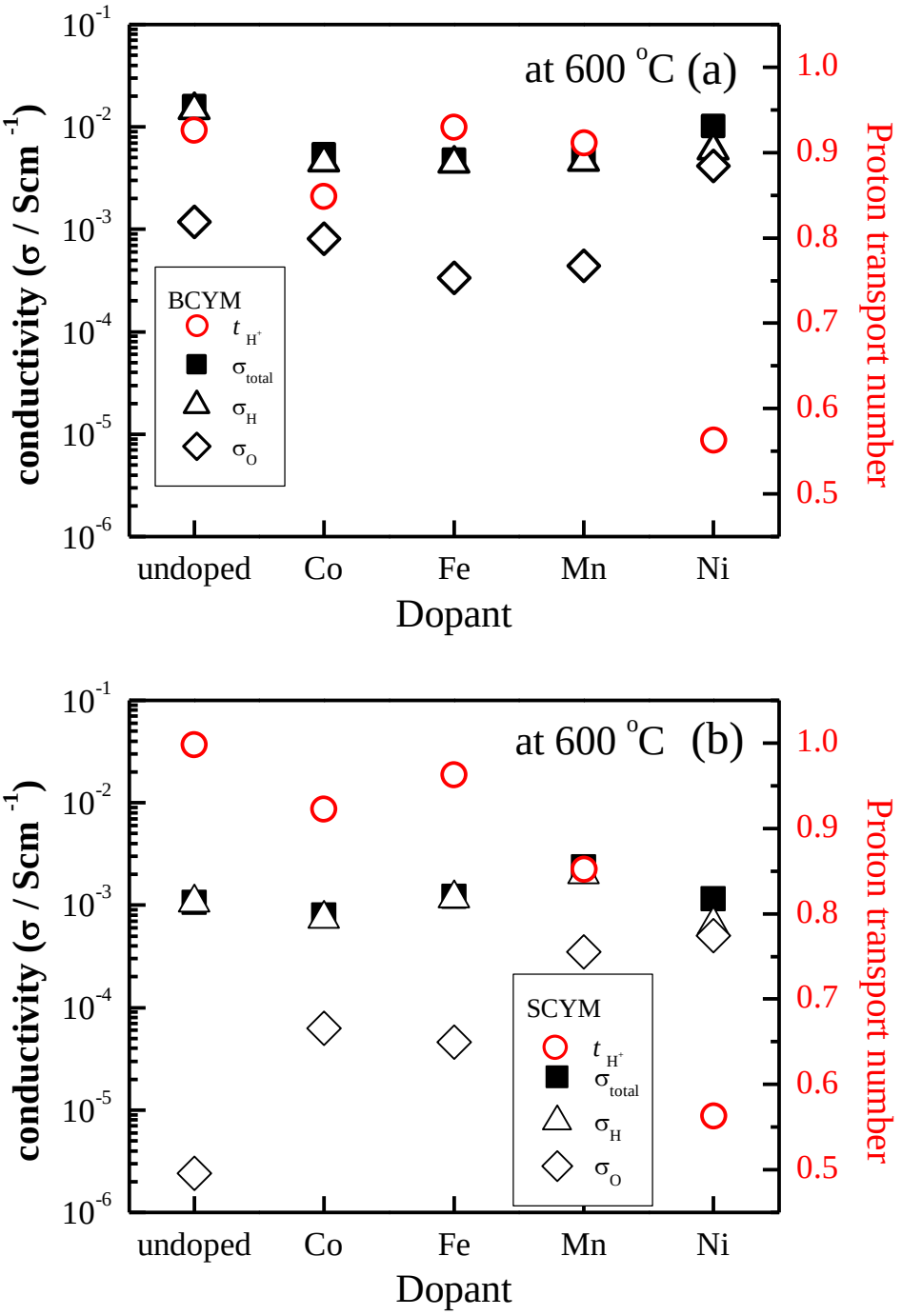

Fig. 2.11 The partial conductivity and proton transport number of transition metal-doped (a) BCYM and (b) SCYM electrolytes at 600 °C in H_2 atmosphere.

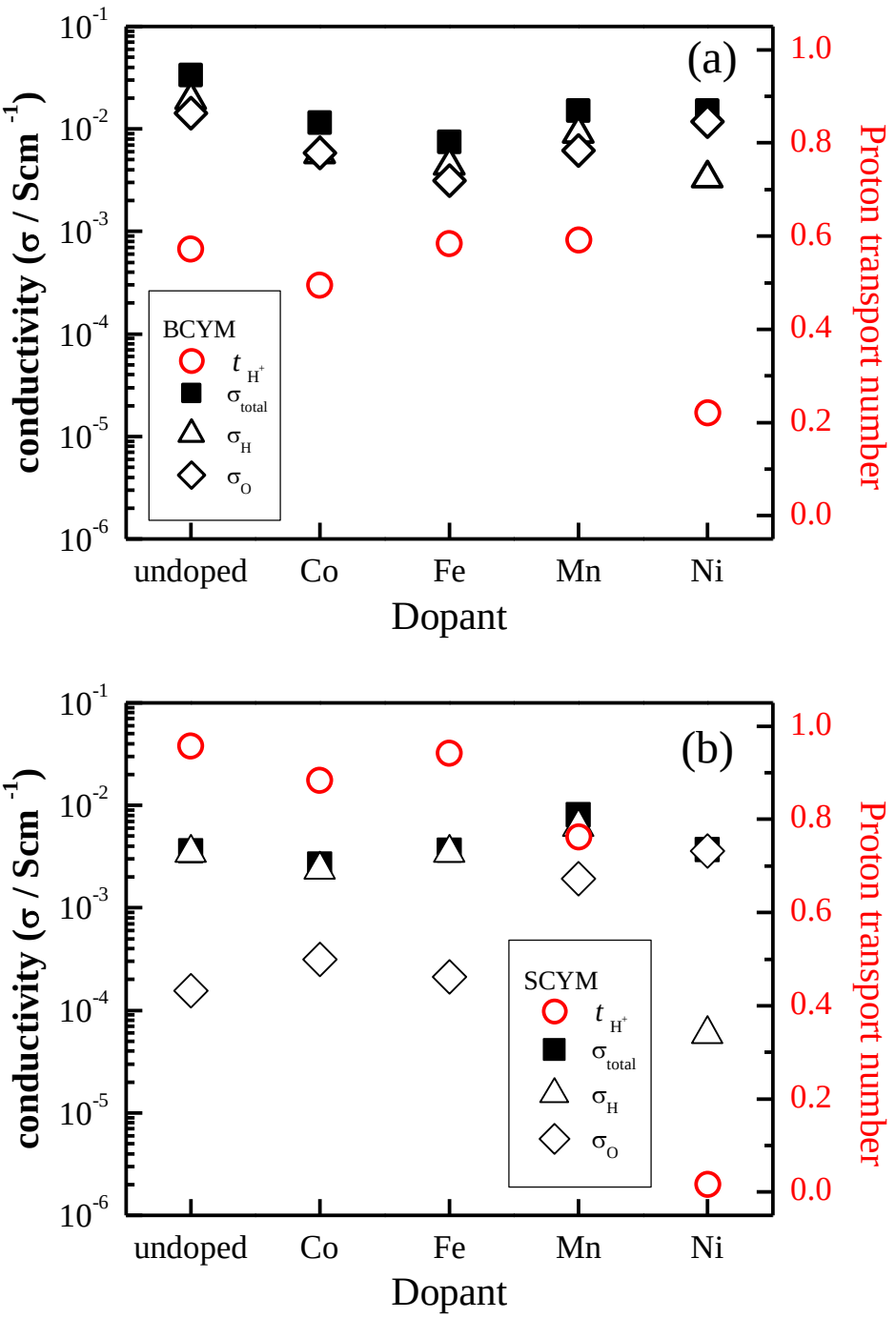

Fig. 2.12 The partial conductivity and proton transport number of transition metal-doped (a) BCYM and (b) SCYM electrolytes at 800 ^{o}C in H_2 atmosphere.

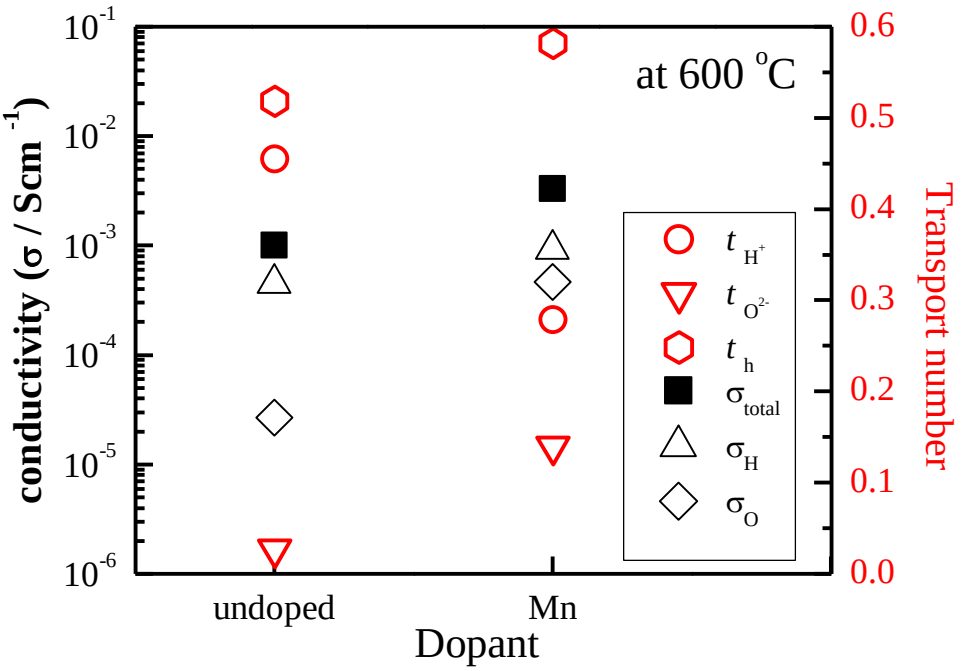

Fig. 2.13 The partial conductivity and transport number of SCY and SCYMn electrolytes at 600 °C in O_2 atmosphere.

Figure 2.13 shows the partial conductivity and transport number of SCY and SCYMn in O_2 atmosphere at 600 °C. The total conductivity in SCYMn was higher than that of SCY at 600 °C, and the conduction species within the materials are significant changed. The SCYMn was increased at 600 °C confirm an increase in the electronic transport number. Therefore, formation of conductivity of SCYMn can be confirmed as a decrease in proton transport number but increase in oxygen and electronic transport number as compared with SCY. These results can explain that SCYMn has a low proton concentration in FT-IR results (Fig. 2.6(c)). However, proton conductivity was slightly increased than that of SCY. The reason for proton conductivity increased in the Mn doping on the SCY is still unclear. However, these results suggest that the transition

metal doping cause increase or decrease in the conductivity and transport number of the electrolytes from that of the original proton conductor and that the magnitude of the properties change depends on the transition metals and parent proton conductors.

2.4 Conclusion

The electrical properties of transition metal doped $BaCe_{0.85}Y_{0.1}M_{0.05}O_{3-\delta}$, $BaZr_{0.85}Y_{0.1}M_{0.05}O_{3-\delta}$, $SrCe_{0.85}Y_{0.1}M_{0.05}O_{3-\delta}$ and $SrZr_{0.85}Y_{0.1}M_{0.05}O_{3-\delta}$ (M = Co, Fe, Mn and Ni) have been investigated. The total conductivity of transition metals doped $SrCe_{0.85}Y_{0.1}M_{0.05}O_{3-\delta}$ slightly increased or nearby equal than that of $SrCe_{0.9}Y_{0.1}O_{3-\delta}$. Meanwhile, $BaCe_{0.85}Y_{0.1}M_{0.05}O_{3-\delta}$, $BaZr_{0.85}Y_{0.1}M_{0.05}O_{3-\delta}$ and $SrZr_{0.85}Y_{0.1}M_{0.05}O_{3-\delta}$ were decreased than that of original electrolytes. From the FT-IR results, it was found that the decrease of the proton concentration was the cause of the decreased total conductivity, but it was not consistent with all the samples. The correlation between the conductivity and the proton concentration were confirmed by the measurement of electromotive force. Especially, it found that the proton transport number decreased significantly and the oxygen transport number increased in hydrogen atmosphere as $SrCe_{0.85}Y_{0.1}Ni_{0.05}O_{3-\delta}$ and $BaCe_{0.85}Y_{0.1}Ni_{0.05}O_{3-\delta}$ samples. Also, $SrCe_{0.85}Y_{0.1}Mn_{0.05}O_{3-\delta}$ represented that the proton transport number decreased and increase of electronic transport number in oxygen atmosphere. Thus, the introduction of a transition metal causes a decrease in proton concentration and transport number, leads to a decrease or increase in conductivity. Also, the changes depend on the choice of A and B–site as well as on the

various atmospheres. Information on transition metal doped electrolytes can assist in selecting suitable oxide electrode materials.

2.5 Reference

[1] H. Iwahara, H. Uchida, K. Ono, K. Ogaki, *J. Electrochem. Soc.*, 135 (1988) 529–533

[2] T. Yajima, H. Kazeoka, T. Yogo, H. Iwahara, *Solid State Ionics*, 47 (1991) 271–275.

[3] H. Iwahara, *Solid State Ionics*, 86–88 (1996) 9-15.

[4] N. Ito, M. Iijima, K. Kimura, S. Iguchi, *Journal of Power Sources*, 152 (2005) 200–203

[5] J. S. Fish, S. Ricote, R. O'Hayre, N. Bonanos, *J. Mater. Chem. A*, 3 (2015) 5392–5401

[6] H. Matsumoto, M. Okubo, S. Hamajima, K. Katahira, H. Iwahara, *Solid State Ionics*, 152–154 (2002) 715–720

[7] M. Sahibzada, S.J. Benson, R.A. Rudkin, J.A. Kilner, *Solid State Ionics*, 285 (1998) 113–115

[8] M. Sahibzada, B.C.H. Steele, K. Zheng, R.A. Rudkin, I.S. Metcalfe, *Catal. Today*, 38 (1997) 459–466

[9] D. Mantzavinos, A. Hartley, I. S. Metcalfe, M. Sahibzada *Solid State Ionics*, 134 (2000) 103–109

[10] T. Hibino, S. Wang, S. Kakimoto, M. Sano, *Solid State Ionics*, 127 (2000) 89–98

[11] B. Morel, R. Roberge, S. Savoie, T.W. Napporn, M. Meunier, *Applied Catalysis A: General*, 323 (2007) 181–187

[12] J. M. Bassat, F. Gervais, R Odier, *Mater. Science and Engineering, B3* (1989) 507–514

[13] S. Takahashi, S. Nishimoto, M. Matsuda, M. Miyake, *J. Am. Ceram. Soc.*, 93 (2010) 2329–2333

[14] P. Ranran, W. Yan, Y. Lizhai, M. Zongqiang, *Solid State Ionics*, 177 (2006) 389–393

[15] Y. Lin, R. Ran, Y. Zheng, Z. Shao, W. Jin, N. Xu, J. Ahn, *J. Power. Sources*, 170 (2007) 38–41

[16] Y. Guo, R. Ran, Z. Shao, *Int. J. Hydrogen Energy*, 36 (2011) 1683–1691

[17] C. Zhang, Z. Du, H. Zhao, X. Zhang, *Electrochimica Acta*, 108 (2013) 369–375

[18] S.Y. Jeon, D.K. Lim, I.H. Kim, B. Singh, S.J. Song, *J. Electrochem. Soc.* 161 (2014) F754–F760

[19] H. Matsumoto, I. Nomura, S. Okada, T. Ishihara, *Solid State Ionics*, 180 (2008) 15–22

[20] L. Yang, C. Zuo, S. Wang, Z. Cheng, M. Liu, *adv. Mater.* 20 (2008) 3280–3283

[21] W. Sun, L. Yan, B. Lin, S. Zhang, W. Liu, *J. Power. Sources*, 195 (2010) 3155–3158

[22] T. Wu, R. Peng, C. Xia, *Solid State Ionics*, 179 (2008) 1505–1508

[23] M. Zunic, L. Chevallier, F. Deganello, A. D'Epifanio, *J. Power. Sources*, 190 (2009) 417–422

[24] L. Yang, Z. Liu, S. Wang, Y.M. Choi, C. Zuo, M. Liu, *J. Power. Sources*, 195 (2010) 471–474

[25] T. Shimura, H. Tanaka, H. Matsumoto, T. Yogo, *Solid State Ionics*, 176 (2005) 2945–2950

[26] C. Zuo, S. Zha, M. Liu, M. Hatano, M. Uchiyama, *Adv. Mater*, 18 (2006) 3318–3320

[27] S. Ricote, N. Bonanos, A. Manerbino, W.G. Coors, *Int. J. Hydrogen Energy*, 37 (2012) 7954–7961

[28] L. Yang, S. Wang, K. Blinn, M. Liu, Z. Liu, Z. Cheng, M. Liu, *Science*, 326 (2009) 126–129

[29] H. Matsumoto, T. Sakai, Y. Okuyama, *Pure Appl. Chem.*, 85 (2013) 427–435

[30] Y. Yamazaki, R. Hernandez-Sanchez, S. H. Haile, *Chem. Mater.* 21 (2009) 2755–2762

[31] R.D. Shannon, *Acta Cryst.*, A32 (1976) 751–767

[32] K.D. Kreuer, A. Fuchs, J. Maier, *Solid State Ionics*, 77 (1995) 157–162

[33] K.D. Kreuer, *Chem. Mater.*, 8 (1996) 610–641

[34] K.D. Kreuer, *Annu. Rev. Mater. Res.*, 33 (2003) 333–359

[35] H. Matsumoto, Y. Kawasaki, N. Ito, M. Enoki and T. Ishihara, *Electrochem. Solid-State Lett.*, 10 (2007) B77–B80

[36] R. B. Cervera, Y. Oyama, S. Miyoshi, K. Kobayashi, T. Yagi, S. Yamaguchi *Solid State Ionics*, 179 (2008) 236–242

[37] T. Omata, M. Takagi, S. Otsuka, *Solid State Ionics*, 168 (2004) 99 –109

[38] S. Shin, H. H. Huang, M. Ishigame, H. Iwahara, *Solid State Ionics*, 40/41 (1990) 910 –913

[39] T. Omata, Y. Noguchi, S. O.-Y-. Matsuo, *Solid State Ionics*, 176 (2005) 2941–2944

Chapter 3

Effects of transition metal oxides doped electrolytes on the performance of PCFC

3.1 Introduction

Proton conducting materials have been studied for a number of electrochemical cell applications including protonic ceramic fuel cells (PCFC), steam electrolyzers, hydrogen pump and gas sensor as they have high electrical conductivity at intermediate temperatures [1-5]. However, performance of electrochemical cell with proton conducting material should be improved. To achieve high performance, PCFC requires new materials, which composites or design with both an improved proton conductivity of the electrolyte. Furthermore, electrolyte materials should have a fully dense structure as well as high ionic conductivity and low electronic conductivity to appear cell performance. For example, barium zirconate based proton conducting materials show high electrical conductivity. On the other hand, these materials require high sintering temperature to obtain high density [6-8]. Given this reason, recent researchers have attempted to optimize the sinterability and reduce the sintering temperature by doping the transition metals [9-13]. Ricote et al. reported that Co and Ni doped barium zirconate and barium cerate electrolyte demonstrated the effects of transition metal composite oxide on the electrolytes grain growth and sinterability [13]. The sintering temperature has been decreased from 1700 °C to 1450 °C by using cobalt or nickel as

sintering aid with a content of 1 or 2% of the B site. However, the ionic contribution of the conductivity decreased to an order of magnitude when Co or Ni were employed as sintering aid for $BaZr_{0.9}Y_{0.1}O_{3-\delta}$. These results show that the advantages accompanied with disadvantages of introduction transition metal on the electrolytes. Meanwhile, many studies have reported oxide containing transition metal composition cathode material in PCFC, such as $La_{0.7}Sr_{0.3}FeO_{3-\delta}$–$BaZr_{0.1}Ce_{0.7}Y_{0.2}O_{3-\delta}$ [14], $La_{0.8}Sr_{0.2}MnO_{3-\delta}$–$BaCe_{0.85}Y_{0.15}O_{3-\delta}$ [15], $Ba_{0.5}Sr_{0.5}Co_{0.8}Fe_{0.2}O_{3-\delta}$ [16-20], $Sm_{0.5}Sr_{0.5}CoO_{3-\delta}$ [21-24], $La_{0.6}Sr_{0.4}Co_{0.2}Fe_{0.8}O_{3-\delta}$ [25-26], $Ba_{0.5}Sr_{0.5}FeO_{3-\delta}$ [27], have been employed as cathode in PCFCs. Table 1 is a summary of the advances in the PCFC performance based on barium cerates electrolyte in other research [14-21,25,28-34]. Researchers investigated oxide materials containing Co and/or Fe from cathode materials. Power density of >1.0 Wcm^{-2} at intermediate temperatures of 600–800 ^{o}C is frequently reported in literature. Matsumoto et al. reported that a solid oxide fuel cell with $BaCe_{0.9}Y_{0.1}O_{3-\delta}$ electrolyte demonstrated the effects of transition metal composite oxide electrode on the cell [21]. According to the report, $Sm_{0.5}Sr_{0.5}CoO_3$ and $Ba_{0.6}La_{0.4}CoO_3$ shows higher cathode activities than $La_{0.7}Sr_{0.3}MnO_3$ (Fig. 3.1). In regard to the transition metals studied in their works, the descending power of the cathode activity is Fe > Co > Mn. From these results, the diffusion of transition metals may has negative effect on the electrode performance to decrease the conductivity of the electrolyte. Also, Nian et al. reported that a protonic ceramic fuel cell with $BaCe_{0.8}Sm_{0.2}O_{3-\delta}$ (BCS) electrolyte and with cathode material of $SmBaCuCoO_{5+\delta}$ (SBCC) or $SmBaCuFeO_{5+\delta}$ (SBCF) [34]. Based on the cathode materials studied in their works (Fig. 3.2(a)), the descending power of the

cathode activity (Co>Fe) was the same with that of the conductivity reported by Shimura et al. [35].

Table 3.1 A summary of PCFCs performance based on barium cerates electrolytes and their reported maximum power densities

Author (Year)	Electrodes (anode/cathode)	Electrolyte (thickness/μm)	Maximum Power density ($mWcm^{-2}$)	Temp. (^oC)	Ref.
N. Taniguchi (1992)	Pt/Pt	$BaCe_{0.75}Gd_{0.25}O_{3-\delta}$ (500)	230	800	[28]
H. Iwahara (1993)	Pt/Pt	$BaCe_{0.8}Sm_{0.2}O_{3-\delta}$ (500)	220	1000	[29]
T. Hibio (2002)	Pd-loaded FeO/$BaPrCoO_3$	$BaCe_{0.75}Y_{0.25}O_{3-\delta}$ (500)	134	600	[30]
N. Maffei (2004)	Pt/$La_{0.6}Fe_{0.8}Co_{0.2}O_{3-\delta}$	$BaCe_{0.8}Gd_{0.2}O_{3-\delta}$ (1000)	6	700	[31]
P. Ranran (2006)	Ni- $BaCe_{0.8}Sm_{0.2}O_{3-\delta}$ / $Ba_{0.5}Sr_{0.5}Co_{0.8}Fe_{0.2}O_{3-\delta}$	$BaCe_{0.8}Sm_{0.2}O_{3-\delta}$ (50)	340	700	[16]
Q. Ma (2006)	Ni-$BaCe_{0.8}Gd_{0.2}O_{3-\delta}$ / $La_{0.5}Sr_{0.5}CoO_3$+$BaCe_{0.8}Gd_{0.2}O_{3-\delta}$	$BaCe_{0.8}Gd_{0.2}O_{3-\delta}$ (50)	371	700	[32]
K. Xie (2007)	Ni-$BaCe_{0.9}Nd_{0.1}O_{3-\delta}$ / $La_{0.5}Sr_{0.5}CoO_3$+$BaCe_{0.9}Nd_{0.1}O_{3-\delta}$	$BaCe_{0.9}Nd_{0.1}O_{3-\delta}$ (20)	335	700	[33]
Y. Lin (2008)	Ni-$BaCe_{0.9}Y_{0.1}O_{3-\delta}$ / $Ba_{0.5}Sr_{0.5}Co_{0.8}Fe_{0.2}O_{3-\delta}$	$BaCe_{0.9}Y_{0.1}O_{3-\delta}$ (55)	550	700	[17]
H. Matsumoto (2008)	Ni-$BaCe_{0.9}Y_{0.1}O_{3-\delta}$ / $Sm_{0.5}Sr_{0.5}CoO_3$	$BaCe_{0.9}Y_{0.1}O_{3-\delta}$ (7)	295	700	[21]
M. Zunic (2009)	Ni-$BaCe_{0.9}Y_{0.1}O_{3-\delta}$ / $La_{0.8}Sr_{0.2}Co_{0.8}Fe_{0.2}O_{3-\delta}$ +$BaCe_{0.9}Yb_{0.1}O_{3-\delta}$	$BaCe_{0.9}Y_{0.1}O_{3-\delta}$ (15)	174	650	[25]
Q. Nian (2010)	Ni-$BaCe_{0.8}Sm_{0.2}O_{3-\delta}$ / $SmBaCuCoO_{5+\delta}$ or $SmBaCuFeO_{5+\delta}$	$BaCe_{0.8}Sm_{0.2}O_{3-\delta}$ (13)	449 333	700	[34]

Y. Guo (2011)	Ni-$BaZr_{0.4}Ce_{0.4}Y_{0.2}O_{3-\delta}$ / $Ba_{0.5}Sr_{0.5}Co_{0.8}Fe_{0.2}O_{3-\delta}$	$BaCe_{0.8}Y_{0.2}O_{3-\delta}$ (35)	566	700	[18]
C. Zhang (2013)	Pt / Co_3o_4+$Ba_{0.5}Sr_{0.5}Co_{0.8}Fe_{0.2}O_{3-\delta}$	$BaCe_{0.8}Sm_{0.2}O_{3-\delta}$ (500)	110	750	[19]
K.C. Lee (2013)	Ni-$BaCe_{0.85}Y_{0.15}O_{3-\delta}$ / $La_{0.8}Sr_{0.2}MnO_3$+$BaCe_{0.85}Y_{0.15}O_{3-\delta}$	$BaCe_{0.85}Y_{0.15}O_{3-\delta}$ (16)	407	750	[15]
S.Y. Jeon (2014)	Ni-$BaCe_{0.85}Y_{0.15}O_{3-\delta}$ / $Ba_{0.5}Sr_{0.5}Co_{0.8}Fe_{0.2}O_{3-\delta}$	$BaCe_{0.85}Y_{0.15}O_{3-\delta}$ (10)	1040	750	[20]

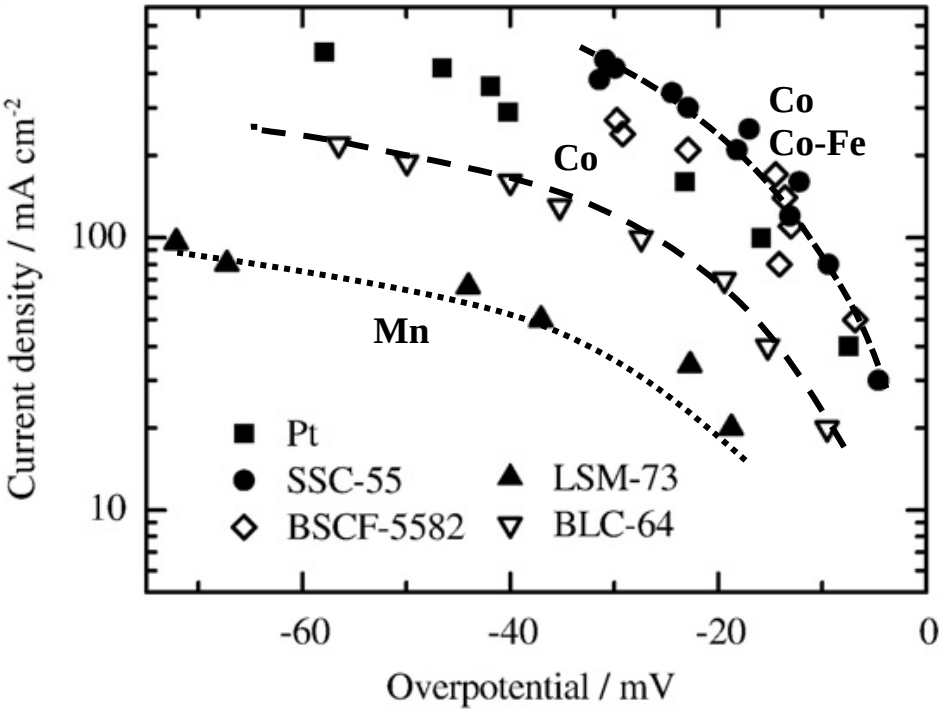

Fig. 3.1 Comparison of cathodic overpotentials of porous platinum, $Sm_{0.5}Sr_{0.5}CoO_3$, $Ba_{0.5}Sr_{0.5}Co_{0.8}Fe_{0.2}O_{3-\delta}$, $La_{0.7}Sr_{0.3}MnO_3$ and $Ba_{0.6}La_{0.4}CoO_3$ measured for H_2 and O_2 fuel cells using $BaCe_{0.9}Y_{0.1}O_{3-\delta}$ electrolyte at 800 ^oC [21]

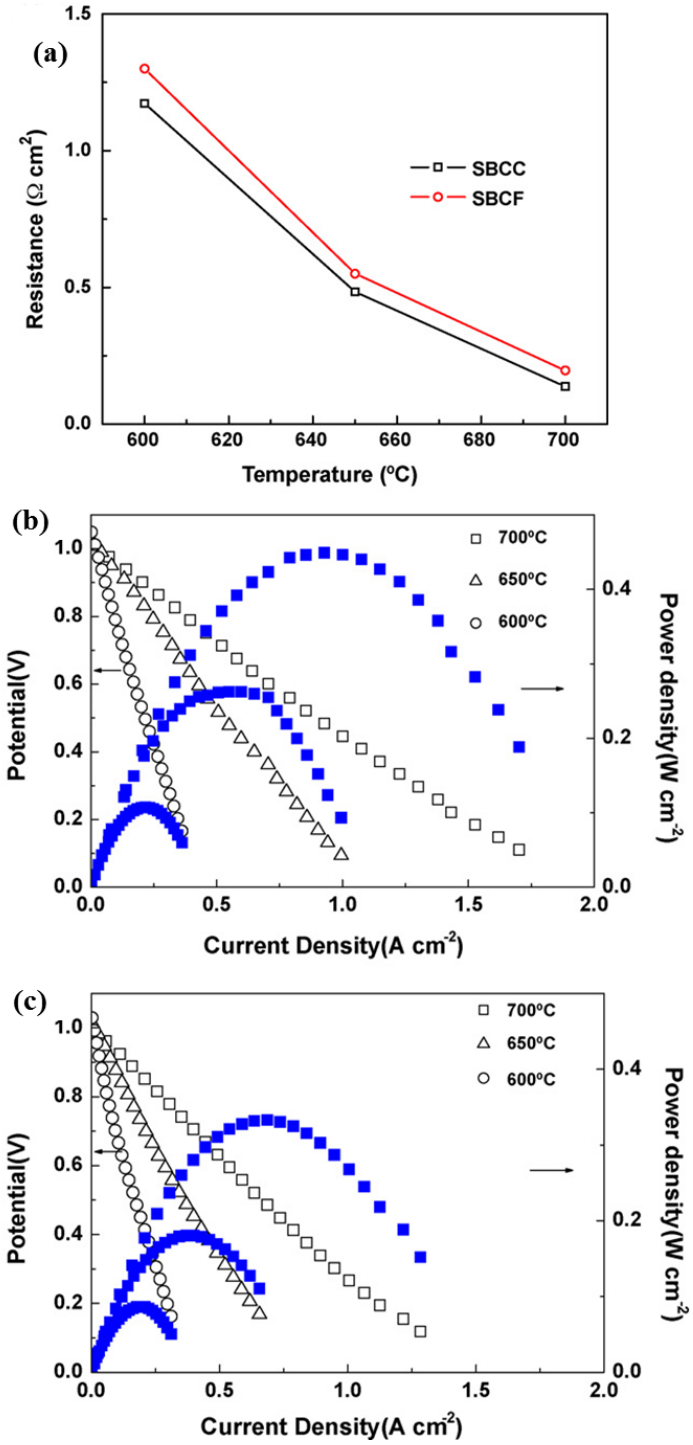

Fig. 3.2 (a) Interfacial polarization resistance comparison between SBCC and SBCF, cell performance of (b) SBCC/BCS/NiO–BCS cell and (b) SBCF/BCS/NiO–BCS cell in H_2 and air atmosphere at 600–700 ^oC [34]

Also, the power density of cell with SBCC cathode was higher than that of SBCF cathode. It is indicated that the electrocatalytic activity for the oxygen reduction of SBCC is higher than that of SBCF from result of I-V and I-P curves (Fig. 3.2). According to this relationship, e the electrode performance degraded since the diffusion of transition metals resulted in the decrease of electrolyte conductivity. Thus, transition metals did not only increase the electrolyte resistance, but also can decrease the electrode activity of the cell. From these viewpoints, it is imperative to understand to what extend the introduction of transition metals can affect the proton conductivity of electrolytes.

Chapter 2 established the electrical properties to investigate such effect of transition metal doping on the electrolytes. It is necessary to confirm whether the decrease in the conductivity of the electrolyte due to the introduction of the transition metal causes an increase in the electrode overpotential in the fuel cell. In this chapter, the electrode activity the doped and parent electrolytes were evaluated through testing PCFC performance. Fuel cell performance is an important process to evaluate electrode compatibility in proton conducting electrolytes. Therefore, Pt was used for both anode and cathode electrodes to confirm the effect of the transition metal. Figure 3.3 shows a schematic illustration of the PCFC using transition metals doped BCYM electrolytes. The reaction of PCFC at the anode (3.1) released electrons and produces proton ions. The electrons flow via an external circuit to the cathode and react with oxygen and protons flowing through to produce water (3.2).

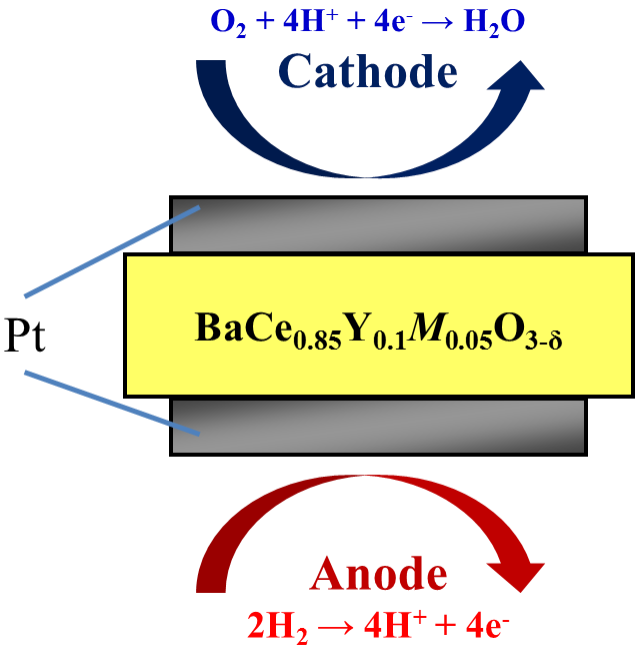

Fig. 3.3 Schematic illustrations of PCFC using transition metals doped BCYM electrolytes

The anode and cathode reactions for the fuel cell represented in figure 3.2 are as follows;

$$\text{Anode: } 2H_2 \rightarrow 4H^+ + 4e^- \qquad (3.1)$$

$$\text{Cathode: } O_2 + 4H^+ 4e^- \rightarrow 2H_2O \qquad (3.2)$$

$$\text{Overall: } 2H_2 + O_2 \rightarrow 2H_2O \qquad (3.3)$$

The cells were prepared with 5% transition metal doping on the $BaCe_{0.85}Y_{0.1}O_{3-\delta}$ (BCY) and $BaCe_{0.85}Y_{0.1}M_{0.05}O_{3-\delta}$ (M = Co, Fe and Mn) electrolytes to clarify the role of transition metals contributions to the cell performance. $BaCe_{0.85}Y_{0.1}M_{0.05}O_{3-\delta}$ which are

referred to hereafter as BCYM, transition-metal-specifically as BCYCo, BCYFe, and BCYMn, respectively.

3.2 Experimental

3.2.1 Preparation of BCYM electrolytes and PCFC cells

$BaCe_{0.85}Y_{0.1}M_{0.05}O_{3-\delta}$ electrolytes were prepared by solid state reaction method. $BaCO_3$ (Rare metallic, 99.99 %), CeO_2 (Rare metallic, 99.99 %), Y_2O_3 (Mitsuwa's pure chemicals, 99.99 %), Co_3O_4 (Kanto chemical, 99.95 %), Fe_2O_3 (Mitsuwa's pure chemicals, 99.99 %) and MnO_2 (High purity chemicals, 99 %) were appropriately weighed, mixed in a zirconia mortar with ethanol and calcined at 1200 °C for 10 h in air. The synthesized powders were then ball milled (P-7 classic, Fritsch Co., Ltd.) with 15 mm zirconia ball at 300 rpm for 1h in ethanol and dried in vacuum oven at 120 ^{o}C for overnight. Obtained powders were pressed into pellets at 250 MPa for 10 min and finally sintered at1400–1600 °C for 10 h in air. The as synthesized BCYM electrolytes show no secondary phases, dense (≥ 95 %) and exhibits perovskite structure (Fig. 2.3(a)). Dense and polished BCYM electrolytes (thickness = 500 μm) were painted Pt paste (Tanaka kikinzoku) on the electrolyte as an anode and a cathode with screen printing (diameter = 8 mm), then baked at 950 ^{o}C for 1h in air. Fig. 3.4 shows the schematic illustration of the apparatus for PCFC experiment. Pt mesh (80 mesh, Tanaka kikinzoku, Kogyo) was used for the electrode on each side. Pt reference electrode was set at between the anode and cathode electrode. The samples were setting on the alumina tube with Pyrex glass ring on both sides, and then melted at 950 ^{o}C for 1h to

seal the electrode compartments after the sample was assembled in the experimental apparatus.

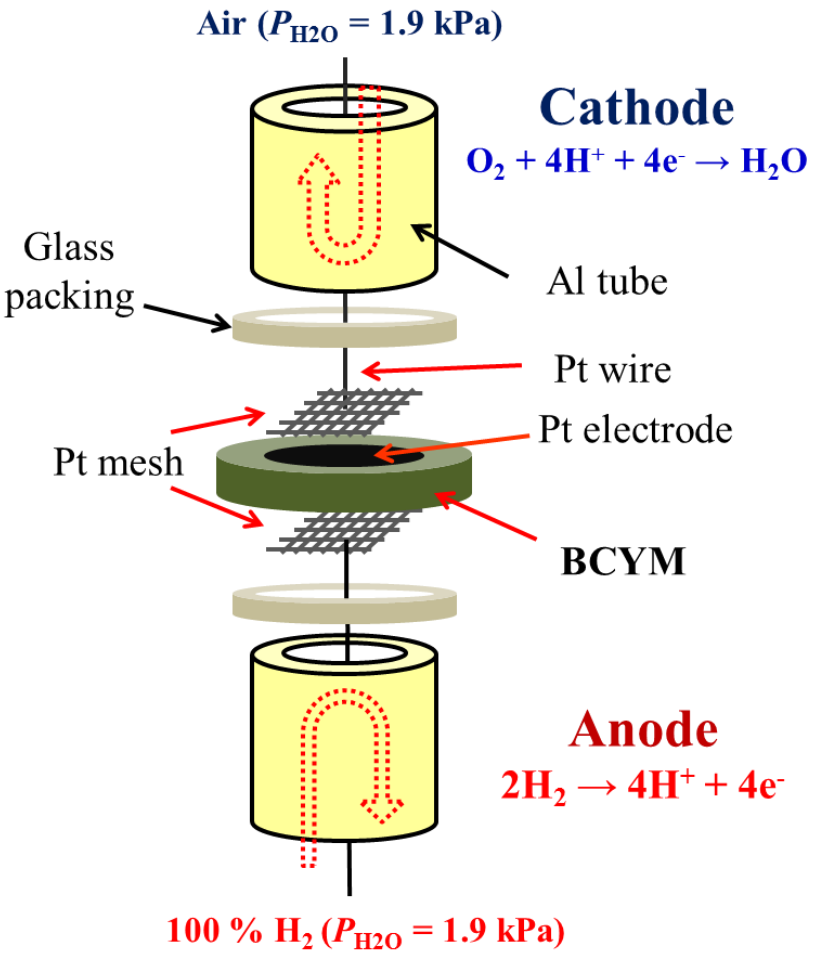

Fig. 3.4 Schematic illustration of the apparatus for PCFC experiments

3.2.2 Fuel cell performance

Fuel cell performance characteristics of the electrochemical cell were measured with the moist 100 %H_2 and air atmosphere at 800 ^oC (pH_2O = 1.9 kPa). The composition of fuel cell is as follow;

Anode – 100 % H_2, Pt │ Electrolytes (BCY or BCYM) │ Pt, air – Cathode

The electrode performance of the cell was evaluated by a current interrupt method and AC impedance method. Also, the change in potentials of the cell was monitored with an oscilloscope (Wave Surfer 422, LeCroy) when a DC was shut off. The electric potentials of the anode and cathode against the reference electrode, V_{RA} (j) and V_{RC} (j), were measured as functions of the current density, j [2]. The electric potentials of the anode and cathode against the reference electrode, V_{RA} (j) and V_{RC} (j), were measured as functions of the current density, j. The overpotentials, defined as the changes in the potentials from those under open circuit condition, consist of electrode reaction polarization, η_{RA} and η_{RC}, overpotentials due to the changes in hydrogen concentrations were ignored because of the hydrogen partial pressure constant in the measurement, ohmic losses, iR_{RA} and iR_{RC}, are shown in equation (3.4) and (3.5). (meaning of $V_{RA}(0)$ and $V_{RC}(0)$ are open circuit voltage)

$$V_{RA}(j) - V_{RA}(0) = \eta_{RA} + iR_{RA} \qquad (3.4)$$

$$V_{RC}(j) - V_{RC}(0) = -(\eta_{RC} + iR_{RC}) \qquad (3.5)$$

The resistance of anode, cathode were measurement by 3-probe impedance method (SI 1287, Solartron). Impedance were connected to the 3-electrode cell where a resistance

was measured between the anode-reference, cathode-reference and anode-cathode electrode, while a current flowed between the anode and cathode, where recorded over a frequency range of 1 MHz to 0.1 Hz with an amplitude of 10 mV.

3.3 Result and discussion

3.3.1 Resistance of anode and cathode electrodes by impedance spectroscopy

Figure 3.5 shows the Nyquist plot for the PCFCs using BCYM electrolytes in both measurement atmospheres (moist 100% H_2-air) at 800 ^oC. In plot of reference-anodes, resistance of transition metal-doped BCYM was increased than that of BCY. The increased of resistance was BCYFe > BCYCo > BCYMn > BCY (Fig. 3.5(a)). This result is consistent with the electrical conductivity of BCYM in 1% H_2 atmosphere examined in the previous chapter (Fig. 2.5(a)). It is analogize that the same result applies in other comparative cell from the electrical conductivity cell and PCFC mode. The same phenomenon for resistance result has been confirmed by reference-cathode (RA) side electrodes shown in Fig. 3.5(b). The magnitude of increase is largest with BCYMn more than other cells. According to the result of the electrical conductivity in air atmosphere (Fig. 2.4(a)), BCYMn showing a more than one order of magnitude decrease in same atmosphere. The other samples were slightly increased the resistance more than that of BCY. The increased of resistance are represent in the same order as well as; BCYMn > BCYCo > BCYFe > BCY. These results are closely consistent in variation as well as in order with PCFC mode and 4-probe cells. Figure 3.5(c) shows the resistance of anode-cathode (AC) electrodes.

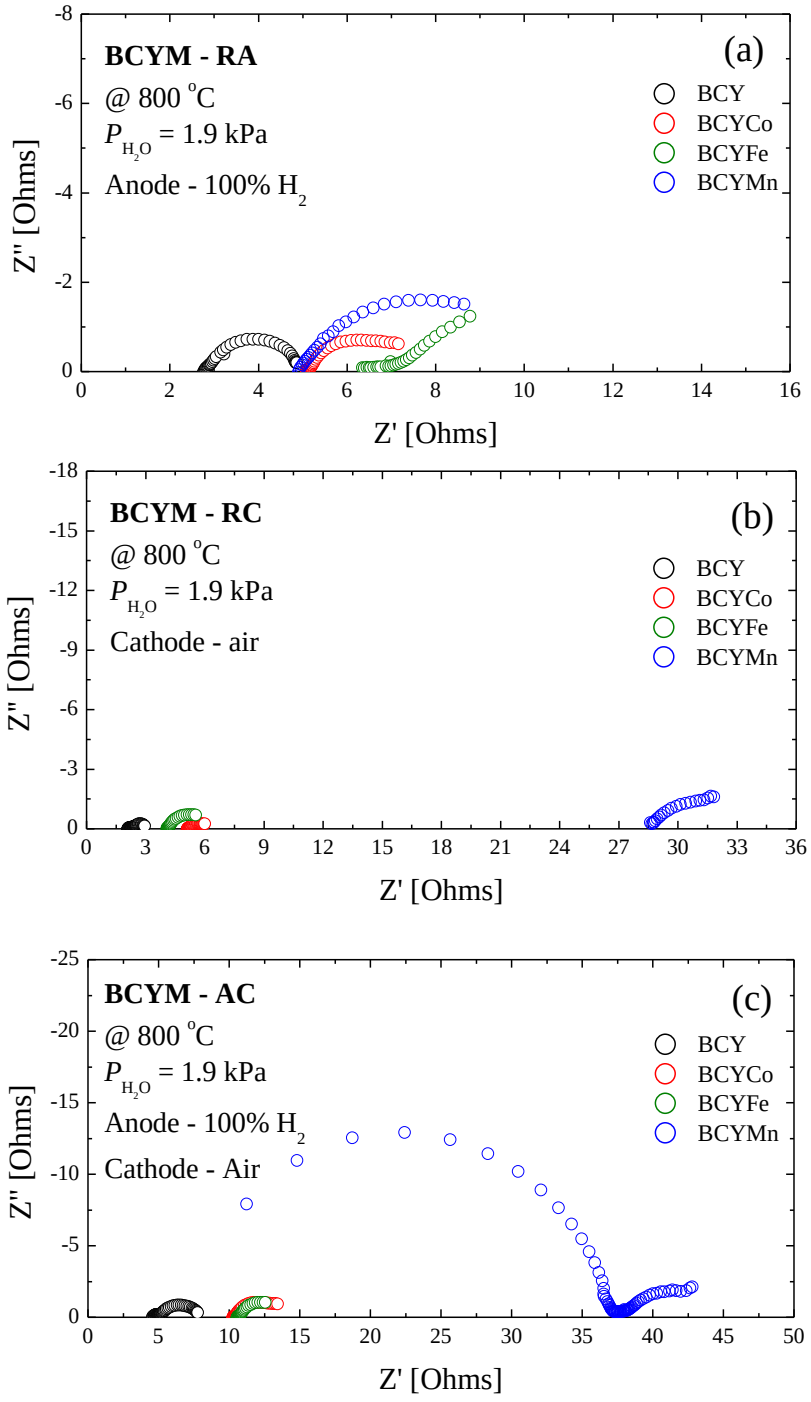

Fig. 3.5 Nyquist plot of (a) reference-anode, (b) reference-cathode and (c) anode-cathode electrodes resistance using BCYM electrolytes for PCFCs at 800 °C in moist air/100% H_2 atmosphere (pH_2O = 1.9 kPa)

The AC resistance coincide with adding up of anode and cathode value, where increases with the order Mn > Fe = Co.

3.3.2 Electrode overportential of transition metals doped BCY electrolytes and PCFC performance

The electrodes overpotentials and ohmic resistances of the PCFCs with BCYM electrolytes with Pt electrode of both sides at 800 ^{o}C in moist air-H_2 atmospheres are shown in Fig. 3.6. BCYM electrolytes containing transition metals can be confirmed that the cathodic and anodic overpotentials increased than BCY electrolyte by the current interrupt method. The anodic overpotential of BCYFe increased significantly than other materials. BCYFe also shows lower the electrical conductivity (Fig. 2.5(a)), reference-anode resistance (Fig. 3.5(a)) and proton conductivity (Fig. 2.11(a)) in hydrogen atmosphere. Thus, this higher overpotential can be caused by reduction of electrical properties. Also, the anodic overpotentials of BCYCo and BCYMn correspond to results of proton conductivity. In Fig. 3.5 (b), BCYMn sample shows the largest value of cathodic overpotential. On the other hand, BCYCo electrolyte has the smallest value of cathodic overpotential. (Mn > Fe > Co). This variation is similar with the electrical conductivity and reference-cathode resistance. The ohmic losses of the BCYM containing transition metals cell were significantly higher than that of the BCY cell. It is confirmed that the BCYCo/BCYFe to the cathode or Co/Fe doped electrolytes are effective for decreasing the cathode overpotential. Therefore, BCYCo and BCYFe would be better than the BCYMn in fuel cell performance.

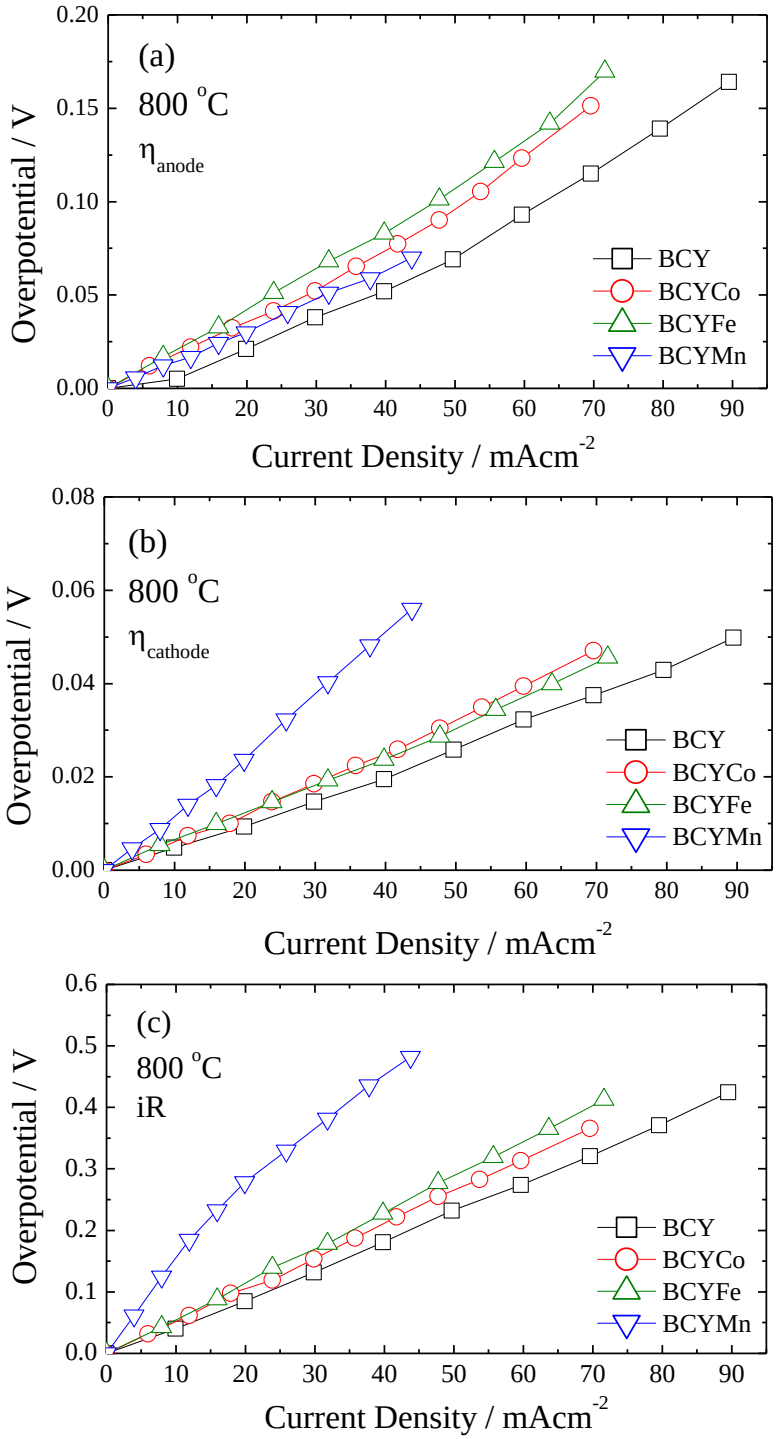

Fig. 3.6 Comparison of (a) anodic overpotentials, (b) cathodic overpotentials and (c) ohmic losses measured for moist air/100 % H_2 atmosphere fuel cell using BCYM electrolytes (pH_2O = 1.9 kPa)

The electrodes overpotentials and ohmic losses of the PCFCs using BCYM electrolytes with Pt electrode of both sides at 800 ^{o}C in moist air-H_2 atmospheres are shown in Fig. 3.6. BCYM electrolytes containing transition metals can be confirmed that the cathodic and anodic overpotentials increased than BCY electrolyte by the current interrupt method. The anodic overpotential of BCYFe increase most than other doping electrolytes. BCYFe shows lower the electrical conductivity (Fig. 2.5(a) in Chapter 2), reference-anode resistance (Fig. 3.5(a)) and proton conductivity (Fig. 2.11(a)) in hydrogen atmosphere. Electrode overpotential increased because of reduction of the electrolyte proton conductivity. Also, the anodic overpotentials of BCYCo and BCYMn correspond to accordance with results of proton conductivity. In Fig. 3.6(b), the results also agree with Fig. 3.5(b). This variation is similar with the trends of electrical conductivity and reference-cathode resistance. The ohmic losses of the BCYM containing transition metals cell were significantly higher than that of the BCY cell. It is indicated that the BCYCo/BCYFe to the cathode or Co/Fe doped electrolytes are effective to decrease the cathode overpotential. Thus, it is suggested that BCYCo and BCYFe may be better than the BCYMn in fuel cell performance. Fig. 3.7 shows the cell voltage (I-V) and power densities (I-P) curves of BCYM electrolytes cell with Pt electrodes at 800 ^{o}C. From the result, BCY electrolyte cell shows the highest cell performance in BCYM system, the BCYCo and BCYFe sample shows almost the same values of cell voltage and power densities than BCYMn in the moist air/100 % H_2 atmosphere. The maximum power densities of the BCYCo, BCYFe and BCYMn electrolytes cell were 23 mW/cm^{-2}, 21 mW/cm^{-2} and 13 mW/cm^{-2} respectively. These values were lower than that of observed in the PCFC with BCY electrolyte (29 mW/cm^{-}

^{2}). The fuel cell performance depended on the electrodes overpotential. The results of the decreasing conductivity were caused by the introduction of the transition metal.

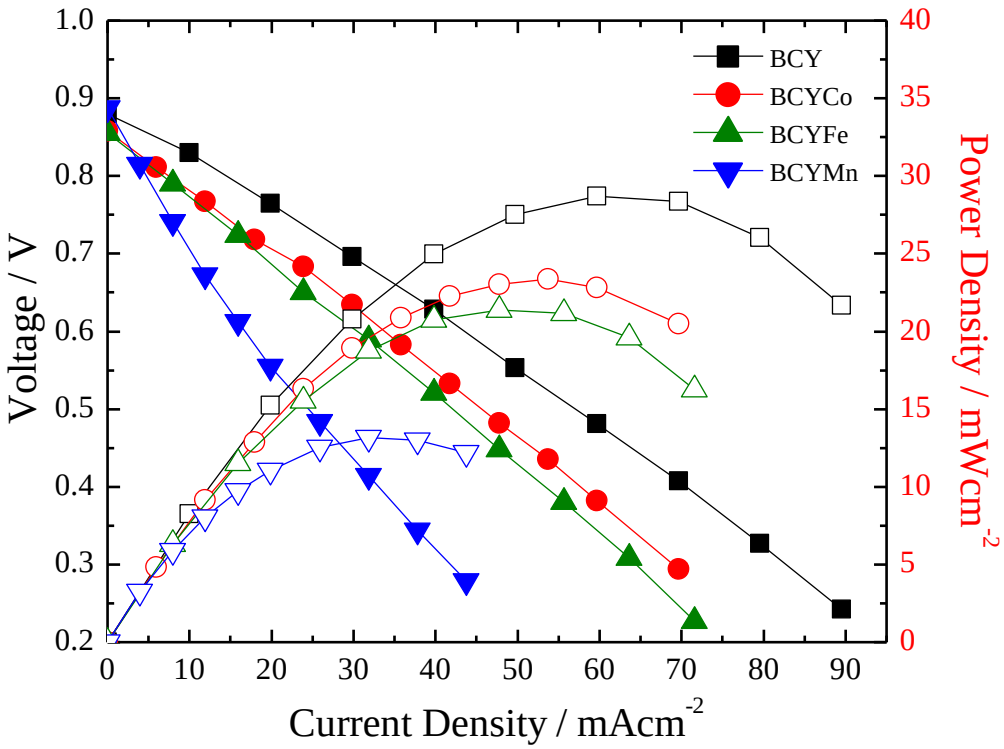

Fig. 3.7 Cell voltage (closed symbols) and power density (open symbols) curves of PCFCs using BCYM electrolytes with Pt electrodes as the both sides in moist air-100 % H_2 atmospheres at 800 ^{o}C (pH_2O = 1.9 kPa)

From these results, the transition metal-doped electrolytes may result in degradation of cell performance such as electrode overpotential, I-V and I-P with decreasing the electrical conductivity. Therefore, the decrease in the proton conductivity, concentration, and transport number studied in Chapter 2 has a significant effect on the fuel cell

performance. It is also believed that the choice of suitable oxide containing transition metal is effective to reduce of the overpotentials and to increase the energy conversion efficiency.

3.4 Conclusion

The electrodes overpotentials of transition metal doped $BaCe_{0.85}Y_{0.1}M_{0.05}O_{3-\delta}$ (M = Co, Fe and Mn) have been investigated. The electrode activities the doped and parent electrolytes was evaluated testing protonic ceramics fuel cell performance at 800 ^{o}C in moist air-100% H_2 atmospheres using Pt in both electrodes. $BaCe_{0.85}Y_{0.1}Mn_{0.05}O_{3-\delta}$ was found to have a poor cathode and cell performance. The performance was lower than $BaCe_{0.9}Y_{0.1}O_{3-\delta}$, $BaCe_{0.85}Y_{0.1}Co_{0.05}O_{3-\delta}$ and $BaCe_{0.85}Y_{0.1}Fe_{0.05}O_{3-\delta}$ electrolyte examined in this chapter. Analysis of impedance measurements and the current interruption allow concluding that the cell performance of the electrolyte in PCFC mode improved when the proton transport number increases. It was found that the order of increase of anodic and cathodic overpotentials coincided with the decreasing order of total conductivity of the electrolyte. Therefore, the introduction of a transition metal causes a decrease in proton concentration and transport number, leads to a decrease in conductivity. This decrease in electrical properties also affects the electrode overpotentials to the fuel cell.

3.5 Reference

[1] H. Iwahara, Y. Asakura, K. Katahira, M. Tanaka, *Solid State Ionics*, 168 (2004) 299–310

[2] H. Matsumoto, T. Shimura, H. Iwahara, T. Higuchi, K. Yashiro, A. Kaimai, T. Kawada, J. Mizusaki, *J. of Alloy and Compounds*, 408–412 (2006) 456–462

[3] C. Duan, J. Tong, M. Shang, S. Nikodemski, M. Sanders, S. Ricote, A. Almansoori, R. O'Hayre, *Science*, 349 (2015) 1321–1326

[4] J. W. Phair, S. P. S. Badwal, *Ionics* 12 (2006) 103–115

[5] N. Ito, M. Iijima, K. Kimura, S. Iguchi, *J. Power. Sources*, 152 (2005) 200–203

[6] S. Barison, M. Battagliarin, T. Cavallin, S. Daolio, L. Doubova, M. Fabrizio, C. Mortalo, S. Boldrini, R. Gerbasi, *Fuel Cells*, 8 (2008) 360–368.

[7] P. Babilo, T. Uda, S. M. Haile, *J. Mater. Res.*, 22 (2007) 1322–1330

[8] Y. Yamazaki, R. Hernandez-Sanchez, S. M. Haile, *Chem. Mater.*, 21 (2009) 2755–2762

[9] S. Nikodemski, J. Tong, C. Duan, R. O'Hayre, *Solid State Ionics*, 294 (2016) 37–42

[10] S. P. Shafi, L, Bi, S. Boulfrad, E. Traversa, *J. Am. Ceram. Soc.*, 162 (2015) 1498–1503

[11] J. Tong, D. Clark, M. Hoban, R. O'Hayre, *Solid State Ionics*, 181 (2010) 496–503

[12] Y. Wan, B. He, R. Wang, Y. Ling, L. Zhao, *J. Power. Sources*, 347 (2017) 14–20

[13] S. Ricote, N. Bonanos, *Solid State Ionics*, 181 (2010) 694–700

[14] W. Sun, S. Fang, L. Yan, and W. Liu, *J. Electrochem. Soc.*, 158, (2011) B1432–B1438

[15] K. C. Lee, M. B. Choi, D. K. Lim, B. Singh, and S. J. Song, J. Power Sources, 232, (2013) 224–233

[16] P. Ranran, W. Yan, Y. Lizhai, M. Zongqiang, *Solid State Ionics*, 177 (2006) 389–393

[17] Y. Lin, R. Ran, Y. Zheng, Z. Shao, W. Jin, N. Xu, J. Ahn, *J. Power. Sources*, 170 (2007) 38–41

[18] Y. Guo, R. Ran, Z. Shao, *Int. J. Hydrogen Energy*, 36 (2011) 1683–1691

[19] C. Zhang, Z. Du, H. Zhao, X. Zhang, *Electrochimica Acta*, 108 (2013) 369–375

[20] S.Y. Jeon, D.K. Lim, I.H. Kim, B. Singh, S.J. Song, *J. Electrochem. Soc.* 161 (2014) F754–F760

[21] H. Matsumoto, I. Nomura, S. Okada, T. Ishihara, *Solid State Ionics*, 180 (2008) 15–22

[22] L. Yang, C. Zuo, S. Wang, Z. Cheng, M. Liu, *adv. Mater.* 20 (2008) 3280–3283

[23] W. Sun, L. Yan, B. Lin, S. Zhang, W. Liu, *J. Power. Sources*, 195 (2010) 3155–3158

[24] T. Wu, R. Peng, C. Xia, *Solid State Ionics*, 179 (2008) 1505–1508

[25] M. Zunic, L. Chevallier, F. Deganello, A. D'Epifanio, *J. Power. Sources*, 190 (2009) 417–422

[26] L. Yang, Z. Liu, S. Wang, Y.M. Choi, C. Zuo, M. Liu, *J. Power. Sources*, 195 (2010) 471–474

[27] W. Sun, Z. Shi, S. Fang, L. Yan, Z. Zhu, W. Liu, *Int. J. Hydrogen Energy*, 35 (2010) 7925–7929

[28] N. Taniguchi, K. Hatoh, J. Niikura, T. Gamo, H. Iwahara, *Solid State Ionics*, 53–56 (1992) 998–1003

[29] H. Iwahara, T. Yajima, T. Hibio, H. Ushida, *J. Electrochem. Soc.*, 140 (1993) 1687–1691

[30] T. Hibio, A. Hashimoto, M. Suzuki, M. Sano, *J. Electrochem. Soc.* 149 (2002) A1503–A1508

[31] N. Maffei, L. Pelletier, A. McFarlan, *J. Power. Sources*, 136 (2004) 24–29

[32] Q. Ma, R. Peng, Y. Lin, J. Gao, G. Meng, *J. Power. Sources*, 161 (2006) 95–98

[33] K. Xie, Q. Ma, B. Lin, Y. Jiang, J. Gao, X. Liu, G. Meng, *J. Power. Sources*, 170 (2007) 38–41

[34] Q. Nian, L. Zhao, B. He, B. Lin, R. Peng, G. Meng, X. Liu, *J. of Alloy and Compounds*, 492 (2010) 291–294

[35] T. Shimura, H. Tanaka, H. Matsumoto, T. Yogo, *Solid State Ionics,* 176 (2005) 2945–2950

Chapter 4

Effect of dopant levels on the electrical properties of $Ba(Zr_{0.5}Ce_{0.4})_{1-x}Y_xO_{3-\delta}$ and $Sr(Zr_{0.5}Ce_{0.4})_{1-x}Y_xO_{3-\delta}$ proton conducting materials for hydrogen production

4.1 Introduction

A typical solid oxide fuel cell (SOFC) and solid oxide electrolysis cell (SOEC) is a three-layered structure ceramics composed of a dense electrolyte sandwiched between the anode and cathode [1-2]. The electrolyte is a principal part of the device and should meet specific requirements for efficient operation. One requirement is a high ionic conductivity, which should minimize ohmic loss. Another is a little or no electronic conduction to minimize leakage currents through the electrolyte. In addition a good chemical and mechanical strength in both oxidizing and reducing atmosphere as well as in high steam and carbon dioxide conditions [1-5]. Conventional SOECs are operated at 700-800 °C with the limited ionic conductivity of yttria stabilized zirconia (YSZ) which is the most typically used electrolyte [3]. Such high operation temperatures caused degradation of cell components, including electrode and electrolyte. Lowering the operating temperature (under 600 °C) is necessary to enhance performance and durability of electrolytes as well as the other cell components. Perovskite-type proton conducting oxides are candidate electrolyte materials for intermediate temperature operation of solid oxide electrochemical cell devices [1, 6-15].

As mentioned above (Chapter 1, Fig. 1.7), the activation energy for proton transport in these materials is lower than that for oxide ion conduction, thus making them suitable for SOEC operation within this regime [7,15]. These materials have a chemical formula of $AB_{1-x}M_xO_{3-\delta}$, consisting of a divalent alkali earth ion at the *A*-site and a tetravalent ion at the *B*-site. Partial substitution of *M* with a trivalent ion leaded to the resulting formation of oxide ion vacancies.

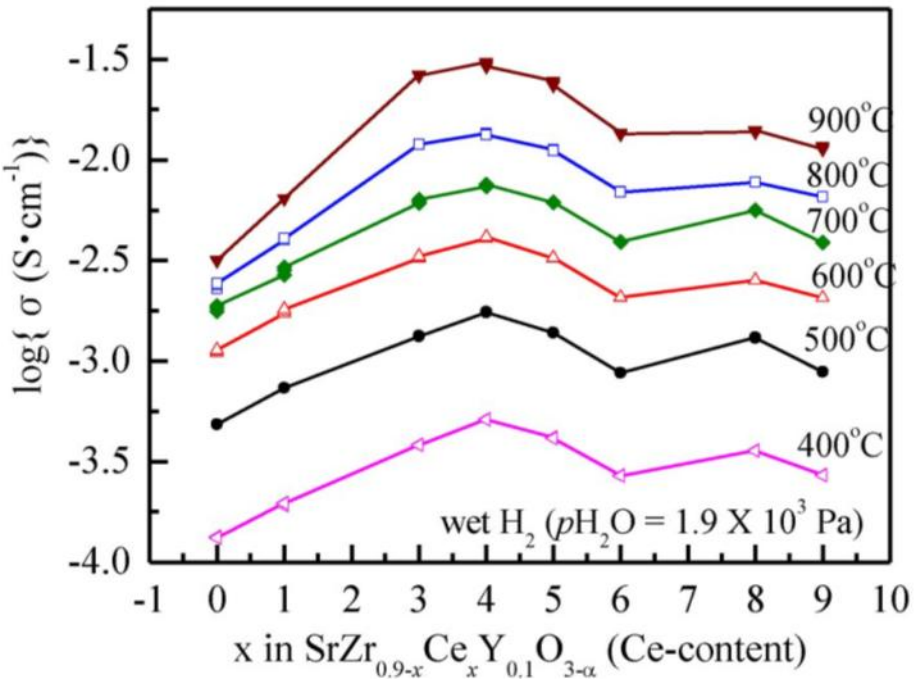

Fig. 4.1 The electrical conductivity of $SrZr_{0.9-x}Ce_xY_{0.1}O_{3-\delta}$ (x = 0-0.9) in wet 1% H_2 atmosphere [15]

Aiming to use for SOEC operating at 600 °C, the composition of yttrium-doped strontium zirconate-cerate oxide proton conducting electrolyte such as $SrZr_{0.9-}$

$_xCe_xY_{0.1}O_{3-\delta}$ (x = 0-0.9) was determined [15]. Fig. 4.1 shows the electrical conductivity of $SrZr_{0.9-x}Ce_xY_{0.1}O_{3-\delta}$ (x = 0-0.9) in wet 1% H_2 atmosphere. After examining the composition series of $SrZr_{0.9-x}Ce_xY_{0.1}O_{3-\delta}$, it has been found the highest electrical conductivity of 4.5×10^{-3} S cm^{-1} at 600 °C in wet 1% H_2 and a sufficient thermodynamic stability at x = 0.4. Also, $SrZr_{0.5}Ce_{0.4}Y_{0.1}O_{3-\delta}$ electrolyte has been successfully tested for chemical stability and steam electrolysis at 600 °C [15-17]. However, the reason for the appearance of maximum conductivity in the $SrZr_{0.5}Ce_{0.4}Y_{0.1}O_{3-\delta}$ case is still unclear. Also, for get better SOEC performance, higher proton conductivity is desired for the electrolyte material.

In this chapter investigated the reason for the highest conductivity of $SrZr_{0.5}Ce_{0.4}Y_{0.1}O_{3-\delta}$ in $SrZr_{0.9-x}Ce_xY_{0.1}O_{3-\delta}$ system. Also, starting from $SrZr_{0.5}Ce_{0.4}Y_{0.1}O_{3-\delta}$, the effects of Ba substitution for Sr and the doping level of Y on the crystal structure, the electrical properties, proton concentration as well as chemical stability of the following compositions $A(Zr_{0.5}Ce_{0.4})_{1-x}Y_xO_{3-\delta}$, ($A$= Ba, Sr and x=0.1, 0.2) was investigated, which are referred to hereafter as BZCY and SZCY or composition-specifically as BZCY541, BZCY$(54)_{8/9}2$, SZCY541 and SZCY$(54)_{8/9}2$, respectively. The proton conductivity is influenced by the sort of dopant [9,12]. The choice of yttrium in the present study is supported by the notion that it resulted to high proton conductivity for many cases of alkali earth cerates and zirconates [6,7,10].

4.2 Experimental

4.2.1 Preparation of BZCY and SZCY electrolytes

SZCY samples were prepared by solid state reaction, using $SrCO_3$ (Rare metallic, 99.99 %), ZrO_2 (Tosoh, 99.9 %), CeO_2 (Rare metallic, 99.99 %), and Y_2O_3 (Mitsuwa's pure chemicals, 99.99 %) as starting materials. Stoichiometric amounts of the appropriately weighed powders were mixed in a mortar with ethanol and then pressed in to a pellet. The pellets were subsequently calcined at 1300 °C for 10 h in air and regrind. The obtain powders were ball-milled at 300 rpm for 1h with 15 mm zirconia ball and, pressed into pellets at 300 MPa for 10 min and finally sintered at 1600 °C for 10 h in air.

BZCY541, BZCY$(54)_{8/9}2$, SZCY541 and SZCY$(54)_{8/9}2$ were prepared by chemical solution method, using a aqueous solution. $Ba(NO_3)_2$ (Wako, 99.9%), $ZrO(NO_3)_2{\cdot}xH_2O$ (Zirconyl nitrate solution, Aldrich, 35 wt %, 99 %), $Sr(NO_3)_2$ (Soekawa, Chemicals, 99.9 %) $Ce(NO_3)_3{\cdot}6H_2O$ (Kanto Chemical Co., 99.99 %) and $Y(NO_3)_3{\cdot}6H_2O$ (Mitsuwa's Pure Chemicals, 99.9 %). Stock solutions of the metal nitrates in aqueous form with concentrations determined by an inductively coupled plasma technique (ICP, Shimadzu, ICPE-9000) were weighed and added into an aqueous solution sequentially with continuous stirring. citric acid (Wako, 99%) and ethylene diamine tetraacetic acid (EDTA, Dojindo, 99%) were then added as chelating agents with the molar ratio of total metal ions to citric acid and EDTA set at 1:1.5:1.5. Ammonium hydroxide solution (Chameleon Regent, 28.0 %) was added to promote the dissolution of EDTA and to adjust the pH to 9 ~ 10. The solution was then heated under stirring to evaporate water until it changed into a viscous gel. The gel was then heat-treated at 240 °C in a vacuum oven to obtain a solid precursor, and then calcined at 900 °C for 10 hours in air. The synthesis powders were then ball milled in ethanol at

300 rpm for 4 days with 2 mm zirconia balls and dried at 120 ^{o}C for overnight in vacuum oven and sieved (150 µm), pressed into pellets at 250 MPa for 10 min and finally sintered at 1600 °C for 10 h in air. For protection against BaO loss of pellets during the long exposure to high temperature (above 1600 ^{o}C), the pellets were covered in a powder of same composition powders during sintering process (Fig. 4.2).

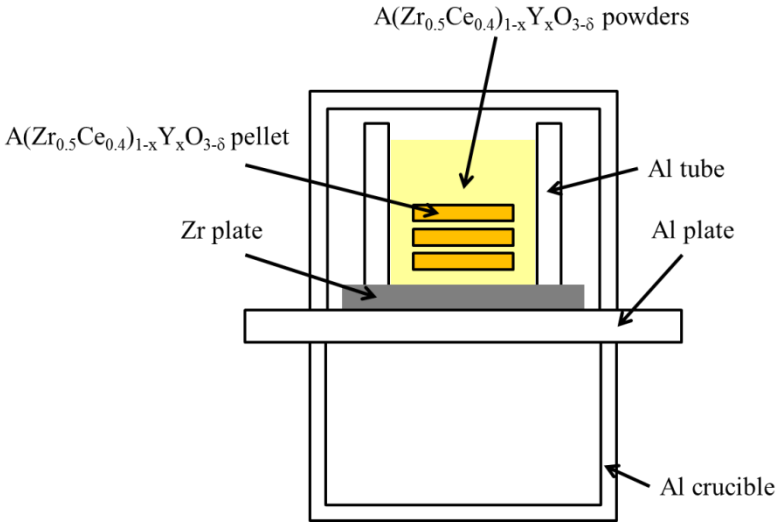

Fig. 4.2 Schematic diagram of the sintering process

4.2.2 Characterization

Phase purity of the samples was confirmed by X-ray diffraction (XRD, Rigaku, Cu Kα, 40 kV–40 mA) with Cu-Kα radiations. Diffraction patterns were obtained in the 2 theta range between 10^{o} to 80^{o} with a step size of 2 degree/min. The microstructures and chemical compositions of the sintered samples were observed via field emission

scanning electron microscopy (Hitachi, High-Technologies SU8000) and a scanning electron microscopy (Topcon, SM-350) equipped with energy dispersive X-ray spectroscopy, (Oxford, INCA energy 300 EDS) whereas the specific surface area of the as-prepared powders were determined using Brunauer - Emmett - Teller analysis (Microtrac BEL, Bellsorp mini II).

The electrical conductivity of BZCY and SZCY were measured by a 2- and 4-probe AC impedance method. The 4-probe method can provide a more precise total conductivity using a bar type sample, whereas the bulk and grain contribution are easily discernable in the later 2-probe configuration using a disk type sample. With respect to the bar shaped samples, platinum paste (Tanaka Kikinzoku, TR-7907) and platinum lead wires were applied on four points on the bar samples and subsequently heat-treatment at 950 ^{o}C for 1 h. Impedance responses were collected with an AC amplitude of 200 mV in the frequency range between 1 MHz and 0.1 Hz using an impedance analyzer (Princeton Applied Research Versa STAT 3), in moist air and 1% H_2 atmosphere (pH_2O = 1.9 kPa). Platinum paste was also brushed on both sides of the sintered disk samples and heat-treatment at 950 ^{o}C for 1 h in air. The electrical conductivity was measured using an impedance analyzer (Solartron, SI 1287) in a 2-probe arrangement under the same conditions as stated for the four-probe configuration. Measurements were repeated at least three times to confirm reproducibility for both configurations. Well-resolved impedance spectra arc in the Nyquist representation were analyzed in terms of an equivalent circuit model using the least squares refinement program Z-View (Scribner Associates Inc., Southern Pines, NC). Each arc from the experimental data was represented by a parallel combination of a resistance (R) and a constant-phase element

(CPE). From the intercepts of impedance plots with the real axis, the resistances (bulk and grain boundary) of the samples were determined. The proton concentration of the samples was evaluated by thermogravimetric analysis (TGA, Netzsch, STA449F3 Jupiter). Since the incorporation of water is described by Eq. (4.1), the proton concentration can be calculated from the amount of incorporated water.

$$H_2O + V_O^{\cdot\cdot} = O_O^x + 2H_i^{\cdot} \qquad (4.1)$$

For quantify the water incorporated into the perovskite structure, sintered powder samples were first heated in dry N_2 atmosphere at 1200 °C for 1 hour to obtain complete sample dehydration. Subsequently weight changes of the samples were then measured in moist 10 % N_2-Ar in the temperature range 100 -1200 °C (pH_2O = 1.9 kPa). The Raman spectra of SZCY samples were measured with an inVia Raman Microscope (Renishaw) at room temperature for the fully hydrated samples under moist 10 % O_2-Ar atmosphere (pH_2O = 1.9 kPa).

4.3 Results and discussion

4.3.1 Proton-conducting properties of $SrZr_{0.9-x}Ce_xY_{0.1}O_{3-\delta}$ based materials

Fig. 4.3 shows the XRD patterns of SZCY as sintered at 1600 ^oC. These electrolytes show the orthorhombic perovskite structure without secondary phase. Also, relative density obtained for all the synthesized compositions were above this can be justified by ionic radius of Ce^{4+} and Zr^{4+} in the same six-coordination configuration (Ce^{4+} = 87 pm and Zr^{4+} = 72 pm) [18].

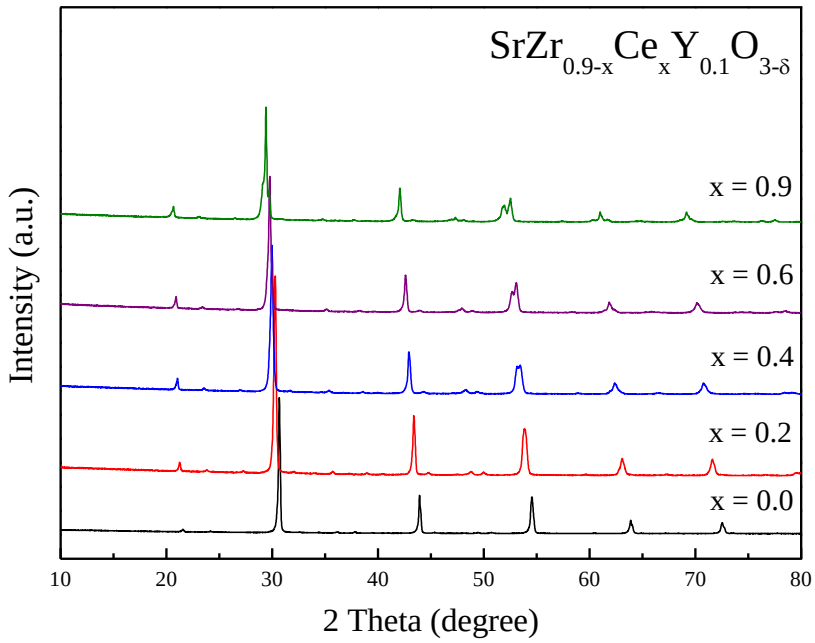

Fig. 4.3 XRD patterns of $SrZr_{0.9-x}Ce_xY_{0.1}O_{3-\delta}$ (x= 0.0, 0.2, 0.4, 0.6 and 0.9) samples as sintered at 1600 ^oC for 10 h in air

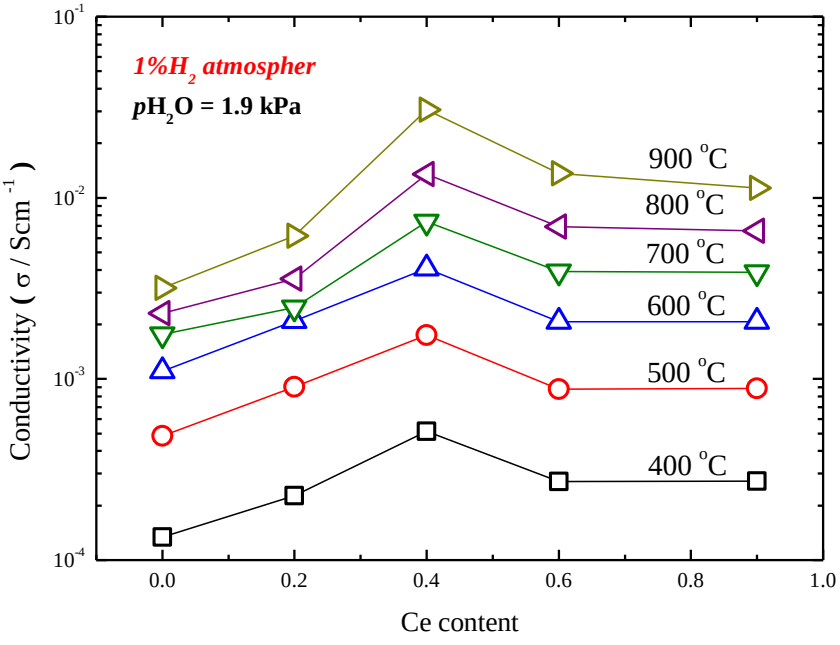

Fig. 4.4 The electrical conductivity of $SrZr_{0.9-x}Ce_xY_{0.1}O_{3-\delta}$ in moist 1% H_2 atmosphere (pH_2O = 1.9 kPa)

Fig. 4.4 shows the electrical conductivities of SZCY samples in moist 1% H_2 atmosphere. The composition of SZCY541 sample shows the highest electrical conductivity at range of 400 to 900 ^oC in 1% H_2 atmosphere. Also, it found the highest electrical conductivity of 4.1×10^{-3} S cm^{-1} at 600 °C. The electrical conductivity results in this study are consistent with the results reported by Matsumoto [15] for SZCY system. TGA was used to evaluate the proton concentration of the samples at different temperatures as reported in the experimental part. The concentrations of the proton were estimated from the differences in the sample weight with reference to the ones under the dry-atmosphere at 1200 ^oC, assuming that the hydration took place as Eq. (4.1). Fig. 4.5 shows the temperature dependence on the proton concentration of SZCY samples. The proton concentration reached a constant value at low temperature, and is the characteristic value for the composition. SZCY541 shows the highest proton concentration in this system for the examined specimen. Thus, the results of proton concentration were providing evidence to support that SZCY541 has the highest conductivity value in this system. Considering the electrical neutrality, the maximum proton concentration might reach the dopant level. However, the maximum proton concentration could not reach the dopant level and was dependent on the Zr/Ce ratio of the cation on the *B*-site. A plausible explanation of the discrepancy between doping level and maximum proton limit has been proposed in the works of Kreuer [7] and Schober [19].

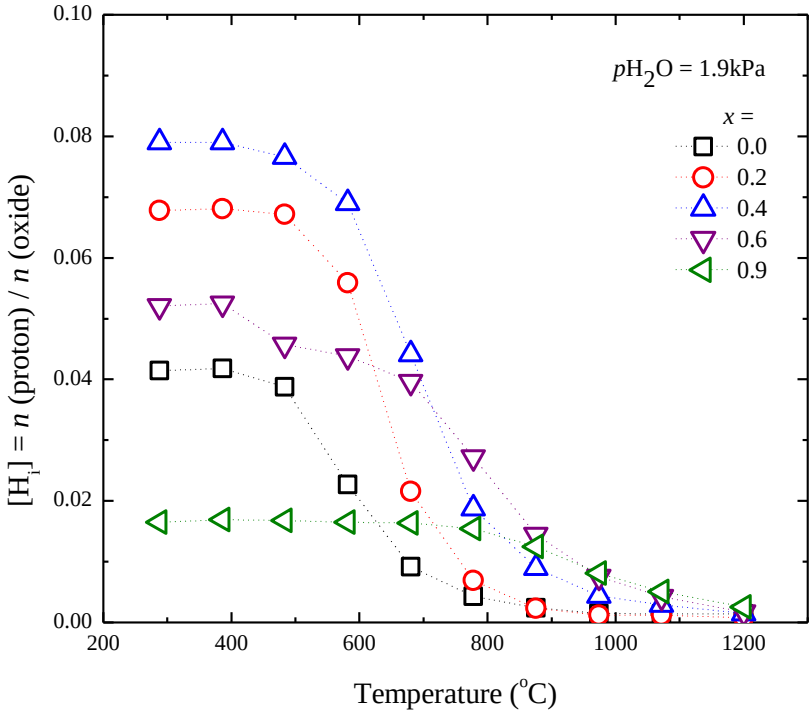

Fig. 4.5 The temperature dependence of proton concentration for $SrZr_{0.9-x}Ce_xY_{0.1}O_{3-\delta}$

They suggested that the reduction in saturation limit with respect to the dopant concentration was as a result of slight substitution of the Y dopant on the Sr^{2+} *A*-site. Kreuer also associated this phenomenon to the decay of oxygen sites into two sites with different affinities towards hydration [19-23] especially in orthorhombic perovskites. Fig. 4.6 shows the Raman spectra of SZCY samples. The SZCY clearly shows the three Raman spectrums for range of 100-200 cm^{-1}. These spectra might be attributed to the stretching mode of the oxygen ion around the strontium ion because the peaks were not shifted as the Zr^{4+} or Ce^{4+} content increasing. The Raman band 320-320 cm^{-1} corresponds to the Sr-O stretching mode as observed in $SrZr_{0.9-x}Ce_xY_{0.1}O_{3-\delta}$ system. It is worth noting that large peaks observed differently within the range of 320-450 cm^{-1}

depending on the composition of SZCY. The results reported, in the Sata [24] and Mineshige [25] research that the range at around 340 and 400 cm^{-1} were attributed to the CeO_6 and ZrO_6 stretching, respectively. Thus, the peak of the Raman spectrum which shifted to a higher wavenumber was observed as the Zr^{4+} concentration increased. The shift might indicate that the bonding energy of the octahedron around Ce^{4+} increased with the increase in the Zr^{4+} content [26-28]. Also, the satellite peaks on right side of the main peak are probably connected with vibrations involving oxygen ions for strontium [26]. Moreover, the half band width of this large peak is broader when the cation on the B-site is a mixture of Ce^{4+} and Zr^{4+}. This might indicate that the symmetry of the octahedron around the *B*-site is reduced when the *B*-site is a mixture of Ce^{4+} and Zr^{4+}. It is supposed that this broadening and wavenumber shift as *B*-site mixture of Zr/Ce samples indicate the change of local lattice distortion in solid solutions [24]. According to Raman spectroscopic data reported by Karlsson et al, *B*-site doping leads to significant local distortions in the symmetry of the perovskites [29-30]. They concluded that a narrow window of external structural distortion thus exist where favorable fast proton transport takes place and hence enhanced proton conductivity. A Raman bands related to the oxygen vacancies [25,31] were observed in the range 500-580 cm^{-1} and might be attributed to un-hydration oxygen vacancies which do not take part in the hydration reaction. This band range was not observed for $SrZr_{0.5}Ce_{0.4}Y_{0.1}O_{3-\delta}$. Which implies almost completed field oxygen vacancies and coupled with the structural distortion in symmetry around 340 and 400 cm^{-1} probably resulted in the observed highest proton conductivity obtained for $SrZr_{0.5}Ce_{0.4}Y_{0.1}O_{3-\delta}$ compared to the case of $SrZr_{0.3}Ce_{0.6}Y_{0.1}O_{3-\delta}$, and $SrCe_{0.9}Y_{0.1}O_{3-\delta}$, where the structural distortion is quite limited.

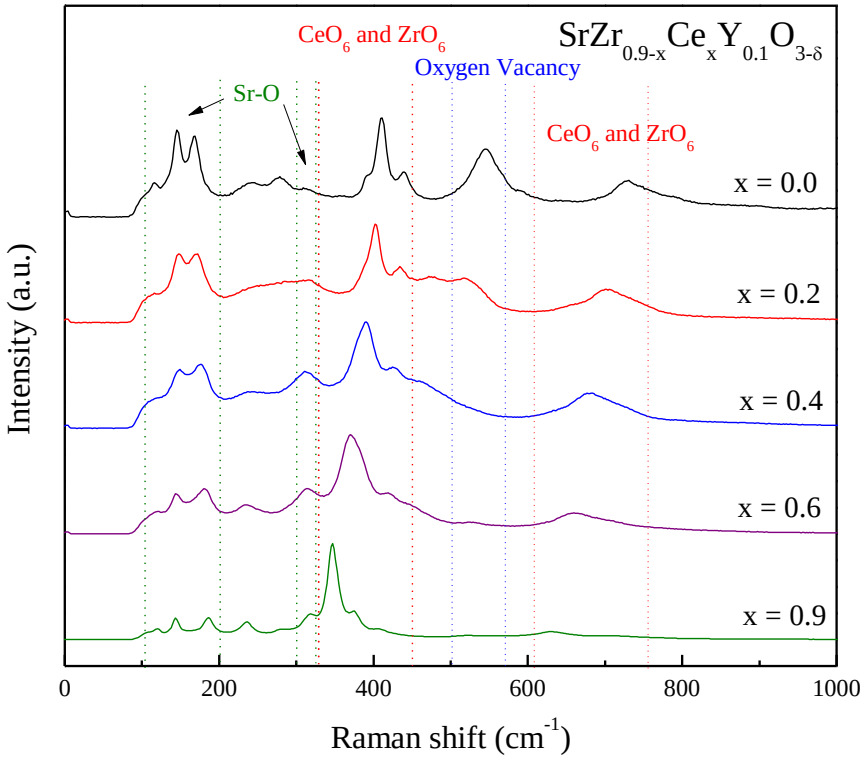

Fig. 4.6 Raman spectra of $SrZr_{0.9-x}Ce_xY_{0.1}O_{3-\delta}$ at room temperature for the fully hydrated as samples

Consider the hydration energy based on the assumption that the partial oxygen vacancies cannot take part in the hydration. In the present system, the electrical neutrality condition is expressed as follows:

$$[Y'_{\mathrm{Ce\ or\ Zr}}] = [H_{\mathrm{i}}^{\cdot}] + 2\left[V_{\mathrm{O(1)}}^{\cdot\cdot}\right] + 2[V_{\mathrm{O(2)}}^{\cdot\cdot}] \qquad (4.2)$$

$[Y'_{Ce\ or\ Zr}]$ is the concentration of Y at either Ce or Zr site, and $[H_i^{\cdot}]$ represents the proton concentration while $V_{\mathrm{O(1)}}^{\cdot\cdot}$ and $V_{\mathrm{O(2)}}^{\cdot\cdot}$ denote oxide ion vacancy involved in hydration and immobile oxide ion vacancy which do not take part in hydration, respectively. The

hole concentration is considered much lower than the protons and oxide ion vacancies. The equilibrium condition for the water incorporation reaction from Henry's law, Eq. (4.1), is written as;

$$K_{\mathrm{Hydr}} = \frac{[\mathrm{H}_i^{\cdot}]^2}{[O_O^x][V_O^{\cdot\cdot}]P_{\mathrm{H_2O}}} = exp\left(-\frac{\Delta G^{\circ}}{RT}\right) \qquad (4.3)$$

where K_{Hydr} and ΔG are hydration equilibrium constant and hydration standard free energy, respectively. Using Eq. (4.2) and (4.3) the hydration standard free energy can be expressed as shown Eq. (4.4).

$$\Delta G^{\circ} = -RTln\left(\frac{2[H_i^{\cdot}]^2}{p_{H_2O}\left\{[Y'_{\mathrm{Ce\ or\ Zr}}]-[H_i^{\cdot}]-[V_{\mathrm{O(2)}}^{\cdot\cdot}]\right\}}\right) \qquad (4.4)$$

The amount of the inert oxygen vacancy can be estimated from Eq. (4.2);

$$2[V_{\mathrm{O(2)}}^{\cdot\cdot}] = [Y'_{\mathrm{Ce\ or\ Zr}}] - [H_i^{\cdot}]_{limit} \qquad (4.5)$$

Fig. 4.7 represented the hydrogen energy of SZCY using Eq. (4.4). The hydration energy increased as Zr^{4+} content increased. However, this phenomenon is different from that of the proton saturation limit. The obtained values are summarized in table 4.1 for all the compositions. Thus, the hydration energy increases with Zr content. Zr content also increased the immobile oxygen vacancies which do not take part in the hydration reaction. SZCY541 is thought to have better conditions for hydration reaction, an essential ingredient for high proton concentration and conductivity in this system. The proton concentration might be dependent on the symmetry.

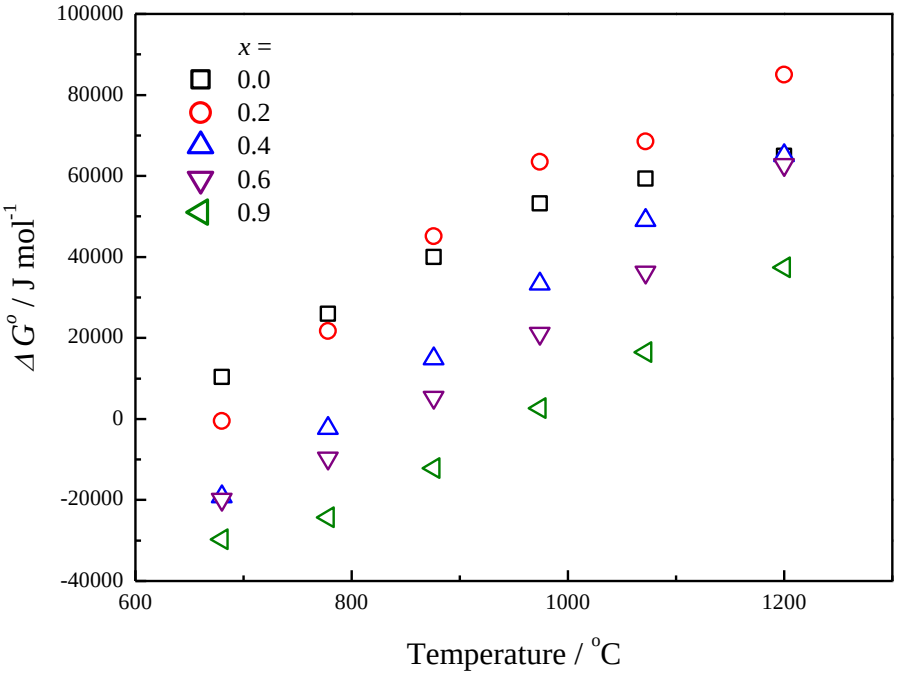

Fig. 4.7 Temperature dependence on the hydration Energy of $SrZr_{0.9-x}Ce_xY_{0.1}O_{3-\delta}$

Table 4.1 Estimated proton saturation limits and concentration of inert oxygen vacancy of the at 288 °C as prepared electrolytes

Ce contents (ratio, x)	0.0	0.2	0.4	0.6	0.9
$[H_i^{\cdot}]_{limit}$	0.041	0.068	0.079	0.052	0.016
$[V_{O(2)}^{\cdot\cdot}]$	0.030	0.016	0.011	0.024	0.042

4.3.2 Phase identification and microstructures of BZCY and SZCY electrolytes

Fig. 4.8 shows the XRD patterns of BZCY541, BZCY(54)$_{8/9}$2, SZCY541 and SZCY(54)$_{8/9}$2 as sintered at 1600 °C. All the patterns over the observed 2θ range (10° to 80°) confirm reflections characteristic of single phase perovskite-type structure. The diffraction peaks of SZCY541 and SZCY(54)$_{8/9}$2 matched the characteristic reflections

of the ABO_3 orthorhombic perovskite structure with space group *Pnma* [32-33]. BZCY(54)$_{8/9}$2 and BZCY541 were indexed to a cubic perovskite with space group *Pm3m* [34-37]. In both BZCY and SZCY systems, a noticeable peak shift towards the lower 2 theta angle was observed with a change of yttrium dopant level from 10 to 20 mol %. This can be justified by the larger ionic radius of Y^{3+} compared to those of Zr^{4+} and Ce^{4+} (six coordination, Shannon's ion radii, Zr^{4+} = 72pm, Ce^{4+} = 87 pm and Y^{3+} = 90pm) [18].

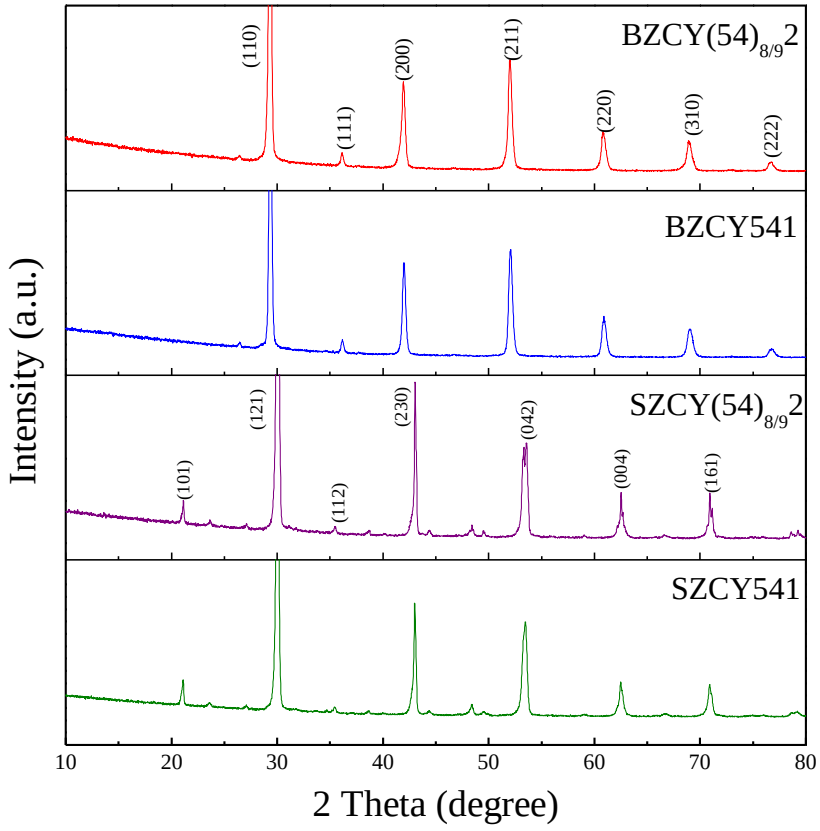

Fig. 4.8 XRD patterns of BZCY and SZCY disks after sintered at 1600 ^{o}C for 10h in air

Table 4.2 Lattice parameter, unit cell volume and relative density of BZCY and SZCY

Composition	Lattice parameter (Å)	Unit cell volume ($Å^3$)	Relative density (%)	Crystal system
BZCY541	4.3204	80.67	95.8	Cubic
$BZCY(54)_{8/9}2$	4.3278	81.06	96.4	Cubic
SZCY541	a= 5.9524 b= 8.3833 c= 5.8994	294.38	95.7	Orthorhombic
$SZCY(54)_{8/9}2$	a= 5.9713 b= 8.3651 c= 5.9081	295.11	98.3	Orthorhombic

The microstructures of the as-sintered pellets are presented in Fig. 4.9. Detailed analysis of the surfaces revealed grain sizes of 2-3 μm for BZCY samples and 3-5 μm for the SZCY samples. The fractured cross sectional surfaces of BZCY541 and BZCY(54)8/92 revealed some open pores. Whereas SZCY541 and $SZCY(54)_{8/9}2$ cross sectional surfaces appeared more denser with very limited pore. It is worth mentioning that the microstructures and grain sizes obtained here for BZCY and SZCY systems were similar to those as reported in literature. Those studies indicated that typical yttrium doped barium zirconates or strontium zirconate partially substituted with ceria prepared by a variety of routes and sintered at 1600 ^oC [9,15,33,38].

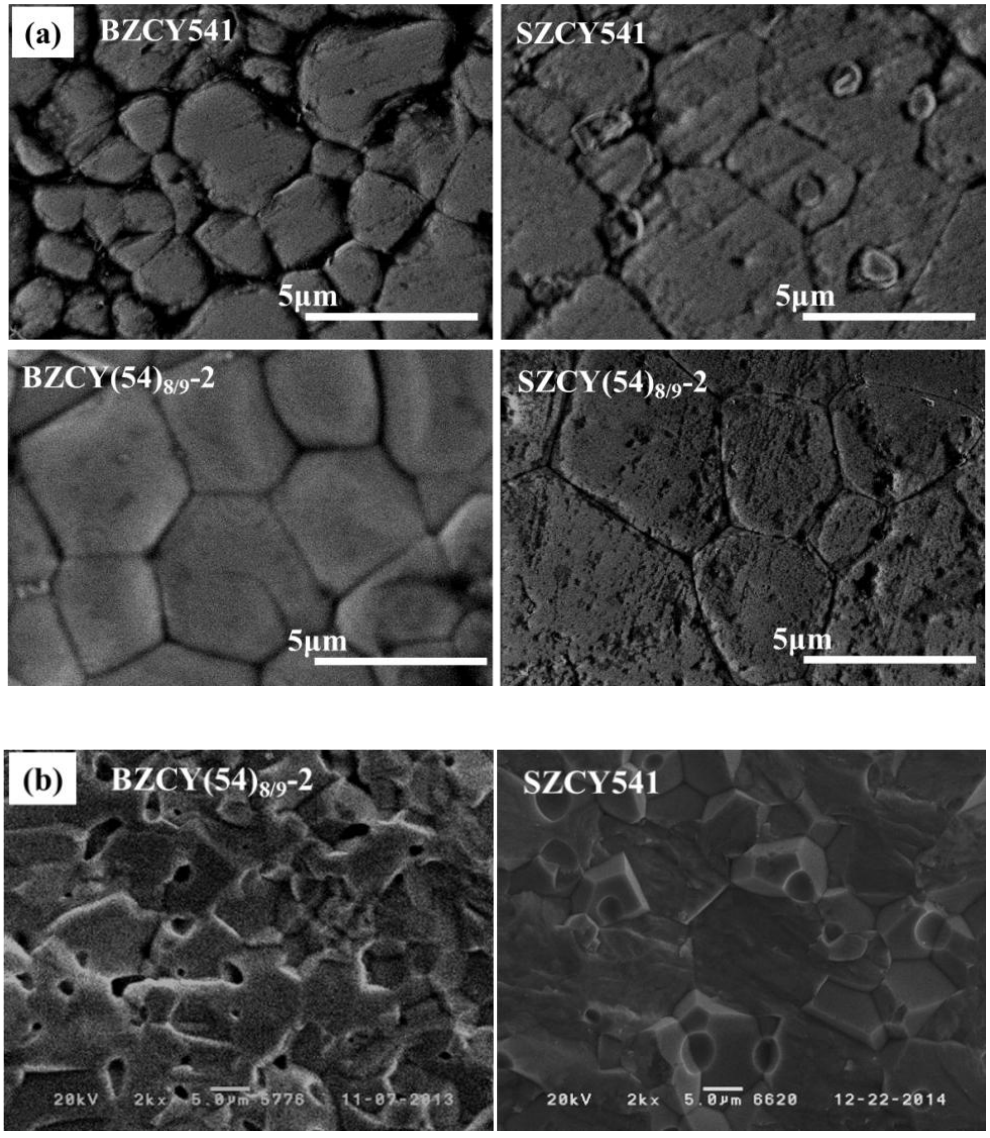

Fig. 4.9 The SEM images of (a) the surfaces of BZCY and SZCY pellets sintered at 1600 ^{o}C for 10 h (polished surface), and the representative (b) fractured cross sectional images for BZCY(54)$_{8/9}$2 and SZCY541.

4.3.3 The electrical conductivity of BZCY and SZCY electrolytes

In Fig. 4.10, the electrical conductivity was measured as a function of temperature with the standard 4-probe method in moist air and 1% H_2. As observed, the total conductivity in moist air atmosphere shows slightly higher values with respect to those obtained under 1% H_2 due to p-type conductivity in this atmosphere [39-40]. The conductivity plots of the BZCY samples demonstrated an initial linear increase in the temperature under 500 ^oC, and thereafter the plots show a bending tendency with increasing temperature. The initial behavior is due to hydration. The temperature range of above 600 ^oC, dehydration took place and a consequent loss of protonic carriers [15]. On the inversely, the shape of the conductivity tendency for SZCY appeared more linear within the measured range of temperature, probably because a significant conductivity from other species states to occur above 600 ^oC even with the dehydration of protons within the material [40]. The total conductivity of $BZCY(54)_{8/9}2$ reached 1.0×10^{-2} Scm^{-1} at 500 ^oC and 1.4×10^{-2} Scm^{-1} at 600 C in 1% H_2. $BZCY(54)_{8/9}2$ exhibited the highest conductivity over the entire temperature range with an almost half-order increase comparing to SZCY541. According to the report of Zuo et al., the $BaZr_{0.1}Ce_{0.7}Y_{0.2}O_{3-\delta}$ shows conductivity values is higher than that of $BZCY(54)_{8/9}2$ at 600 °C whereas at temperatures ≤ 500 °C $BZCY(54)_{8/9}2$ [13]. Moreover some recent reports have studied the thermodynamics stability of the 0.1 zirconium concentration of $BaZr_{0.1}Ce_{0.7}Y_{0.2}O_{3-\delta}$ in water rich environments [36]. Obviously high proton conductivity is a prerequisite for these materials to be considered viable; however, adequate material stability should also be achieved. Some recent investigations have equally demonstrated that both acceptable electrical conductivity and reasonable

thermodynamic stability can be achieved for materials with close concentrations of cerium and zirconium (Zr/Ce ratio 4:4, 5:3) [41-42].

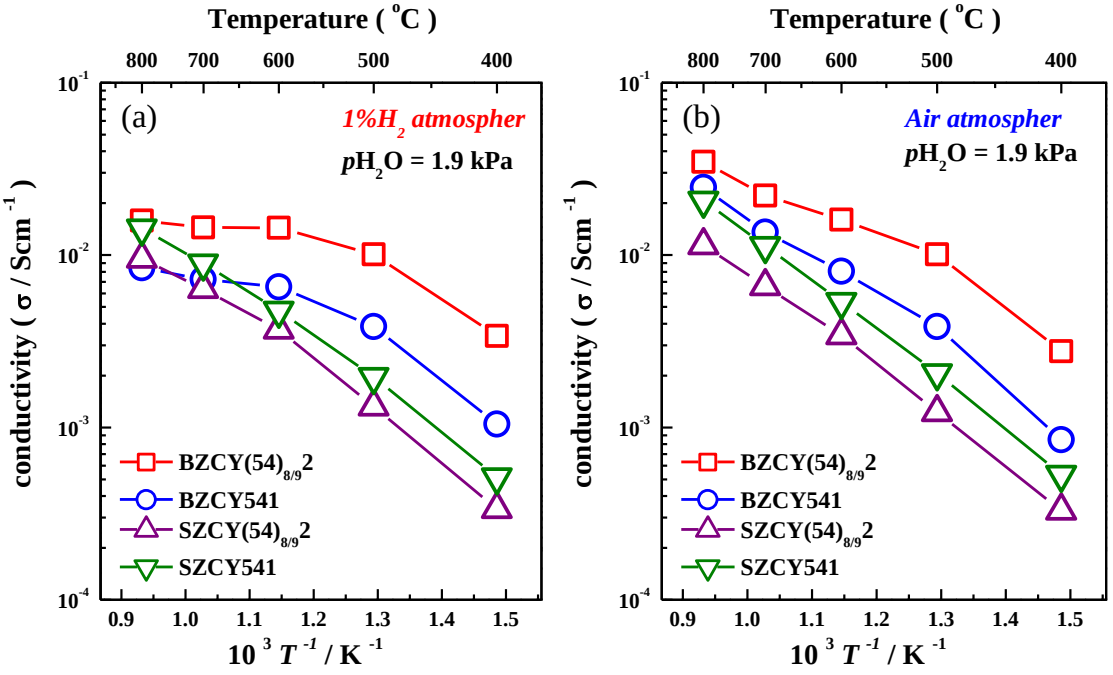

Fig. 4.10 Arrhenius plots of the electrical conductivity of BZCY and SZCY in moist (a) 1 % H_2 and (b) air atmosphere (pH_2O = 1.9 kPa)

Based on these considerations, the present $BZCY(54)_{8/9}2$ seems to exhibit a good balance between conductivity and stability. To examine the applicability to SOEC the evaluation of its thermodynamic stability at 600 °C in 80% steam was investigated. Fig. 4.11(a) shows the conductivity plots of $BZCY(54)_{8/9}2$ and SZCY541in 80% steam as a function of time under moist 1% H_2 and air atmospheres. Both samples show fairly constant conductivity after 100 h of steam treatment. Fig. 4.11(b) shows the XRD

patterns of BZCY(54)$_{8/9}$2 pellets before and after 80% steam exposure. It is clear from the XRD pattern that BZCY(54)$_{8/9}$2 shows no change after treatment, and thus confirming the tolerance of this composition to the condition employed.

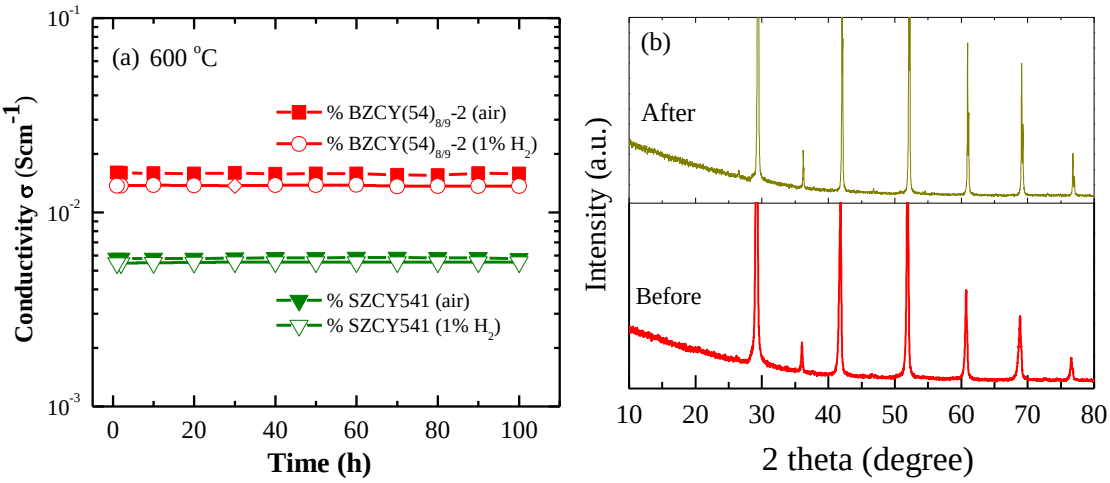

Fig. 4.11 (a) The electrical conductivity of BZCY(54)$_{8/9}$2 and SZCY541 in 80 % steam for 100 h under moist 1% H_2 and air atmosphere (pH_2O = 1.9 kPa), (b) XRD patterns of BZCY(54)$_{8/9}$2 before and after exposure to 80 % steam at 600 °C

Nyquist plots of typical impedance method for BZCY(54)$_{8/9}$2 and SZCY541 were recorded in air at 400 °C with a 2-probe AC impedance arrangement as shown in Fig. 4.12(a). As observed, the plots consist of three separated arc, a high frequency semicircle corresponding to the bulk resistance, an intermediate frequency arc attributed to the grain boundary resistance, and a low frequency region ascribed to the electrode response. A similar spectrum was obtained in moist 1% H_2 as shown in Fig. 4.12(b).

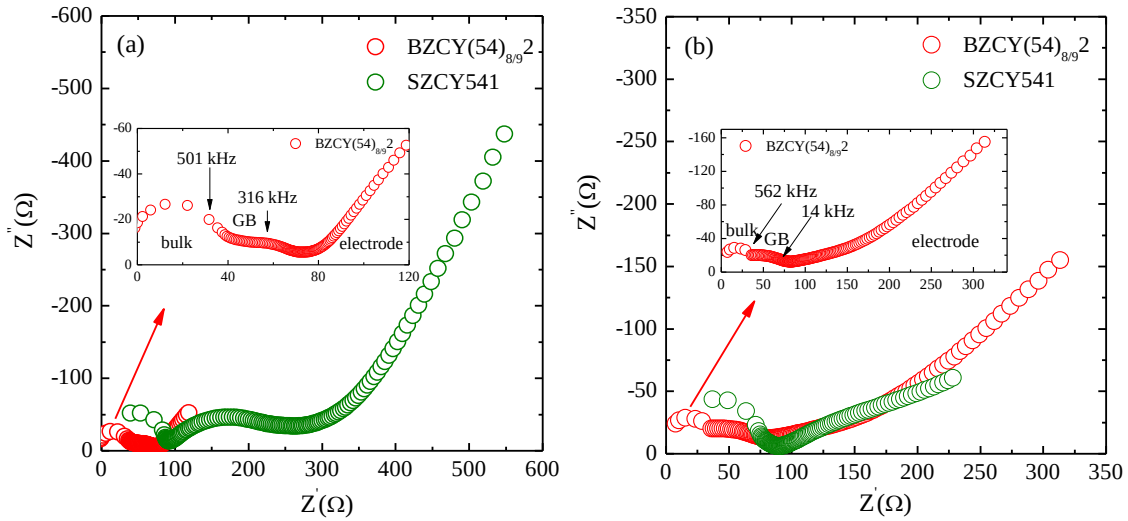

Fig. 4.12 Nyquist plot of $BZCY(54)_{8/9}2$ and SZCY541at 400 ^{o}C in moist (a) air and (b) 1% H_2 atmosphere (pH_2O = 1.9 kPa), the inset plot in both figure are expanded view of the $BZCY(54)_{8/9}2$ sample

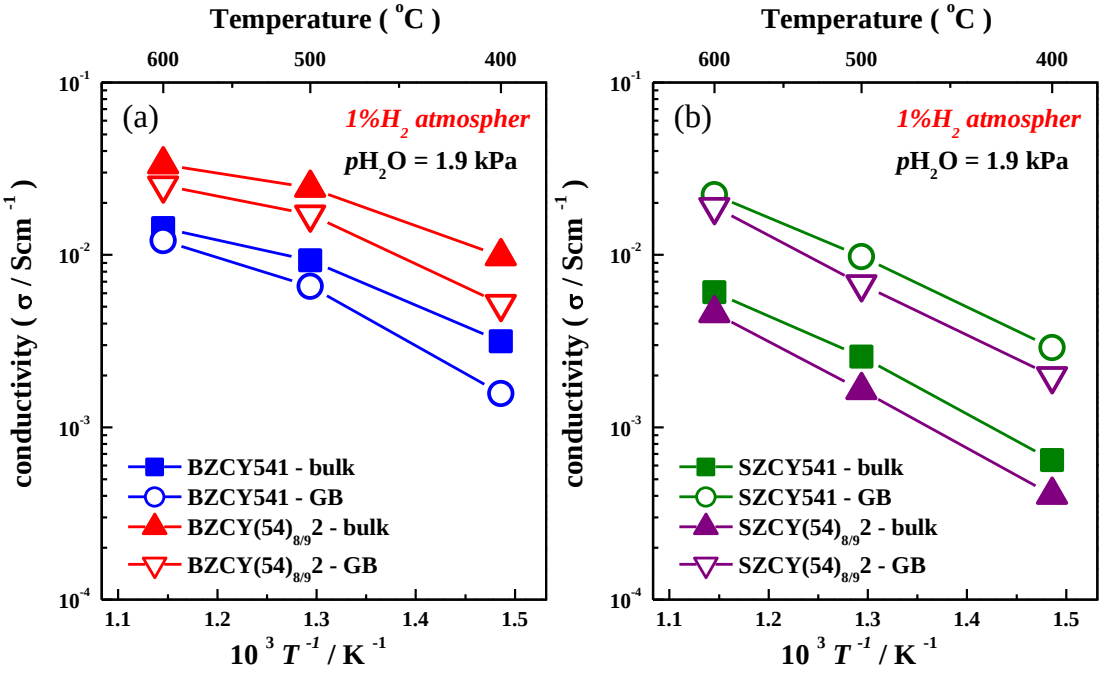

Fig. 4.13 Temperature dependence of the bulk and grain boundary conductivity of (a) BZCY and (b) SZCY measured in moist 1% H_2 atmosphere (pH_2O = 1.9 kPa)

Fig. 4.13 shows the bulk and grain boundary conductivities of the samples were measured in moist 1% H_2 plotted as function of inverse temperature. From the plots, the bulk conductivity of the BZCY specimen increased by about half an order of magnitude as Y concentration increases from 10 to 20 mol %. However the bulk conductivity of the SZCY counterparts is almost the same for 10 and 20 mol % Y concentration. In addition, the grain-boundary contribution are the major source of resistance to the total conductivity of BZCY541 and BZCY(54)8/92 while the bulk represent the minor component. Whereas with respect to SZCY541 and SZCY(54)8/92 the bulk contribution are the major source of resistance to the total conductivity and are not dominated by the grain boundary contribution.

4.3.4 Proton concentration of BZCY and SZCY electrolytes

TGA was used to evaluate the proton concentration of the samples at different temperature as reported in the experimental part. Fig. 4.14 shows the temperature dependence on the weight change of BZCY and SZCY in dry and wet N_2 atmosphere. As shown in both figures, a successive weight change in all the samples is observed with a stepwise raise in temperature. This weight gains reflected hydration within the crystal lattices. An analysis of the weight gain allowed the estimation of proton concentration in the as tested composition. Plots of the proton concentration profiles as a function of temperature are shown in Fig. 4.15(a).

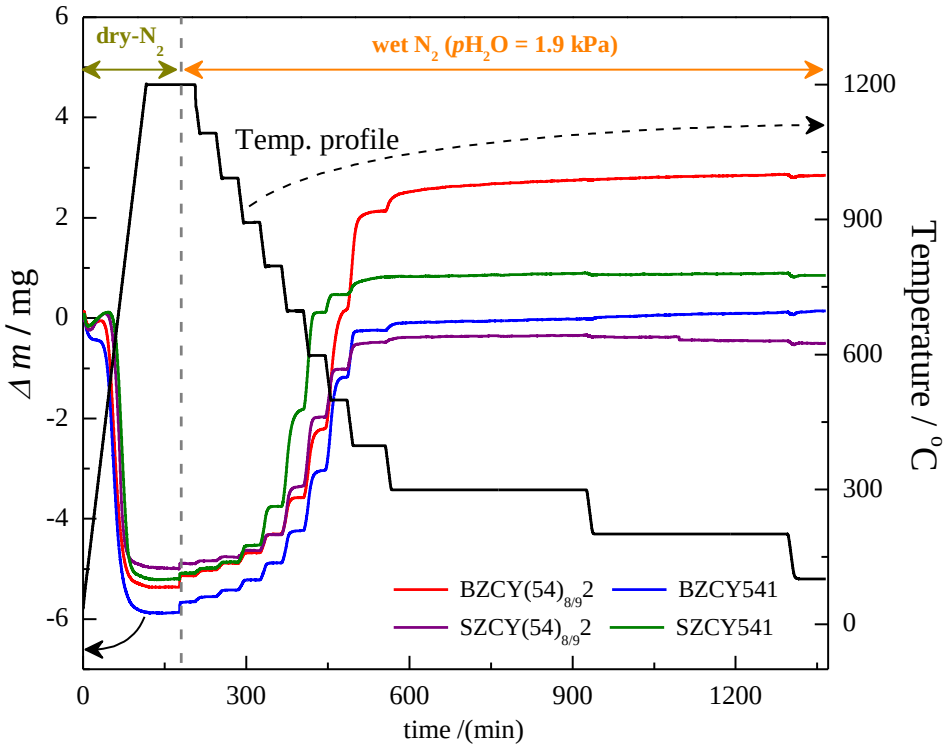

Fig. 4.14 Weight change behavior of BZCY and SZCY sintered powder as a function of time together with the temperature profile (black line), when the atmosphere is change from dry N_2 to wet N_2 atmosphere (pH_2O = 1.9 kPa)

This fact is worthy of notice that, the maximum proton concentration did not attain the initial dopant level in all the four samples investigated, which is not uncommon with other prominent proton conductors [7]. Fig. 4.15(b) shows the maximum proton concentration limit measured at 100 °C versus the Y-dopant content for BZCY and SZCY systems. For comparison, the theoretically possible proton content is also plotted. It can be observed that the experimentally obtained values for both BZCY and SZCY are much lower than the theoretically possible values and the difference is more significant with increasing Y content. A maximum proton content of 9.5 mol %, almost approaching the limit of 10 % for BZCY541 (with 10 %Y) was achieved whereas

SZCY541 showed a maximum limit of 7.85 mol %. Both results are consistent with previously reported values [7,19]. With an increase in the Y-dopant level to 20 mol %, BZCY(54)$_{8/9}$2 retains a maximum proton limit of 17.1 mol % while SZCY(54)$_{8/9}$2 decreased to ~ 6.03 mol %. This observation is consistent with the fact that BZCY(54)$_{8/9}$2 has the highest magnitude of protonic conductivity than SZCY(54)$_{8/9}$2. As above mentioned at proton concentration result of SZCY samples, the reduction in saturation limit with respect to the dopant concentration was as a consequence of slight substitution of the Y dopant on the Sr^{2+} *A*-site. In line with the above discussions it believe that the 20 mol % Y-dopant level in SZCY(54)8/92 results in an increased number of oxygen vacancies, with most of them having a relatively low affinity towards hydration.

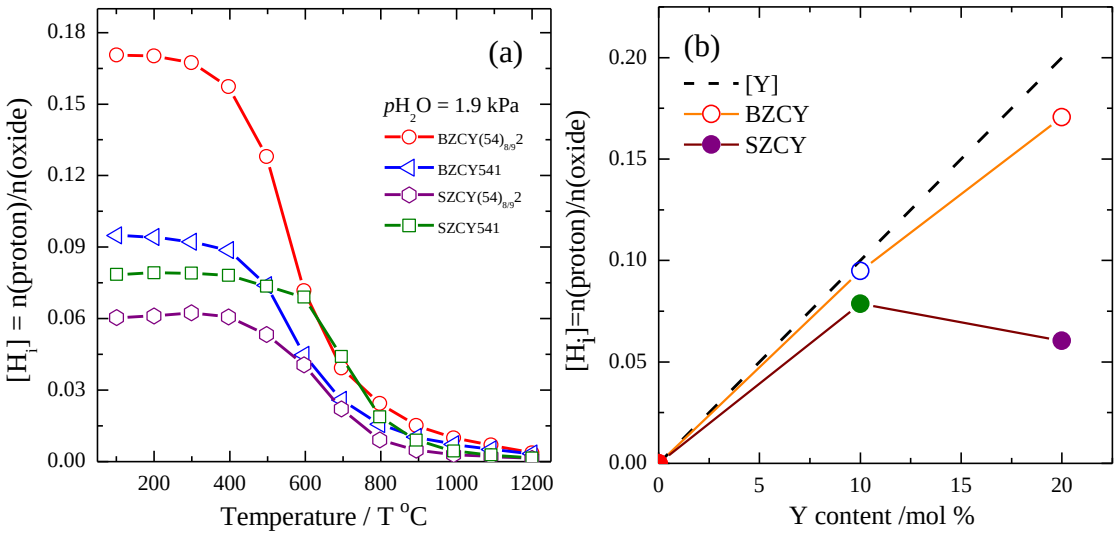

Fig. 4.15 Typical (a) proton concentration in BZCY541, BZCY(54)$_{8/9}$2, SZCY541 and SZCY(54)$_{8/9}$2 (b) proton concentration as a function of yttrium content (pH_2O = 1.9 kPa)

The hole concentration is considered much lower than the protons and oxide ion vacancies. The standard hydration enthalpies and entropies can be presented as a follows;

$$kT \ln K = T\Delta S_{hydr} - \Delta H_{hydr} \quad (4.6)$$

$$K_{\mathrm{Hydr}} = \exp\left\{\frac{\Delta S^{o}_{\mathrm{Hydr}}}{R}\right\} \exp\left\{\frac{-\Delta H^{o}_{\mathrm{Hydr}}}{RT}\right\} \quad (4.7)$$

Using Eq. (4.3) and (4.6) the equilibrium constant K_{Hydr} can be expressed as shown Eq. (4.7). Where $\Delta S^{\circ}_{\mathrm{Hydr}}$, $\Delta H^{\circ}_{\mathrm{Hydr}}$ represent the standard molar entropy and enthalpy change associated with hydration. The extracted equilibrium constant of hydration are plotted versus the reciprocal temperature for BZCY(54)$_{8/9}$2 and SZCY(54)$_{8/9}$2 as shown in Fig. 4.16 for the higher temperature region, $\Delta \mathrm{H}^{\circ}_{\mathrm{Hydr}}$ and $\Delta \mathrm{S}^{\circ}_{\mathrm{Hydr}}$ were subsequently obtained from the slope and intercept, respectively. The obtained values are summarized in Table 4.3 for all the compositions. The results reveal an increase in the exothermic hydration enthalpy with a change of the Y doping from 10 mole % to 20 mole % in the BZCY system. The value becomes more negative when Ba^{2+} is replaced with Sr^{2+} in the *A*-site for SZCY541. Even though this tendency is opposite to the trend in proton incorporation, the observation is however in agreement with the works of Kreuer [7] and Schober et al [22]. Similar reports by Bjørheim et al [21] have also shown hydration enthalpies for ABO_3 perovskites becoming more exothermic with decreasing ionic radius of *A*-site cation (Sr^{2+} = 144 pm and Ba^{2+} = 166 pm) and suggesting a correlation with the radius or radius ratio of the different ions.

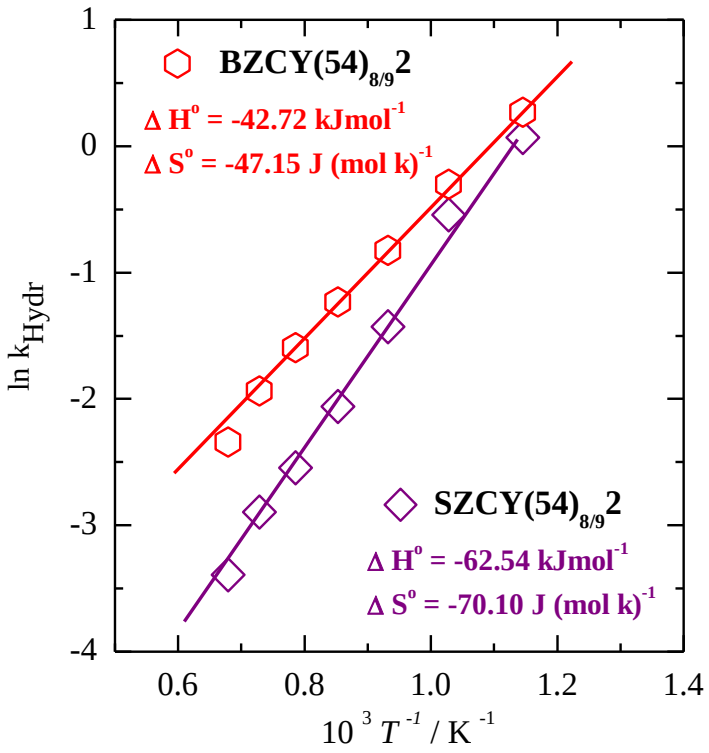

Fig. 4.16 Arrhenius plots of the equilibrium constant as a function of the reciprocal of temperature for $BZCY(54)_{8/9}2$ and $SZCY(54)_{8/9}2$

Table 4.3 Thermodynamics properties of enthalpy and entropy for as prepared samples at 600 ^{o}C

Composition	ΔH^{o} (kJ mol^{-1})	ΔS^{o} (J mol^{-1}k^{-1})
BZCY541	-41.64	-46.89
$BZCY(54)_{8/9}2$	-42.72	-47.15
SZCY541	-70.00	-72.86
$SZCY(54)_{8/9}2$	-62.54	-70.10

The mobility of protons in the compositions was estimated from the proton concentration and bulk conductivity in moist 1% H_2 with the assumption that a majority of the protons reside in the bulk. Proton mobility was thus evaluated using the Nernst Einstein expression;

$$\mu_{\mathrm{H}} = \sigma_{H_{bulk}} \mathrm{V}_m / F[H_i^{\cdot}] \qquad (4.8)$$

where $\sigma_{\mathrm{H}_{bulk,}}, F, \mu_{\mathrm{H}}, [H_{\mathrm{i}}^{\cdot}]$ and V_m denoted the bulk proton conductivity, Faraday constant, mobility of proton, proton concentration and the molar volume of the compositions respectively [7,10,23].

Table 4.4 Estimated proton saturation limits, concentration of inert oxygen vacancy at 288 ^{o}C, and the mobility of proton at 600 ^{o}C of the as prepared electrolytes

Composition	$[H_i^{\cdot}]_{\mathrm{limit}}$	$[V_{o(2)}^{\cdot\cdot}]$	V_{m} (cm^3)	$\mu_{\mathrm{H}(cm^2S^{-1}V^{-1})}$
BZCY541	0.095	0.003	48.581	1.60×10^{-4}
$BZCY(54)_{8/9}2$	0.171	0.012	48.815	2.35×10^{-4}
SZCY541	0.079	0.011	48.319	4.01×10^{-5}
$SZCY(54)_{8/9}2$	0.060	0.070	44.429	5.18×10^{-5}

The calculated values for V_m are presented in Table 4.4. This approach is suitable only within the range 400 °C ≤ T ≤ 600 °C in which proton conduction is predominant. At higher temperatures just as discussed above oxygen ions in principle contribute to the conductivity. In which case alternative measurement approaches are necessary and will not be considered in the present study. Fig. 4.17 shows plots of the proton mobility

against the reciprocal temperature within the range 400 °C ≤ T ≤ 600 °C with respect to the bulk conductivity.

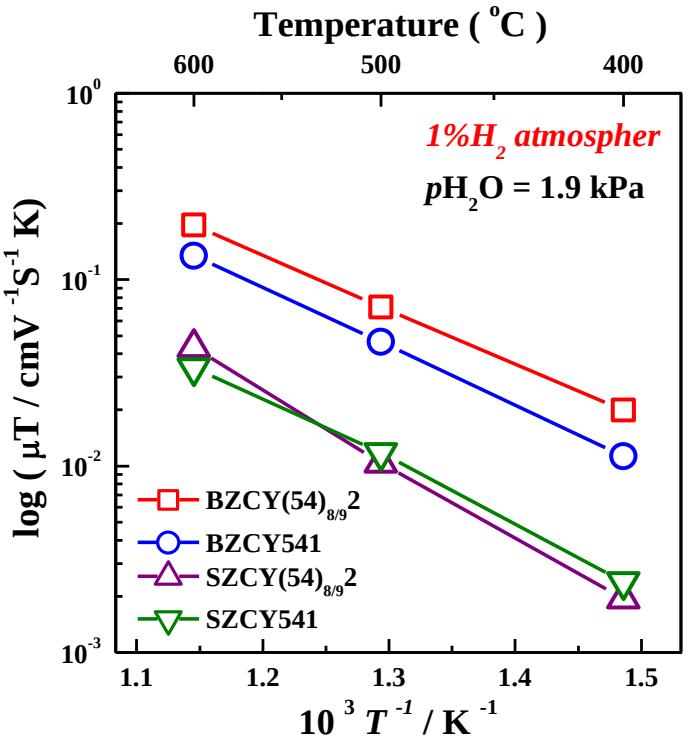

Fig. 4.17 The Arrhenius plots of the bulk proton conductivity of BZCY and SZCY samples in moist 1% H_2 atmosphere (pH_2O = 1.9 kPa)

Table 4.5 Activation energy of bulk and grain boundary for the mobility of proton determined at 400 – 600 °C in moist 1% H_2 atmosphere

Activation Energy (eV)	BZCY541	$BZCY(54)_{8/9}2$	SZCY541	$SZCY(54)_{8/9}2$
$E_{a(bulk)}$	0.63	0.58	0.67	0.78
$E_{a(GB)}$	0.76	0.81	0.62	0.73

Fitting the proton mobility data in Arrhenius form Eq. (4.7) allows for the determination of activation energies.

$$\mu_{\mathrm{H}} = \frac{A}{T}\exp(-\frac{E_a}{k_b T}) \qquad (4.7)$$

The obtained values are shown in table 4.5. The magnitude of the bulk conductivity as well as their activation energies for proton conduction for all the composition are in agreement with literature values for analogous composition [33,37,41]. SZCY541 and $SZCY(54)_{8/9}2$ showed almost comparable proton mobility in moist 1% H_2, whereas $BZCY(54)_{8/9}2$ showed a slightly higher proton mobility than BZCY541 in response to an increase in Y-dopant concentration from 10 to 20 mol %. Table 4.4 summaries the obtained proton mobility for the compositions at 600 °C. These results are also consistent with the trend in conductivity discussed above for $BZCY(54)_{8/9}2$, and BZCY541 respectively. The conductivities of all the samples differ somewhat significantly and approximately 2 orders of magnitude apart between $BZCY(54)_{8/9}2$ (highest) and $SZCY(54)_{8/9}2$ (lowest) whereas the mobility is just within less than half order of magnitude for all the samples. Thus the major difference in conductivity between all the samples originates mostly from the difference in proton concentration and probably the magnitude of grain boundary contribution especially in the SZCY systems.

4.4 Conclusion

In this study investigated the reasons for the highest conductivity of $SrZr_{0.5}Ce_{0.4}Y_{0.1}O_{3-\delta}$ in $SrZr_{0.9-x}Ce_xY_{0.1}O_{3-\delta}$ system. The composition of $SrZr_{0.5}Ce_{0.4}Y_{0.1}O_{3-\delta}$ has the highest proton concentration in the $SrZr_{0.9-x}Ce_xY_{0.1}O_{3-\delta}$ system. The Raman spectra indicates that the bonding energy of the octahedron around the *B*-site increases with the increase in the Zr^{4+} content, and the symmetry of the octahedron around the *B*-site was reduced when the *B*-site is a mixture of Ce^{4+} and Zr^{4+}. The hydration energy and immobile oxygen vacancies increased with Zr content, the $SrZr_{0.5}Ce_{0.4}Y_{0.1}O_{3-\delta}$ shows only oxide ion vacancy involved in hydration. This phenomenon was related to the higher conductivity and proton concentration. The effect of substituting Sr^{2+} with Ba^{2+} in $A(Zr_{0.5}Ce_{0.4})_{1-x}Y_xO_{3-\delta}$, (*A*= Ba, Sr and x=0.1, 0.2) was investigated in an attempt to find an optimum composition with both high conductivity and acceptable stability. Thermo-gravimetric analyses revealed that almost similar proton concentration in both $SrZr_{0.5}Ce_{0.4}Y_{0.1}O_{3-\delta}$ and $SrZr_{0.44}Ce_{0.36}Y_{0.2}O_{3-\delta}$ with a constant Zr/Ce fraction of 5:4. Both samples have almost comparable proton conductivities in moist 1% H_2. Whereas $BaZr_{0.44}Ce_{0.36}Y_{0.2}O_{3-\delta}$ has higher proton mobility than $BaZr_{0.5}Ce_{0.4}Y_{0.1}O_{3-\delta}$ in response to an increase in Y-dopant and retained the highest proton conductivity of 1.4×10^{-2} Scm^{-1} in humidified 1 % H_2 at 600 °C as well as excellent chemical stability under 80 % steam for 200 hours. The bulk and grain boundary contributions on the conductivity were strongly dependent on the A-site host (Sr^{2+} or Ba^{2+}), with the grain boundary response being the main source of resistance in the $Ba(Zr_{0.5}Ce_{0.4})_{1-x}Y_xO_{3-\delta}$ system relative to the $Sr(Zr_{0.5}Ce_{0.4})_{1-x}Y_xO_{3-\delta}$. The bulk response however is the main limiting factor to the conductivity of the $Sr(Zr_{0.5}Ce_{0.4})_{1-}$

$_xY_xO_{3-\delta}$ system. The major difference in conductivity among the studied compositions originates from the difference in proton concentration and the magnitude of the grain boundary contribution. Considering the suitable balance between conductivity and stability achieved by $BaZr_{0.44}Ce_{0.36}Y_{0.2}O_{3-\delta}$, it can be conclude that this composition seems a better choice electrolyte for SOEC at intermediate temperature.

4.5 Reference

[1] L. Bi, S. Boulfrad, E. Traversa, *Chem. Soc. Rev.*, 43 (2014) 8255–8270

[2] M. Ni, M.K.H. Leung, D.Y.C Leung, *Int. J. Hydrogen Energy* 33 (2008) 2337–2354

[3] A. Hauch, S.D. Ebbesen, S.H. Jensen, M. Mogensen, *J. Mater. Chem*., 18 (2008) 2331–2340

[4] W. Doenitz, E. Erdle, *Int. J. of Hydrogen Energy*, 10 (1985) 291–295

[5] M.A. Laguna-Bercero, *J. Power. Sources*, 203 (2012) 4–16

[6] H. Iwahara, T. Esaka, H. Uchida, N. Maeda, *Solid State Ionics*, 3/4 (1981) 359–363

[7] K.D. Kreuer, *Solid State Ionics*, 125 (1999) 285–302

[8] K.H. Ryu, S.M. Haile, *Solid State Ionics*, 125 (1999) 355–67

[9] P.A. Stuart, T. Unno, J.A. Kilner, S.J. Skinner, *Solid State Ionics*, 179 (2008) 1120–1124

[10] T. Yajima, H. Iwahara, *Solid State Ionics*, 50 (1992) 281–286

[11] H. Matsumoto, M. Okubo, S. Hamajima, K. Katahira, H. Iwahara, *Solid State Ionics*, 152 (2002) 715–720

[12] A.K. Azad, J.T.S. Irvine, *Solid State Ionics*, 178 (2007) 635–640

[13] C. Zuo, S. Zha, M. Liu, M. Hatano, M. Uchiyama, *Adv. Mater.*, 18 (2006) 3318–3320

[14] H. Matsumoto, I. Nomura, S. Okada, T. Ishihara, *Solid State Ionics* 179 (2008) 1486–1489

[15] H. Matsumoto, T. Sakai, Y. Okuyama, *Pure Appl. Chem.*, 85 (2013) 427–435

[16] H. Matsumoto. Proton conduction in cerium and zirconium based perovskites. In: Ishihara T, editor. *Perovskite oxide for solid oxide fuel cells*, New York: Springer Science LLC; 2009. p. 243–259.

[17] T. Sakai, S. Matsushita, H. Matsumoto, S. Okada, S. Hashimoto, T. Ishihara, *Int. J. of Hydrogen Energy*, 34 (2009) 56–63

[18] R.D. Shannon, *Acta Cryst.*, A32 (1976) 751–767

[19] T. Schober, *Solid State Ionics*, 145 (2001) 319–324

[20] K.D. Kreuer, Th. Dippel, Y.M. Baikov, J. Maier, *Solid State Ionics*, 86-88 (1996) 613–620

[21] T.S. Bjørheim, A. Kuwabara, I. Ahmed, R. Haugsrud, S. Stølen, T. Norby, *Solid State Ionics*, 181 (2010) 130–137

[22] T. Shober, F. Krug, W. Schiling, *Solid State Ionics*, 97 (1997) 369–373

[23] H. Uchida, H. Yoshikawa, T. Esaka, S. Ohtsu, H. Iwahara, *Solid State Ionics*, 36 (1989) 89–95

[24] N. Sata, H. Yugami, Y. Akiyama, H. Sone, N. Kitamura, T. Hattori, M. Ishigame, *Solid State Ionics*, 125 (1999) 383–387

[25] A. Mineshige, S. Okada, K. Sakai, M. Kobune, S. Fujii, H. Matsumoto, T. Shimura, H. Iwahara, Z. Ogumi, *Solid State Ionics*, 162-163 (2003) 41–45

[26] R.R. Chien, C.-S. Tu, V. Hugo Schmidt, S.-C. Lee, C.-C. Huang, *Solid State Ionics*, 181 (2010) 1251–1257

[27] R.Q. Long, Y.P. Huang, H.L. Wan, *Journal of Raman Spectroscopy*, 28 (1997) 29–32

[28] B.K. Kim, H.O. Hamaguchi, *Physica Status Solidi*, 203 (1997) 557–563

[29] M. Karlsson, A. Matic, P. Berastegui, L. Borjesson, *Solid State Ionics*, 176 (2005) 2971–2974

[30] M. Karlsson, A. Matic, C.S. Knee, I. Ahmed, S.G. Eriksson, L. Borjesson, *Chem. Mater.*, 20 (2008) 3480–3486

[31] Q. Chen, T.W. Huang, M. Baldini, A. Hushur, V. Pomjakushin, S. Clark, W. L. Mao, M. H. Manghnani, A. Braun, T. Graule, *J. Phys. Chem.*, C115 (2011) 24021–24027

[32] L.S. Cavalcante, A.Z. Simoes, J.C. Sczancoski, V.M. Longo, R. Erlo, M.T. Escote, E. Longo, J.A. Varela, *Solid State Ionics*, 9 (2007) 1020–1027

[33] I.M. Hung, Y.J. Chiang, J.S.C. Jang, J.C. Lin, S.W. Lee, J.K. Chang, C.S. Hsi, *J. of Eur. Ceram. Soc.*, 35 (2015) 163–170

[34] S. Ricote, N. Bonanos, A. Manerbino, W.G. Coors, *Int. J. of Hydrogen Energy*, 37 (2012) 7954–7961

[35] D. Medvedev, J. Lyagaeva, S. Plaksin, A. Demin, P. Tsiakaras, *J. Power. Sources*,

273 (2015) 716–723

[36] E. Fabbri, A. D'Epifanio, E. Di Bartolomeo, S. Licoccia, E. Traversa, *Solid State Ionics*, 179 (2008) 558–564

[37] P. Sawant, S. Varma, B.N. Wani, S.R. Bharadwaj, *Int. J. of Hydrogen Energy*, 37 (2012) 3848–3856

[38] D.K. Lim, C.J. Park, M.B. Choi, C.N. Park, S.J. Song, *Int. J. of Hydrogen Energy*, 35 (2010) 10624–10629

[39] S.M. Babiniec, S. Ricote, N.P. Sullivan, *Int. J. of Hydrogen Energy*, 40 (2015) 9278–9286

[40] S. Ricote, N. Bonanos, H.J. Wang, R. Haugsrud, *Solid State Ionics*, 185 (2011) 11–17

[41] N. Nasani, P.A.N. Dias, J.A. Saraiva, D.P. Fagg, *Int. J. of Hydrogen Energy*, 38 (2013) 8461–8470

[42] S. Barison, M. Battagliarin, T. Cavallin, L. Doubova, M. Fabrizio, C. Mortalo, S. Boldrini, L. Malavasi, R. Gerbasi, *J. Mater. Chem.*, 18 (2008) 5120–5128

Chapter 5

Investigation of the electrical conductivity in indium and yttrium-doped barium zirconate proton conducting materials

5.1 Introduction

Trivalent-cation-doped barium zirconate shows proton conduction and is a promising candidate electrolyte material for intermediate temperature solid oxide fuel cells and steam electrolysis [1-7]. The material has the cubic perovskite-type structure. Partial substitution of trivalent cation for the tetravalent zirconium ion causes the formation of oxide ion vacancy and the hydration of the oxide ion vacancy with ambient moisture results in the formation of protonic charge carrier [1]. For example, yttrium doped barium zirconate (BZY) could be written as:

$$Y_2O_3 + 2Zr_{Zr}^{x} + O_o^{x} \rightarrow 2Y_{Zr}' + V_o^{\cdot\cdot} + 2ZrO_2 \qquad (5.1)$$

Yttrium has been reported to be the best dopant as long as the bulk proton conductivity is concerned [2], whereas the material is characterized by high grain-boundary resistance. One reason for the high grain-boundary resistance is due to the poor sinterability, causing limited grain growth even by sintering at high temperature (~1800 ^{o}C) [8-10]. Meanwhile, barium zirconate based electrolytes have been considered that grain boundary (GB) conductivity is lower than of that the bulk conductivity. It is suggested that such high resistance at the grain boundaries is resulted from potential barriers which may be formed at the grain boundaries [11-12]. For example, the GB

conductivity of BZY material is lower than the bulk value, meaning that the grain boundaries in the BZY serve as extra resistance in series to further hinder the proton migration. Guo et al. reported that ionic particles could transport across the grain boundary in rare earth-doped zirconia and ceria. A positively charged grain boundary core exists at the grain boundary [13-17].

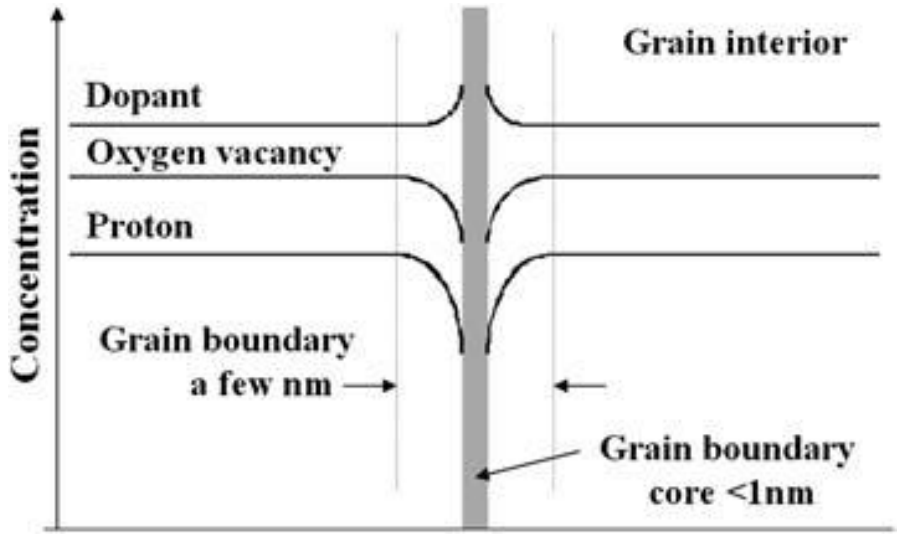

Fig. 5.1 Schematic illustration of the space charge layer at the grain boundary [12]

A schematic illustration of space charge layers around the grain boundary is shown in Fig. 5.1. The ionic conductivity is in proportion to the oxygen vacancy concentration. On the other hand, the depletion layers of oxygen vacancies at the grain boundary cause higher resistance and lower ionic conductivity. A depletion layer of positively charged oxygen vacancies and an accumulation layer of negatively charged dopants are formed at both sides of the grain boundary core, because of compensation for the positive

charge. The positively charged grain boundary core could be regarded as a product from the discontinuity of grains in various oxides in grain boundary of BZY system [12]. Therefore, the grain boundary has negative effect to ionic conductivity.

The complex impedance is typically represented in a Nyquist plot, where the imaginary impedance (Z'') component is plotted as a function of the real impedance component (Z'). Typical schematic of an equivalent circuit and Nyquist plot is shown in Fig. 5.2.

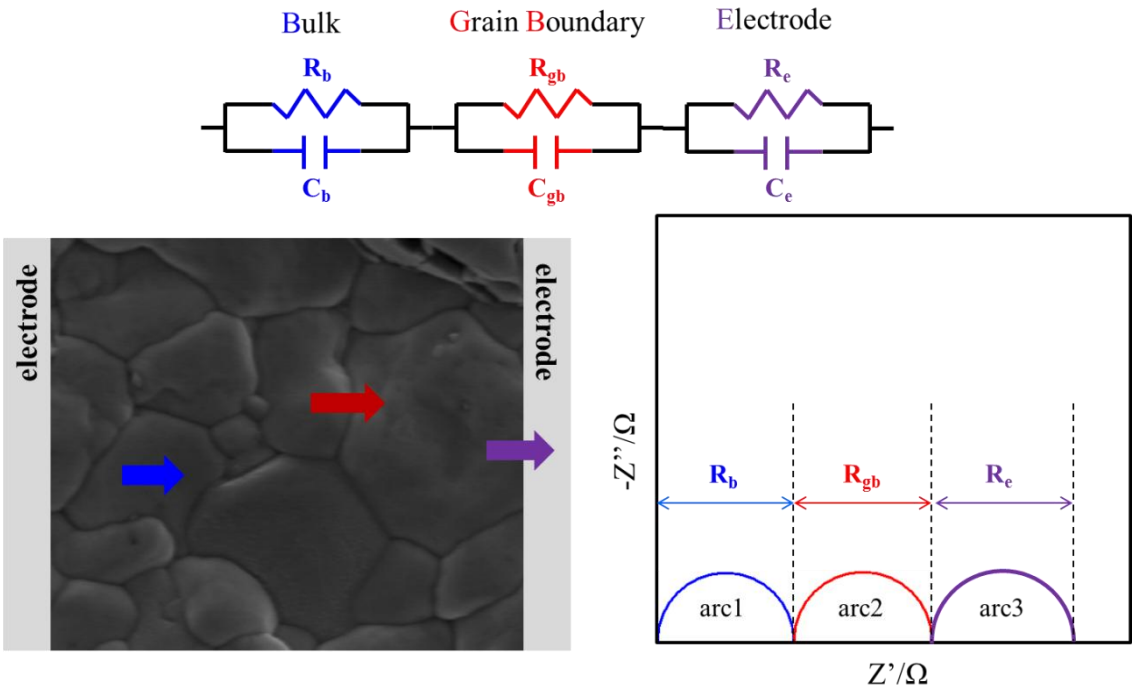

Fig. 5.2 Schematics of an equivalent circuit and Nyquist plot

In 2-probe impedance measurements, each species of resistance appears as an arc and can be modeled with an appropriate equivalent circuit. In perovskites materials, the

three processes are typically represented bulk (arc 1), grain boundary (arc 2), and electrode (arc 3) responses with decreasing frequency.

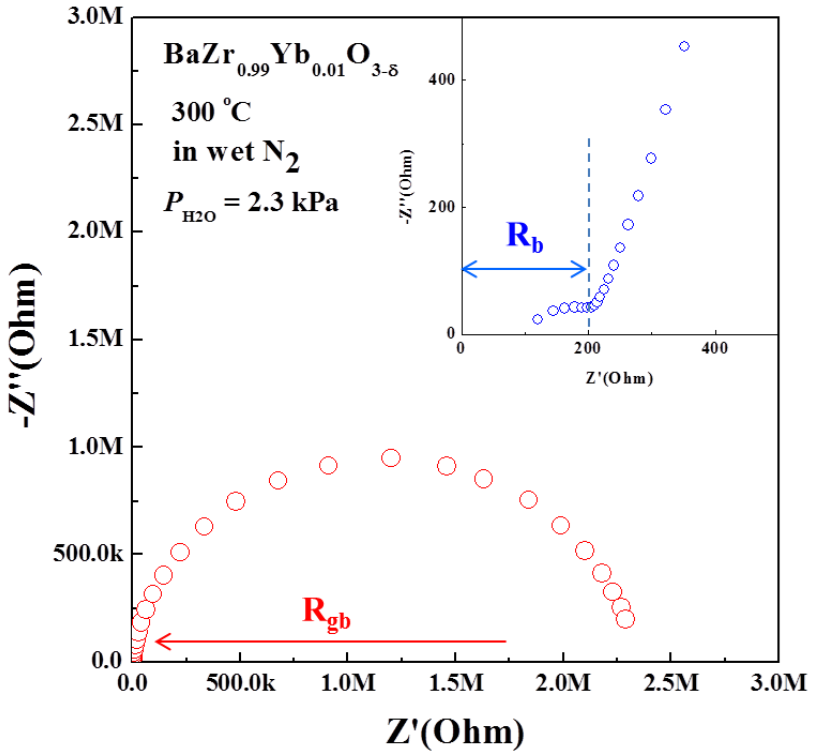

Fig. 5.3 Nyquist plots of $BaZr_{0.99}Yb_{0.01}O3_{3-\delta}$ measured at 300 °C under a given water partial pressure. The insets show the plots in high-frequency regions (bulk)

As mentioned above, a small amount of trivalent cation doped barium zirconate oxide has high grain boundary resistance. Fig. 5.3 shows the Nyquist plots of $BaZr_{0.99}Yb_{0.01}O3_{3-\delta}$ (BZYb1) measuring at 300 °C under moist N_2 atmosphere. Bulk resistance of BZYb1 electrolyte is smaller than grain boundary resistance of BZYb1 electrolyte. Several reports also show the similar phenomenon in BZY system

[14,18,19]. The grain boundary blocking could increase in several ways such as using a high doping level and grain growth. Iguchi et al. reported that a significant decrease in the grain boundary resistance of BZY proton conductors with increasing of the Y doping level [20].

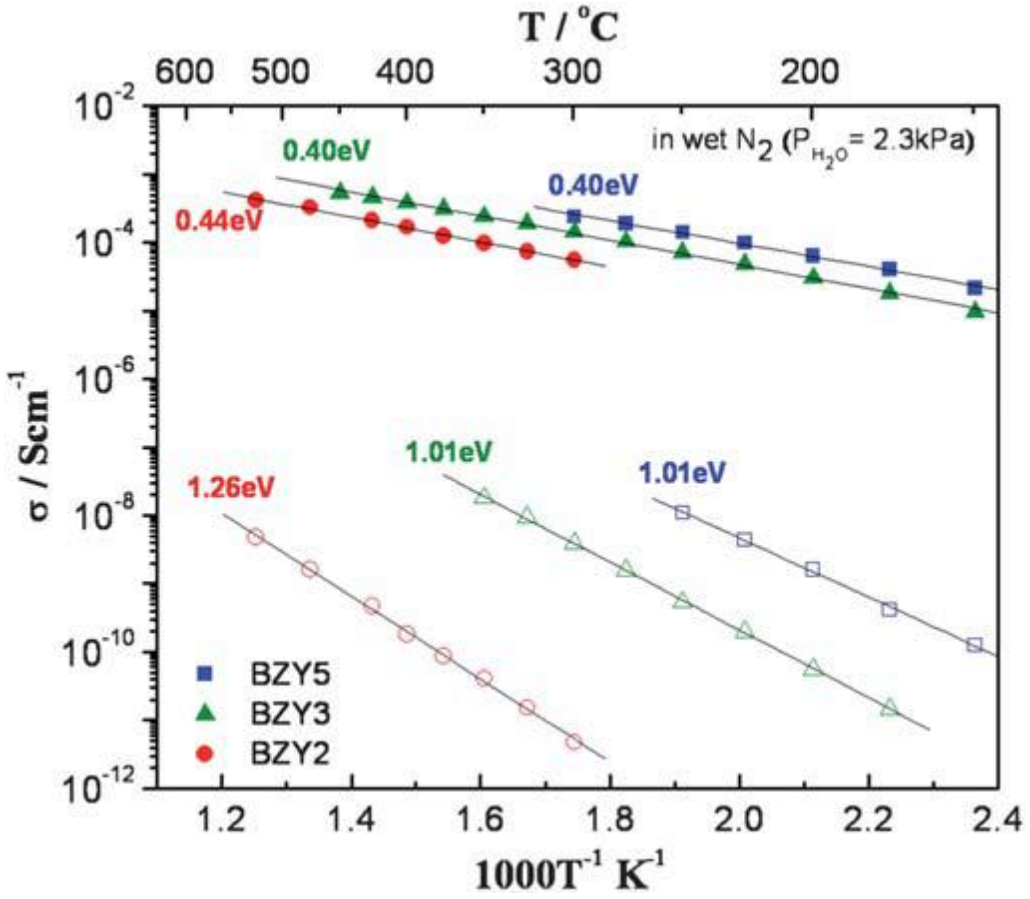

Fig. 5.4 The Arrhenius plots of the bulk (solid symbol) and the grain boundary (open symbol) conductivities of $BaZr_{1-x}Y_xO_{3-\delta}$ in moist N_2 atmosphere [20]

Fig. 5.4 shows the bulk and grain boundary conductivity of BZY in wet N_2 atmosphere. The addition of yttrium assists the grain growth of barium zirconate, and this effect

become stronger with the increase of the doping level [7]. According to these results, the addition of yttrium significantly could accelerate the grain growth of BZY system, and this effect became more remarkable with increasing of the doping level. Namely, it is suggested that the grain boundary conductivity shows strong dependence on the BZY system. Indium is another possible dopant for barium zirconate and is reported to enhance the sinterability, whereas the conductivity is less than that of Y-doped case, due to low bulk conductivity of In-doped $BaZrO_3$ [21-23].

In this study, the effect of yttrium and indium doping to barium zirconate, i.e., $BaZr_{1-x}Y_xO_{3-\delta}$, $BaZr_{1-x}In_xO_{3-\delta}$, ($x$ = 0.1, 0.2), on the electrical conductivity is compared. It was found that the yttrium doping results in higher conductivity than indium doping, while the indium doping leads to lower activation energy of the grain boundary conduction. In response to this result, yttrium-indium co-doping, i.e. $BaZr_{1-x-y}In_xY_yO_{3-\delta}$ (x, y = 0.1, 0.2) has been investigated to see how the conductivity and activation energy changes. These investigated compounds are referred to hereafter as BZY, BZI and BZIY, or composition-specifically as BZY91, BZY82, BZI91, BZI82, BZIY811, BZIY721 and BZIY712, respectively.

5.2 Experimental

5.2.1 Preparation of $BaZr_{1-x-y}In_xY_yO_{3-\delta}$ electrolytes by chemical solution method

$BaZr_{1-x-y}In_xY_yO_{3-\delta}$ (x = 0, 0.1, 0.2 and y = 0, 0.1, 0.2) electrolytes were prepared by a chemical solution method using aqueous solution. $Ba(NO_3)_2$ (Wako, 99 %),

$ZrO(NO_3)_2 \cdot xH_2O$ (Zirconyl nitrate solution, Aldrich, 35 wt %, 99 %), $Y(NO_3)_3 \cdot 6H_2O$ (Wako, 99.9 %) and $In(NO_3)_3 \cdot 3H_2O$ (Wako, 98 %) were used. Citric acid (Wako, 99.5 %) and ethylene diamine tetraacetic acid (EDTA, Dojindo, 99 %) were used as chelating and complexing agents. The molar ratio between total metal cations, EDTA, and citric acid was set at 1:1.5:1.5 and the appropriate amounts of the materials are dissolved in deionized water under vigorous stirring. NH_3 water (Chameleon reagent, 28 %) was added to the solution to adjust the pH to approximately 9 to 10. The aqueous solution was dehydrated on a hot plate at 260 ^oC to generate a viscous liquid.

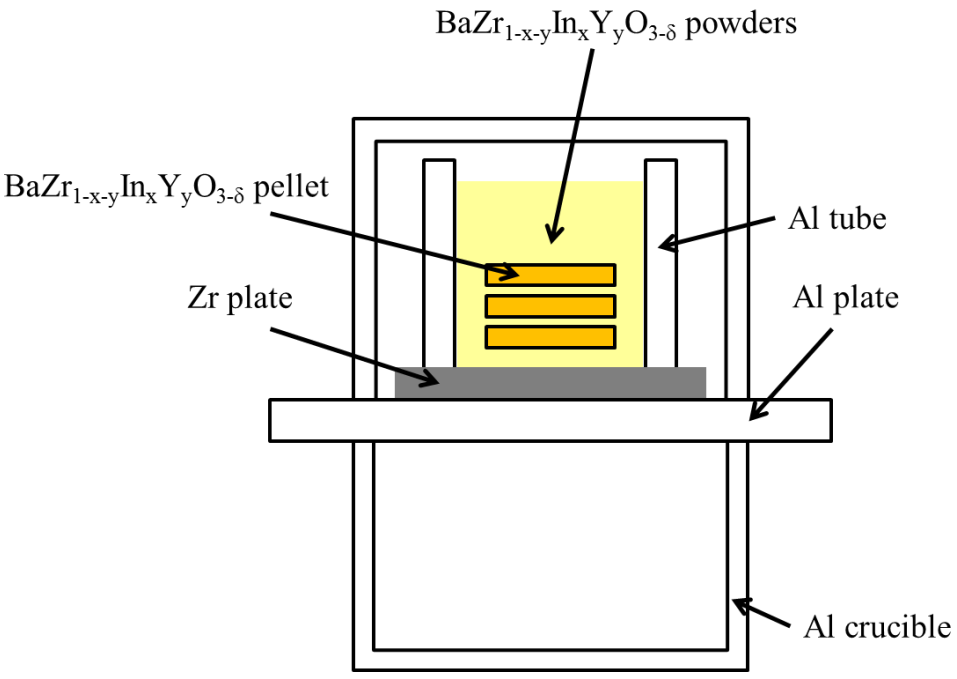

Fig. 5.5 Schematic diagram of the sintering process

This material was then dried at 240 ^oC for overnight in vacuum and calcined at 900 ^oC for 10h to obtain precursor powder. The powder was then ball milled in ethanol at 300

rpm for 5 days with 2 mm zirconia balls and dried at 120 ^{o}C for overnight in vacuum, sieved (150 μm), pressed into pellets at 250 MPa for 10 min and finally sintered at 1600 ^{o}C for 10 h in air. The synthesis powders were then ball milled in ethanol at 300 rpm for 5 days with 2 mm zirconia balls and dried at 120 ^{o}C for overnight in vacuum oven and sieved (150 μm), pressed into pellets at 250 MPa for 10 min and finally sintered at 1600 °C for 10 h in air atmosphere. The pellets were covered in a powder of same composition powders as the pellet during sintering process to protect pellets from BaO loss during the long exposure to high temperature (above 1600 ^{o}C) (Fig. 5.5).

5.2.2. Characterization

The crystal structures of the sintered samples were investigated by X-ray diffraction (XRD, Cu Kα, 40 kV–40 mA, Rigaku). The microstructures of the sintered pellets were observed via a scanning electron microscopy (SEM, Topcon, SM-350) conducted on the fracture surface. The electrical conductivity of $BaZr_{1-x-y}In_xY_yO_{3-\delta}$ electrolytes were measured by a 4-probe AC impedance method (Versa state 3) (Fig. 5.6). The sintered and polished $BaZr_{1-x-y}In_xY_yO_{3-\delta}$ samples were painted with platinum electrode (Tanaka kikinzoku, TR-7907) on the bar sample surface, then heat-treatment at 950 ^{o}C for 1 h in air atmosphere. The electrical conductivity was measured between 300 to 700 ^{o}C in moist 1% H_2 atmosphere (P_{H2O} = 1.9 kPa), where recorded over a frequency range of 1 MHz to 0.1 Hz with an amplitude of 10 mV. The electrical conductivity was calculated using the following equation; $\sigma = l/RA$ where l, R and A are the length of electrolyte, total resistance and cross sectional area, respectively.

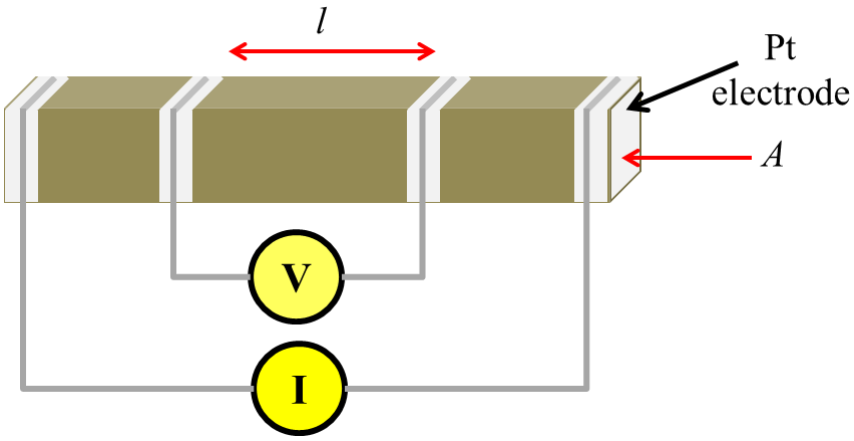

Fig. 5.6 Schematic illustration of 4-probe impedance cell

5.3 Result and discussion

5.3.1 Characteristic of Y- and In-doped barium zirconate proton conducting materials

The XRD patterns of BZY and BZI electrolytes as sintered at 1600 ^{o}C for 10 h in air are shown in Fig. 5.7. The patterns of all the specimen show the cubic structure without secondary phase. The lattice parameter and relative density are indicated in table 5.1. With respect to BZY and BZI systems, the lattice parameters are in the order of BZY82 > BZY91 > BZI82 > BZI91. The ionic radius of the six-coordinated In^{3+}, Y^{3+} and Zr^{4+} are 80 pm, 90 pm and 72 pm, respectively [24], and the order of the lattice parameters are consistent with the ionic radii. The relative density obtained for all the synthesized specimens were above 90 % and is dependent on the doping level. 10 % Y- and In-doped barium zirconate showed relative densities lower than 92 %.

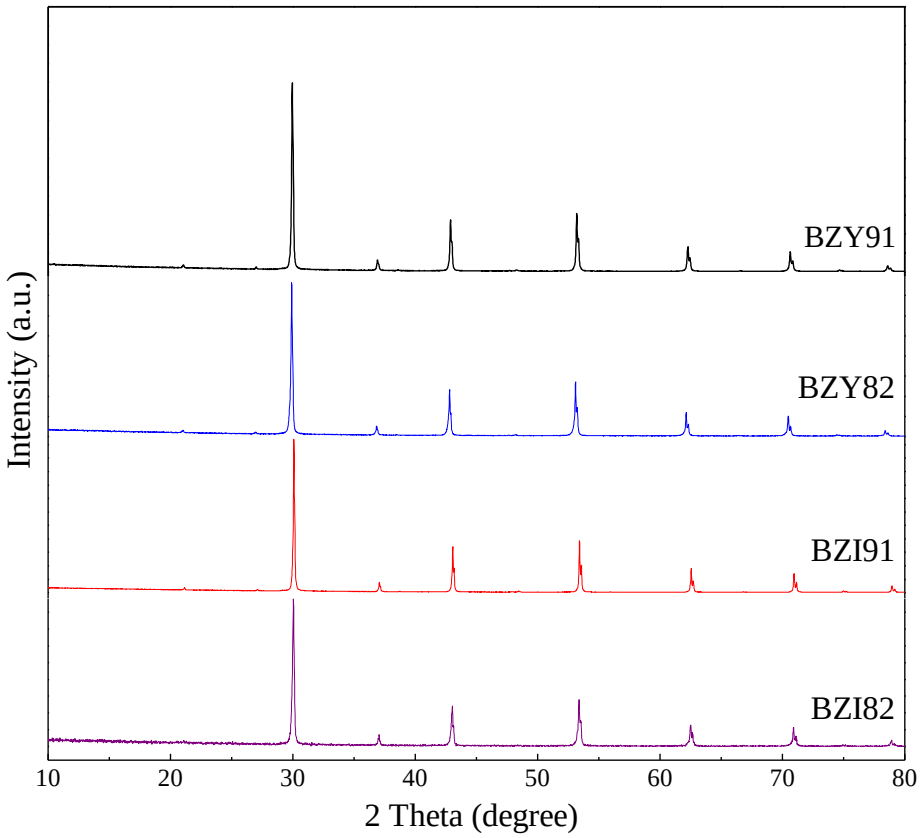

Fig. 5.7 XRD patterns of BZY and BZI electrolytes as sintered at 1600 ^{o}C for 10 h in air

Table 5.1 The lattice parameter and relative density of BZY and BZI as sintered pellets

sample	Lattice parameter, a (nm)	Relative density (%)	Activation Energy (E_a), 300–400 ^{o}C (eV)
BZY91	0.4214	91.8	0.82
BZY82	0.4222	97.1	0.75
BZI91	0.4197	91.5	0.52
BZI82	0.4200	96.9	0.46

As mentioned above, low sinterability is a characteristic feature of barium zirconate based electrolytes. As doping level increases, the relative density increased 91.8 % to 97.1 % in BZY system. The same tendency is found in the BZI system as increased 91.5 % to 96.9 %.

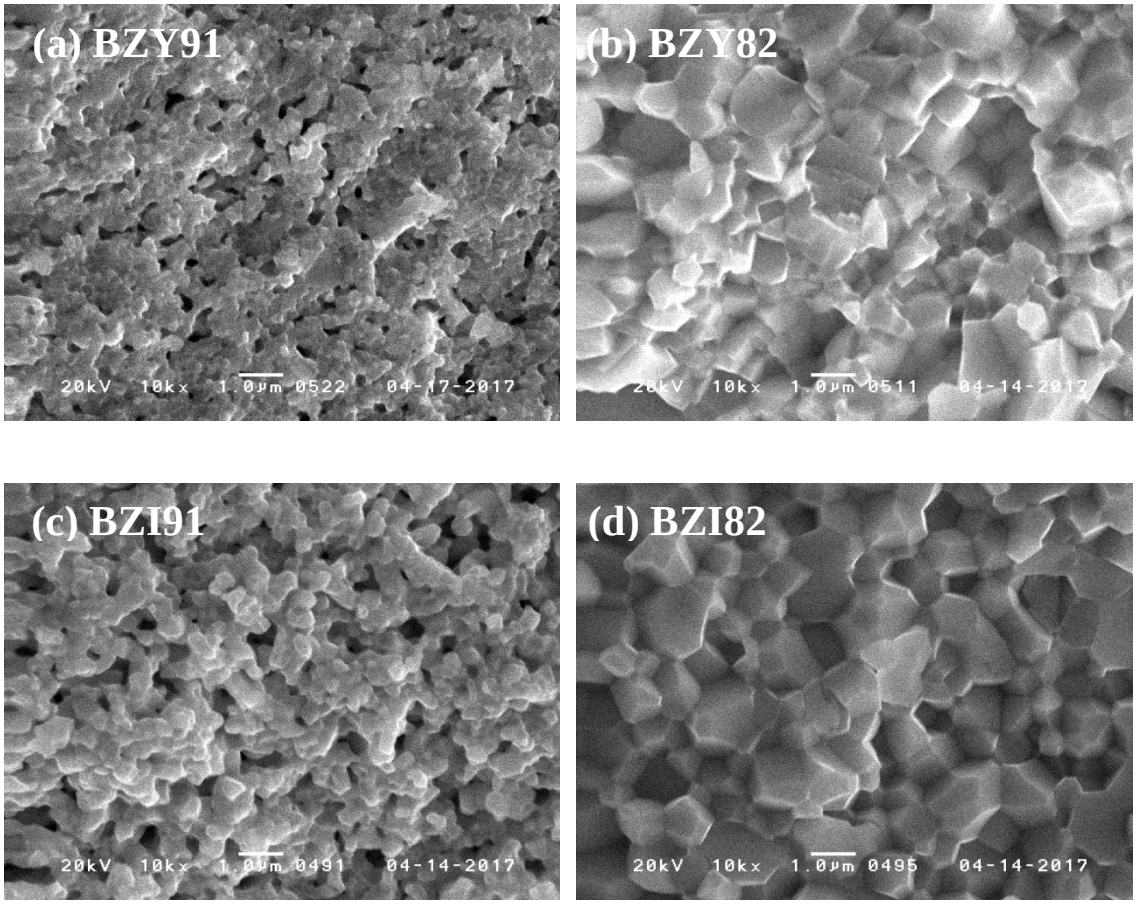

Fig. 5.8 SEM images of fractured cross-sections of (a) BZY91, (b) BZY82, (c) BZI91 and (d) BZI82 as sintered disk

SEM images of the fractured cross-sections of BZY and BZI samples are

shown in Fig. 5.8. BZY91 and BZI91 have small grains with porosity. Dense microstructure with uniform grain size was obtained with BZY82 and BZI82 samples. The increase in the doping level of either Y or In cause well developed grains with uniform grain size and high density. This tendency is consistent with those reported on BZY [7]. Doping of yttrium and indium showed similar effect on the enhancement of sintering and the enhancement is more pronounced in the case of In doping as recognized in Fig. 5,8, although the difference is not significant.

The Arrhenius plots of the electrical conductivity of BZY and BZI in moist 1% H_2 atmosphere are shown in Fig. 5.9. The plots are not straight but bending particularly in the case of BZY82. This bending feature is due to the change in the process dominating the electrical conductivity [25-26]: temperature dependence of the grain boundary resistance is larger than that of the bulk resistance. Since the two resistances are in series, the larger component dominates the total resistivity, and as a result the grain boundary dominates the total resistivity (conductivity) at low temperature with a higher slope in the Arrhenius plots. As temperature increases, the contribution of the bulk resistivity increases, and hence the slope of the plots would decrease. These temperature dependent changes between the bulk and grain boundary contributions would result in the bending of the Arrhenius plots [25-26]. The activation energy calculated from the slope of the plots in the temperature range of 300-400 ^{o}C which would thus be grain boundary dominant region is listed in Table 5.1. It is notable that the activation energy of BZI, which is around 0.46-0.52 eV, is markedly smaller than that of BZY, 0.75-0.82 eV. Thus it can be concluded that the activation energy of grain boundary conductivity is smaller than that of BZY. It is generally supposed that the

origin of the grain boundary resistance is the electric potential barrier developed by the electric double layer (space charge layer) [11-12]. The present result suggests that the formation of such space charge is more significant in the case of BZY than in the case of BZI.

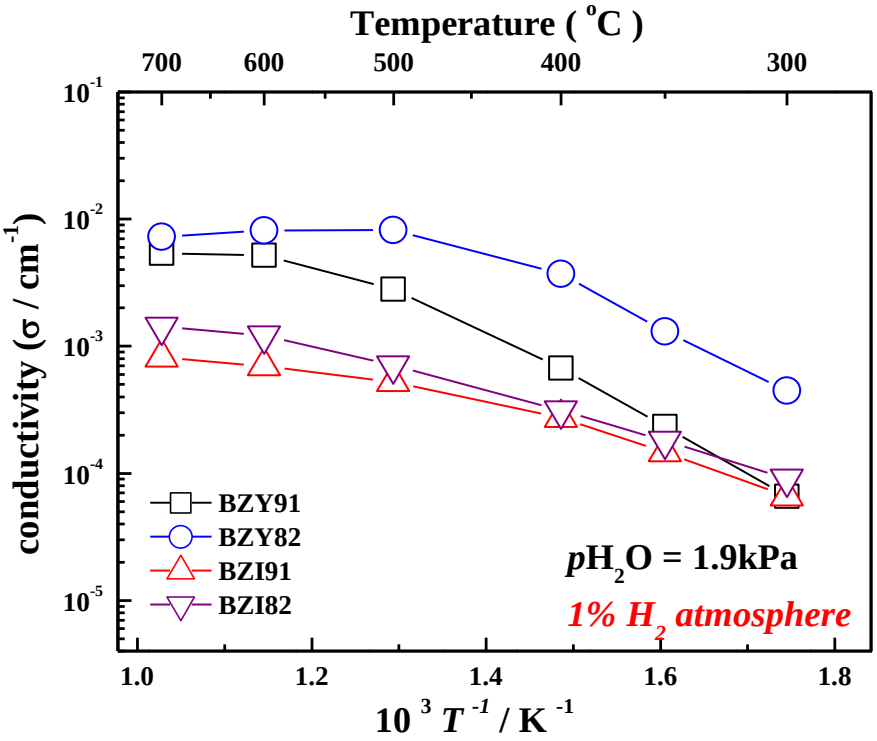

Fig. 5.9 The temperature dependence of the electrical conductivity of BZIY in moist 1% H_2 atmosphere

On the other hand, at the higher temperature region where the bulk conductivity would become dominant, the conductivity of BZY is higher than that of BZI. This suggests that Y doping is advantageous in increasing the bulk conductivity compared to

In doping in consistent with the idea shown by Kreuer that Y is the best dopant for barium zirconate [2,26].

In the above discussion, grain boundary and bulk dominant temperature regions have been discussed only from the slope of the Arrhenius plots. Contribution of these may usually be more clearly discussed by impedance analysis. However, separation between the bulk and grain boundary contributions to the conductivity is difficult for barium zirconte and the methods are under investigation.

5.3.2 Characteristic of Y and In co-doped barium zirconate proton conducting materials

As discussed above, BZY has high bulk conductivity and BZI is characterized by low activation energy of grain boundary conductivity. Thus co-doping of Y and In, i.e. BZIY, will bring us interests on how these properties change on the co-existence of the two dopant species. Figure 5.10 shows the XRD patterns of BZIY811, BZIY712 and BZIY721 pellets after sintered at 1600 ^{o}C for 10 h. The XRD results show the cubic structure without secondary phase. The lattice parameter and relative density are listed in table 5.2. With respect to the BZIY system, the lattice parameter size are in the order of BZIY712 > BZIY721 > BZIY811. Figure 5.11 shows SEM observation of the fractured cross section of the specimens. Good grain growth was observed in BZIY712 and BZIY721. It appears that the high doping concentration promotes grain growth of BZIY.

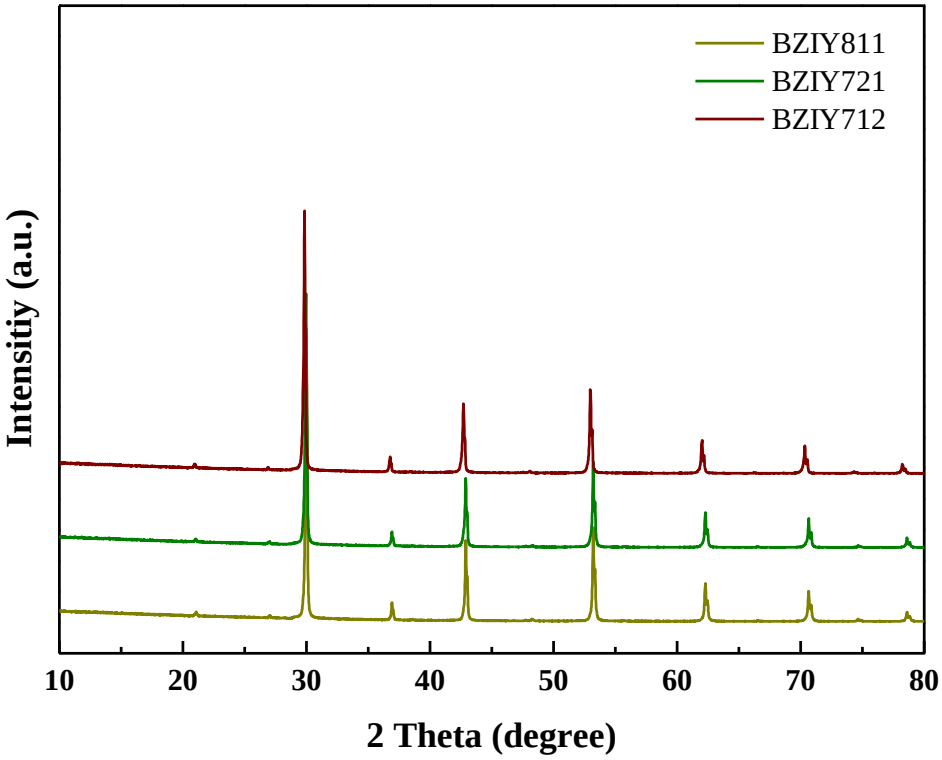

Fig. 5.10 XRD patterns of BZIY712 and BZIY721 electrolytes as sintered at 1600 ^{o}C for 10 h in air

Table 5.2 The lattice parameter and relative density of BZIY as sintered pellets

sample	Lattice parameter, a (nm)	Relative density (%)	Activation Energy (E_a), 300–400 ^{o}C (eV)
BZIY811	0.4213	94.2	0.58
BZIY721	0.4215	95.8	0.66
BZIY712	0.4229	96.3	0.74

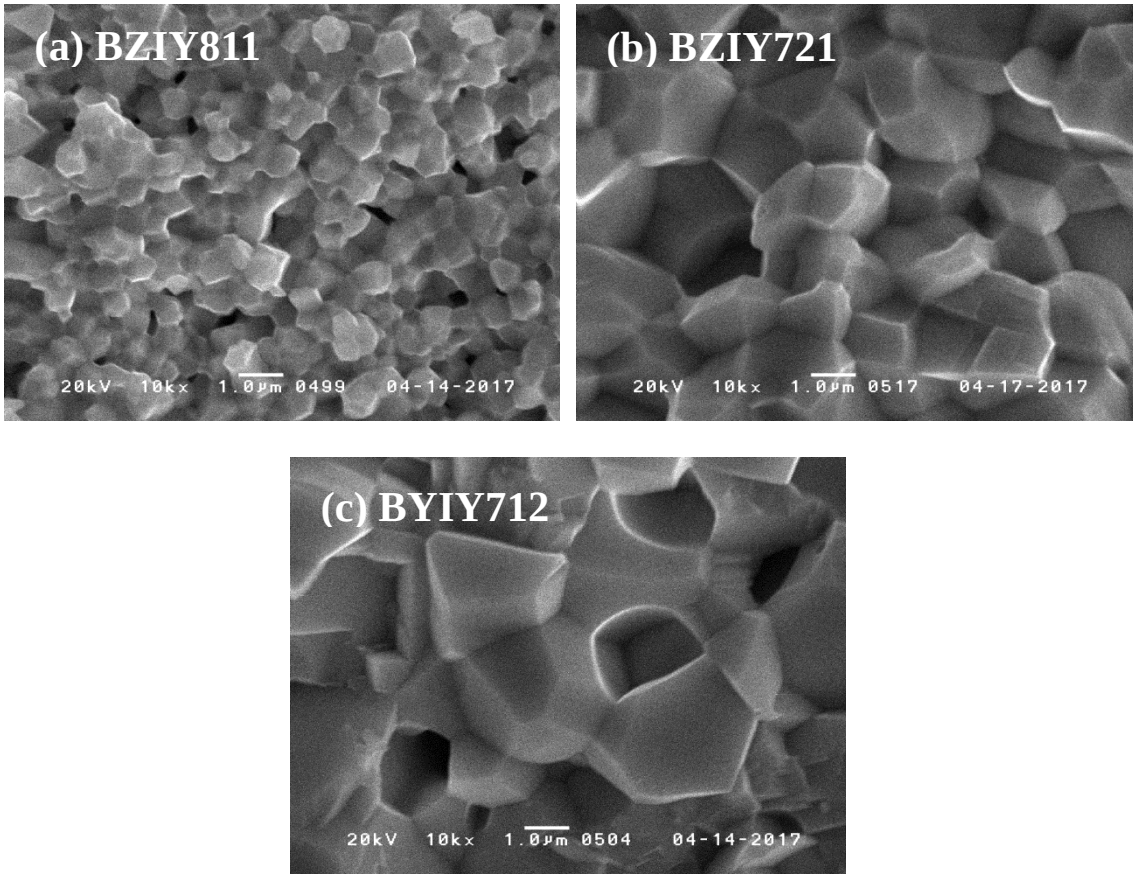

Fig. 5.11 SEM images of fractured cross-sections of (a) BZIY811, (b) BZIY721 and (c) BZIY712 as sintered disk

The Arrhenius plots of the electrical conductivity of BZIY in moist 1% H_2 are shown in Fig. 5.12. As mentioned above, the bending feature of the electrical conductivity is due to the change in bulk (above 500 ^{o}C) and grain boundary (below 400 ^{o}C) dominating of the electrical conductivities, and here how these conductivities are affected by the co-substitution is discussed. BZIY811 is the sample in which the half of In in BZI82 is substituted by Y. In response to this substitution, the electrical conductivity in the region dominated by bulk conductivity became higher than that of

BZI82: the conductivity is higher than the logarithmic average of the conductivities of BZI82 and BZY82 in the bulk-dominant temperature region (above 500 ^{o}C). On the other hand, the activation energy of the grain boundary conductivity of BZIY811, 0.58 eV, is smaller than the average of the activation energies of BZI82 and BZY82. It is apparent that the co-substitution of Y and In synergistically works, i.e. it results in enhancing the bulk conductivity and lowering the activation energy of grain boundary conductivity from these averages.

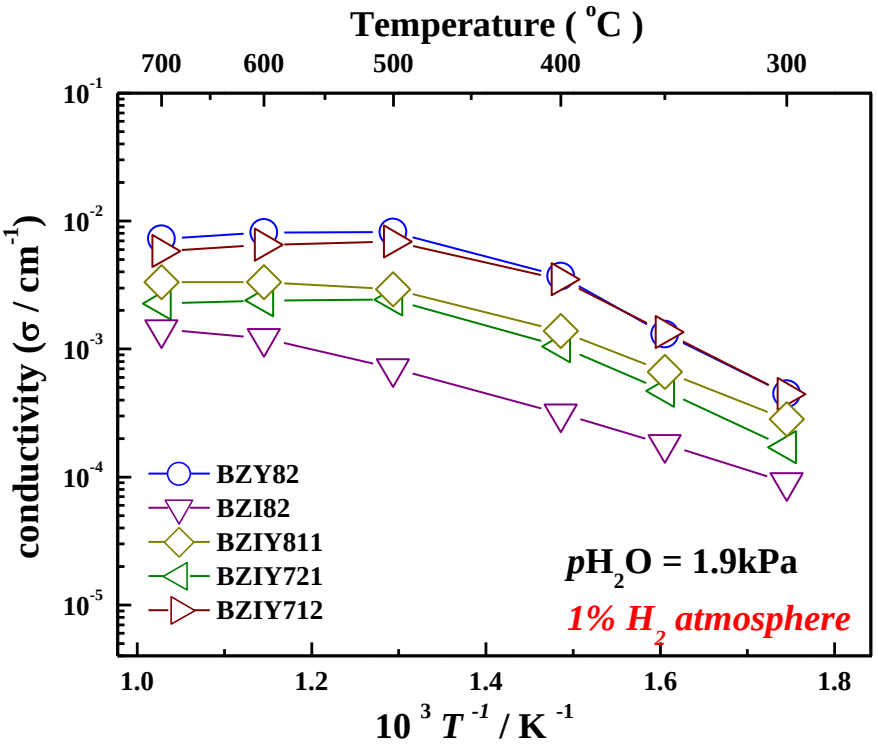

Fig. 5.12 The temperature dependence of the electrical conductivity of BZIY in moist 1% H_2 atmosphere

Then either Y or In doping is increased by another 10 % from BZIY811, resulting in the compositions of BZIY712 and BZIY721, respectively. In BZIY712, increasing amount of dopant leads to the increase in the bulk conductivities, however, the activation energy in grain boundary conduction also increased. In comparison with the conductivity of BZY82, the conductivity of BZIY712 is almost the same. A small decrease at high temperature suggests that In doping cause a small degradation of the conductivity of BZY82. On the other hand, BZY721 showed inferior properties in both the bulk conductivity and activation energy of the grain boundary conductivity to those of BZY811. As a result, BZIY721 electrolyte show slightly decreased conductivities than that of BZIY811 in all examined temperature region. From these results, the co-doping may result in degradation of the absolute values of conductivity when the original conductivity is already high. However, the present results suggest that the co-doping of yttrium and indium can work for specific purposes of controlling bulk and/or grain boundary conductivities by choosing each doping level appropriately.

5.4 Conclusion

The electrical properties of trivalent-cation-doped $BaZr_{1-x-y}In_xY_yO_{3-\delta}$ (x=0, 0.1, 0.2 and y=0, 0.1, 0.2) have been investigated. Comparison between the properties of BZY and BZI suggests that BZY is characterized by higher bulk conductivity, but BZI has lower activation energy of the grain boundary. Co-doping of Y and In promotes the enhancement of the bulk conductivity and lowering of activation energy of the grain boundary conductivity in the inferior materials. Although, no example could be found in

increasing the conductivity which is already high, such co-doping possibly control the specific bulk-grain-boundary conductivity feature of the materials.

5.5 Reference

[1] H. Iwahara, T. Yajima, T. Hibino, K. Ozaki, H. Suzuki, *Solid State Ionics*, 61 (1993) 65–69

[2] K. D. Kreuer, *Annu. Rev. Mater. Res.*, 33 (2003) 333–359

[3] K. H. Ryu, S. M. Haile, *Solid State Ionics*, 125 (1999) 355–367

[4] R. C. T. Slade, S. D. Flint, N. Singh, *Solid State Ionics*, 82 (1995) 135–141

[5] K. Bae, D. Y. Jang, H. J. Jung, J. W. Kim, J. W. Son, J. H. Shim, *J. Pow. Sour.*, 248 (2014) 1163–1169

[6] W. Sun, Z. Zhu, Z. Shi, W. Liu, *J. Pow. Sour.*. 229 (2013) 95–101

[7] Y. Yamazaki, R. Hernandez-Sanchez, S. Haile, *Chem. Mater.*, 21 (2009) 2755–2762

[8] H. G. Bohn, T. Schober, *J. Am. Ceram. Soc.*, 83 (2000) 768–772

[9] F. Iguchi, T. Yamada, N. Sata, T. Tsurui, H. Yugami, *Solid State Ionics*, 177 (2006) 2381–2384

[10] J. Tong, D. Clark, L. Bernau, M. Sanders, R. O'Hayre, *J. Mater. Chem.*, 20 (2010) 6333–6341

[11] S. Kim, J. Maier, *J. Electrochem. Soc.*, 149 (2002) J73–J83

[12] F. Iguchi, N. Sata, H. Yugami, *J. Mat. Chem.*, 20 (2010) 6265–6270

[13] X. Guo, *Solid State Ionics*, 81 (1995) 235–242

[14] X. Guo, J. Maier, *J. Electrochem. Soc.*, 148 (2001) E121–E126

[15] X. Guo, *J. Am. Ceram. Soc.*, 86 (2003) 1867–1873

[16] X. Guo and R. Waser, *Solid State Ionics*, 173 (2004) 63–67

[17] S. K. Tiku, F. A Kroger, *J. Am. Ceram. Soc.*, 63 (1980) 183–189

[18] C. T. Chen, C. E. Danel, S. Kim, *J. Mat. Chem.*, 21 (2011) 5435–5442

[19] S. Kim, J. Fleig, J. Maier, Phys. Chem. Chem. Phys., 5 (2003) 2268–2273

[20] F. Iguchi, C. T. Chen, H. Yugami, S. Kim, *J. Mat. Chem.*, 21 (2011) 16517–16523

[21] S. Imashuku, T. Uda, Y. Nose, G. Taniguchi, Y. Ito, Y. Awakura, *J. Electrochem. Soc.*, 156 (2009) B1–B8

[22] L. Bi, E. Fabbri, Z. Sun, E. Traversa, *Solid State Ionics*, 196 (2011) 59–64

[23] K. D. Kreuer, St. Adams, W. Munch, A. Fuchs, U. Klock, J. Maier, *Solid State Ionics*, 145 (2001) 295–306

[24] R.D. Shannon, *Acta Cryst.*, A32 (1976) 751–767

[25] F. Iguchi, N. Sata, T. Tsurui, H. Yugami, *Solid State Ionics*, 178 (2007) 691–695

[26] Z. Sun, E. Fabbri, L. Bi, E. Traversa, Phys. *Chem. Chem. Phys.*, 13 (2011) 7692–7700

Chapter 6

Conclusion

6.1 General summary

In chapter 2, the electrical properties of transition metal-doped (Ba / Sr)(Ce/Zr)$_{0.85}$Y$_{0.1}$*M*$_{0.05}$O$_{3-\delta}$ (*M*= Co, Fe, Mn, Ni) proton-conducting perovskites have been investigated. The electrical conductivity of SrCe$_{0.85}$Y$_{0.1}$*M*$_{0.05}$O$_{3-\delta}$ slightly increased than or almost same to that of SrCe$_{0.9}$Y$_{0.1}$O$_{3-\delta}$, and BaCe$_{0.85}$Y$_{0.1}$*M*$_{0.05}$O$_{3-\delta}$, BaZr$_{0.85}$Y$_{0.1}$*M*$_{0.05}$O$_{3-\delta}$, and SrZr$_{0.85}$Y$_{0.1}$*M*$_{0.05}$O$_{3-\delta}$ were mostly decreased. From the EMF results, it was found that BaCe$_{0.85}$Y$_{0.1}$Ni$_{0.05}$O$_{3-\delta}$, SrCe$_{0.85}$Y$_{0.1}$Ni$_{0.05}$O$_{3-\delta}$ and SrCe$_{0.85}$Y$_{0.1}$Mn$_{0.05}$O$_{3-\delta}$ samples confirmed a decrease in proton transport and an increase in the number of oxygen/electronic transport number. Thus, it can be concluded that the proton concentration was decreases than that of original electrolyte, but the total conductivity suppresses the large change due to the increases of oxygen or electron transport number. Also, the changes of the electrical conductivity depend on the choice of A and B–site as well as on the various atmospheres. Information on transition metal doped electrolytes can assist in selecting suitable oxide electrode materials.

In chapter 3, continuing from the chapter 2, the electrode activities of BaCe$_{0.85}$Y$_{0.1}$*M*$_{0.05}$O$_{3-\delta}$ (*M*= Co, Fe and Mn) and BaCe$_{0.9}$Y$_{0.1}$O$_{3-\delta}$ electrolytes were evaluated by testing protonic ceramic fuel cell performance. The current interrupt measured on BaCe$_{0.85}$Y$_{0.1}$*M*$_{0.05}$O$_{3-\delta}$ could elucidate that transition metal doping leaded to

increasing overpotential of anodic and cathodic. Also, the order of the increased in electrodes overpotentials of $BaCe_{0.85}Y_{0.1}M_{0.05}O_{3-\delta}$ is consistent with the order of decreasing electrical conductivity due to the introducing of transition metal. Analysis results obtained by impedance measurements and the current interruption can be concluded that the increased resistance of the electrolyte due to the transition metal contributes to the electrodes overpotentials in the fuel cell to increase.

In chapter 4, for clarifying the mixed effect of a cation on proton conduction, the electrical conductivity and the proton concentration of $SrZr_{0.9-x}Ce_xY_{0.1}O_{3-\delta}$ (x= 0.0, 0.2, 0.4, 0.6 and 0.9) were investigated. The electrical conductivity and proton concentration reached a maximum value at x= 0.4. The hydration energy and immobile oxygen vacancies increased with Zr content increasing, but $SrZr_{0.5}Ce_{0.4}Y_{0.1}O_{3-\delta}$ shows only oxide ion vacancy involved in hydration. Yttrium doped cerate and zirconate with the formula $A(Zr_{5/9}Ce_{4/9})_{1-x}Y_xO_{3-\delta}$, ($A$ = Sr, Ba; x = 0.1, 0.2) have been studied as proton conducting electrolytes. $BaZr_{0.44}Ce_{0.36}Y_{0.2}O_{3-\delta}$ has higher proton mobility than $BaZr_{0.5}Ce_{0.4}Y_{0.1}O_{3-\delta}$, $SrZr_{0.44}Ce_{0.36}Y_{0.2}O_{3-\delta}$ and $SrZr_{0.5}Ce_{0.4}Y_{0.1}O_{3-\delta}$ in response to an increase in Y-dopant and retained the highest proton conductivity in moist 1% H_2 at 600 °C as well as excellent chemical stability under 80 % steam for 200 hours. The major difference in conductivity among the studied compositions is originated from the difference in proton concentration and the magnitude of the grain boundary contribution. In regard to the suitable balance between conductivity and stability achieved by $BaZr_{0.44}Ce_{0.36}Y_{0.2}O_{3-\delta}$, this composition seems to be the optimized choice of electrolyte for SOEC at intermediate temperature.

In chapter 5, the influences of In- and Y-doping on the electrical conduction

properties of barium zirconate were investigated. The electrical conductivity were measured on of $BaZr_{1-x-y}In_xY_yO_{3-\delta}$ (x=0, 0.1, 0.2 and y=0, 0.1, 0.2), elucidating that yttrium doping causes high bulk conductivity and indium doping leaded to lower activation energy of the grain boundary. Co-doping of yttrium and indium promotes the enhancement effect of improving the bulk conductivity and lowering of activation energy, and it is thus expected that the co-doping with yttrium and indium can work for controlling the bulk and grain boundary conduction specifically in the materials.

This thesis furnished information of electrical properties of transition metal doped electrolytes can assist in selecting suitable oxide electrode materials. Additionally, newly designed proton conducting material is expected to establish application for fuel cell or electrolysis cell. It is hoped that this research will be useful for the importance of hydrogen system and for the development of electrolytes for fuel cells and electrolysis cells.

6.2 Outlook for future plan

In this study, the electrical properties of the electrolyte due to the introduction of transition metal and the fuel cell performance test were examined. However, the fundamental reason for the change of properties due to the transition metal is still unclear. The change in the valent state of the transition metal depending on the *A*- or *B*-site cation and the atmosphere can be an important answer. I will try to clarify the reasons for the change of properties of the transition metal on the electrolyte through the change of the valent state.

Acknowledgments

This thesis is the result of work during which I have been supported and entertained by many people. I would like to express my thanks to all those who made the completion of my doctoral thesis possible. I am greatly indebted to my supervisor Professor Hiroshige Matsumoto for giving me the opportunity to pursue my graduate research under his guidance. Every discussion, insight and perspectives I acquired were invaluable. He has been really inspiration for taking a creative and innovative approach to the research of proton conducting materials.

I am very thankful to my dissertation committee members Prof. Hisahiro Einaga, Prof. Miki Inada and Prof. Fujio Tsumori for their important guidance to this thesis and critical comments.

I am also very grateful for the practical help and general support obtained from my group members Dr. Kwati Leonard, Dr. Yuki Terayama, Dr. Yi-Hsuan Lee and PhD-student Yasuhiro Takamura. Additionally, I would like to thank Prof. Yuji Okuyama at the University of Miyazaki for his time and useful discussions. I enjoyed all the conversations with Matsumoto group members and graduated students. It was a great pleasure to work and socialize with them.

Finally, I would like to thank my family for all the love they showed me and for standing behind me and giving me the encouragement and motivation to complete this part of my challenge in life.